In Situ Tensile Investigations on AA 7020-T6 Using Synchrotron Diffraction for Texture, Lattice Strain and Defect Density Studies

Doctoral Thesis
(Dissertation)
to be awarded the degree
Doctor of Engineering (Dr.-Ing.)

submitted by
Zhengye Zhong
from Chengdu city, Sichuan province, China

approved by the Faculty of Natural and Materials Science
Clausthal University of Technology

Date of oral examination
16.07.2015

Chairperson of the Board of Examiners: Prof. Dr.-Ing. habil. Joachim Deubener

Chief Reviewer: apl. Prof. Dr. rer. nat. Dr.-Ing. habil. Heinz-Günter Brokmeier

Reviewer: Prof. Dr.-Ing. habil. Lothar Wagner

Name, Vorname Datum:

EIDESSTATTLICHE ERKLÄRUNG

Hiermit erkläre ich an Eides Statt, dass ich die bei der Fakultät für Natur- und Materialwissenschaften der Technischen Universität Clausthal eingereichte Dissertation selbständig und ohne unerlaubte Hilfe verfasst und die benutzten Hilfsmittel vollständig angegeben habe.

Unterschrift

Name, Vorname Datum:

EIDESSTATTLICHE ERKLÄRUNG

Hiermit erkläre ich an Eides Statt, dass die eingereichte Dissertation weder in Teilen noch in Ihrer Gesamtheit einer anderen Hochschule zur Begutachtung vorliegt oder vorgelegen hat und dass ich bisher noch keinen Promotionsversuch unternommen habe.

Unterschrift

Abstract

The present work deals with the texture, dislocation and lattice strain evolution under uniaxial tension. The in situ experiments were carried out using high-energy X-ray diffraction and a 20 kN universal tensile machine. The anisotropic mechanical behavior is revealed through the reflex-dependent lattice strain evolution of flat samples under uniaxial tension.

The as-received material is a 29.5 mm thick aluminum block with strong texture gradient along the block thickness. In the first experiment, two tensile samples from 7.5 mm below the surface were prepared along the RD (rolling direction). The two samples have the deformation texture (copper type) with sharpness of 10 mrd (multiples of random distribution). One sample is used to study the texture evolution and the other sample is used to determine the lattice strain evolution and dislocation evolution during uniaxial tension. During the tensile test, the texture changes slightly due to the low amount of deformation from initial state to sample fracture. In contrast, significant changes in reflex-dependent lattice strains are observed. In the elastic region, the {111} lattice planes are the stiffest, as in theory, but the {200} lattice planes are not the most compliant ones due to the interaction with neighboring grains having other orientations. Moreover, the Young's modulus of {311} lattice planes is less affected by the texture of 10 mrd. The work hardening during plastic deformation shows a clear dependence on the grain orientations, as shown by the reflex-dependent lattice strains. The essential difference of work hardening as a function of grain orientation is based on two types of dislocation arrangements, the so called [111] tension stress state and [100] tension stress states. Load release first starts on the {111} and {222} lattice planes before macroscopic UTS (ultimate tensile strength). After UTS all lattice planes experience load release. The dislocation density evolution indicates that in the elastic region, dislocation density decreases as the tensile stress increases. From YS (yield strength), the increase of dislocation density causes the work hardening. Near UTS region, the dislocation density becomes constant. Further beyond UTS, some grain orientations show further work hardening while other grain orientations show softening. It leads to a slight increase in the dislocation density. In the fracture region, a significant increase of dislocation density is observed. It results from the reversal stress (compressive stress) which is formed outside the necking zone, caused by the return of elastic strain.

In a second experiment the anisotropic behavior of AA 7020-T6 sample with maximum orientation density of 29.7 mrd was investigated. For this purpose, three flat samples from the center of the Al-block were prepared, with the orientations of 0° to RD, 45° to RD and 90° to RD. The uniaxial tensile tests were carried out till UTS, which shows three stress-strain curves with different yield strengths, ultimate tensile strengths and elongations. The in situ experiments were performed in HEMS@PetraIII/DESY. Due to the low elastic anisotropy of aluminum, the yield strengths, which were determined from the reflex-dependent lattice strain evolution, show only small variation. The plastic anisotropy is much stronger, which can be observed from the lattice strain evolution of all the three samples. The tensile test of the 45° to RD sample shows lowest values of YS and UTS. The variation of lattice strain shows that differently oriented grains undergo different stresses. This effect is greatest in the 45° to RD sample. Overall, the 45° to RD sample shows the most specific characteristics, because less (111) and more (200) grain orientations are available.

Zusammenfassung

Die vorliegende Arbeit befasst sich mit der Entwicklung der Textur, den Versetzungsdichten und den reflexabhängigen Dehnungen während eines uniaxialen Zugversuches. Das in situ Experiment würde mittels hochenergetischer Röntgendiffraktion und einer 20kN Zuganlage durchgeführt. Mit Hilfe der reflexabhängigen Dehnungen wurden Aussagen über die Anisotropieeigenschaften der Blechprobe gemacht.

Bei dem Ausgangsmaterial handelte es ich um einen Aluminiumblock von 29,5mm Dicke mit starkem Texturgradienten über die Blockdicke. In einem ersten Experiment wurden zwei Zugproben aus einer Tiefe von 2,5mm unterhalb der Oberfläche präpariert. Die Deformationstextur dieser Probe (Kupfertyp) hat eine Texturschärfe von 10mrd. Eine Probe wurde zur Studie der Texturentwicklung verwendet und an der zweiten Probe wurden Gitterspannungen und Versetzungen bei uniaxialer Zugspannung bestimmt. Während des Zugversuchs ändert sich die Textur ändert sich nur wenig. Der Grund ist die geringe Verformung der Probe bis zum Bruch. Dagegen sind deutliche Änderungen der reflex-abhängigen Gitterspannungen zu beobachten. Die härteste Ebene ist die {111}, wie von der Theorie vorhersagt, aber {200} ist nicht die weichste Orientierung, was durch den Einfluss benachbarter Körner erklärt werden kann. Es wurde festgestellt, dass der E-Modul der Körner mit {311} Orientierung nur wenig von der Textur beeinflusst wird. Die Kaltverfestigung während der plastischen Verformung zeigt eine deutliche Abhängigkeit von der Korn-orientierung, wie der Verlauf der reflexabhängigen Gitterdehnungen zeigt. Der wesentliche Unterschied der Kaltverfestigung als Funktion der Kornorientierung beruht auf zwei Typen der Versetzungsanordnung, dem sogenannten [111] Dehnungsstress-Zustand und dem [100] Dehnungsstress-Zustand. Der Abfall der angelegten Zugspannung im Spannungsdehnungs-diagramm wurde zuerst bei {111} und{222} schon vor Erreichen der Zugfestigkeit beob-achtet. Nach Erreichen der Zugfestigkeit ist der Abfall der angelegten Spannung bei fast allen Reflexen zu beobachten. Die Defektdichteentwicklung als Funktion der Zugspannung zeigt, dass im elastischen Bereich die Defektdichte abnimmt. Ab der Streckgrenze bewirkt die Kaltverfestigung eine kontinuierliche Zunahme der Defektdichte. Diese Entwicklung geht in einen Teil mit konstanter Defektdichte um die Zugfestigkeit über. Weitere Belastung über Zugfestigkeit zeigt Kornorientierungen, die weiter Verfestigen, während andere Kornorientierungen entfestigen. Dies führt zu einem leichten Anstieg der Defektdichte. In dem Versagensbereich ist ein deutlicher Anstieg der Defektdichte zu beobachten. Es baut sich eine Gegenspannung (Druckspannung) außerhalb der Bruchzone auf, die durch die Rückführung der elastischen Dehnung verursacht wird.

In einem zweiten Experiment wurde das anisotrope Verhalten der AA 7020-T6 Probe mit einer Orientierungsdichte von 29.7mrd untersucht. Dazu wurden aus dem Zentrum des Al-Blocks Flachzugproben mit den Orientierungen 0° zur WR (Walzrichtung), 45° zur WR und 90° zur WR genutzt. Die einachsigen Zugexperimente wurden bis zum Erreichen der Zugfestigkeit (Rm) durchgeführt und zeigen unterschiedliche Streckgrenzen (Rp0.2), Zugfestigkeiten und Dehnungen der drei Spannungs-Dehnungs-Kurven. Die in situ Experimente wurden an HEMS@PetraIII/DESY durchgeführt. Wegen der geringen elastischen Anisotropie von Al zeigen die Streckgrenzen, die aus reflexabhängigen Dehnungs-entwicklung bestimmt worden sind, nur geringe Variation. Die plastische Anisotropie ist deutlich stärker, was an der Entwicklung der einzelnen Gitterdehnungen für alle drei Proben zu sehen ist. Das Zugexperiment der Probe 45° zur WR liefert die geringsten Rp0.2, Rm Werte. Die Variation der Gitterdehnung zeigt, dass unterschiedlich orientierte Körner unterschiedliche Verformungsspannungen aufnehmen. Dieser Effekt ist bei der Probe 45° zur WR am größten. Insgesamt zeigt diese Probenorientierung die meisten Besonderheiten auf, da sehr wenig (111) und sehr viel (200) Kornorientierungen vorhanden sind.

Acknowledgements

This thesis has been submitted in partial fulfillment of the requirements for a doctoral degree in the Faculty of Natural and Materials Science of Clausthal University of Technology in Germany. This research was carried out between October 2010 and March 2015 supported by China Scholarship Council through the File No. 2010605125.

It is my great honor to express my gratitude to Prof. Dr. Heinz-Günter Brokmeier for giving me the chance to carry out my doctoral research under his supervision. Thanks for his patience, guidance, inspirations and kindness during the whole study.

I would like to thank Prof. Dr. Lothar Wagner for reviewing my thesis and giving comments on my thesis.

I would like to thank Bernd Schwebke working in Helmholtz-Zentrum Geesthacht for his friendship, his help when we made measurements together and telling me many good things of Germany, from which I know more German culture.

I appreciate the numerous discussions with Dr. Emad Maawad and his help. Thanks for his patience in correcting my paper and dissertation.

I acknowledge the Helmholtz-Zentrum Geesthacht GEMS outstation at DESY for the provided beamtime, during which I conducted most of my experiments. Thanks Dr. Norbert Schell for his help during the measurements. I acknowledge the Forschungsneutronenquelle Heinz Maier-Leibnitz in Garching FRM II for providing beamtime at beamline Stress-SPEC. I am grateful for the assistance of Dr. Weimin Gan during the measurements and the help from Dr. M. Hofmann. I am also thankful that Mr. B. Eltzschig from Helmholtz-Zentrum Geesthacht processed all my tensile samples.

I would like to thank Dr. U. Vainio, Dr. P. Staron, Dr. D. Lott, Dr. L. Lottermoser, Dr. M. Z. Salih, Dr. N. Al-hamdany, PhD candidate Daniel Ostach, PhD candidate Malte Blankenburg, Mr. H. Burmester, Mr. J. Schumann and Mr. P. König for their help. Thank all the friends who helped me with the living in Germany.

I would also like to thank Prof. Guangmin Sheng working in Chongqing University, China, for his guidance during my study for Master degree.

I express my deep gratitude to my mother and father for their support, their worries and everything. I would like to thank my grandparents and the whole family for the support. I also want to say thanks to my future wife who has not yet appeared in my life for letting me concentrate on my study.

Table of Contents

1. INTRODUCTION AND AIMS .... - 1 -

1.1 INTRODUCTION .... - 1 -
1.2 AIMS AND OBJECTIVES .... - 3 -

2. LITERATURE SURVEY .... - 4 -

2.1 INTRODUCTION TO ALUMINUM AND ITS ALLOYS .... - 4 -
2.2 CRYSTALLOGRAPHY OF ALUMINUM .... - 5 -
2.3 BASIC DISLOCATION THEORY .... - 7 -
2.3.1 Dislocation types and slip .... - 7 -
2.3.2 Partial dislocations and stacking faults .... - 9 -
2.3.3 Cross slip in fcc metals .... - 10 -
2.3.4 Vacancies and dislocation climb .... - 11 -
2.4 DEFORMATION MECHANISM OF FCC SINGLE CRYSTALS .... - 12 -
2.4.1 Schmid law .... - 12 -
2.4.2 Tensile deformation of fcc crystals. .... - 13 -
2.4.3 Lattice rotation during tension .... - 15 -
2.5 ORIENTATION DEPENDENCE OF YOUNG'S MODULUS IN FCC CRYSTALS .... - 17 -
2.6 DEFORMATION MODELS OF POLYCRYSTALLINE MATERIALS .... - 19 -
2.6.1 Sachs model .... - 19 -
2.6.2 Taylor model .... - 19 -
2.6.3 Bishop and Hill model .... - 21 -
2.7 GENERAL DESCRIPTION ON TEXTURE .... - 22 -
2.8 DEFORMATION TEXTURES OF FCC METALS .... - 27 -
2.8.1 Fiber texture .... - 27 -
2.8.2 Rolling texture .... - 30 -
2.9 TEXTURE MEASUREMENT USING HIGH ENERGY X-RAY .... - 37 -
2.9.1 A short introduction to Synchrotron radiation .... - 37 -
2.9.2 Texture measurement using synchrotron radiation .... - 38 -
2.10 LATTICE STRAIN DETERMINATION USING HIGH ENERGY X-RAYS .... - 41 -
2.10.1 Definition of lattice strain .... - 41 -
2.10.2 Lattice strain in fcc randomly oriented polycrystals .... - 42 -
2.10.3 Diffraction pattern measurement using synchrotron radiation .... - 44 -
2.11. ESTIMATION OF DISLOCATION DENSITY USING MODIFIED WILLIAMSON-HALL PLOT .... - 46 -

3. EXPERIMENTAL PROCEDURES .... - 49 -

3.1 AS-RECEIVED MATERIAL AND CHEMICAL COMPOSITION .... - 49 -
3.2 SAMPLE PREPARATIONS .... - 49 -
3.2.1. Round tensile sample from 7.5 mm below the surface of the as-received plate .... - 49 -
3.2.2. Flat tensile sample from the center of the as-received AA 7020-T6 plate. .... - 50 -
3.2.3. Sample for texture gradient .... - 51 -
3.3 IN SITU POLE FIGURE MEASUREMENTS UNDER DIFFERENT LOADS .... - 51 -
3.4 IN SITU DIFFRACTION PATTERN MEASUREMENTS FOR THE ROUND SAMPLE .... - 52 -

3.5 POLE FIGURE MEASUREMENT FOR TEXTURE GRADIENT INVESTIGATION - 53 -
3.6 IN SITU DIFFRACTION PATTERN MEASUREMENTS FOR FLAT TENSILE SAMPLES - 57 -
3.7 METALLOGRAPHIC SAMPLE PREPARATION AND CHEMICAL ETCHING - 57 -

4. TEXTURE EVOLUTION DURING TENSION AT RT: IN SITU MEASUREMENT - 58 -

4.1 MICROSTRUCTURE OF THE ROUND TENSILE SAMPLE - 58 -
4.2 IN SITU TEXTURE MEASUREMENTS POSITIONS - 58 -
4.3 RESULTS AND DISCUSSION - 59 -
4.3.1 Pole figure analysis - 59 -
4.3.2 ODF analysis - 62 -
4.4 SUMMARY OF THE TEXTURE EVOLUTION - 66 -

5. LATTICE STRAIN EVOLUTION DURING TENSION AT RT: IN SITU MEASUREMENT - 67 -

5.1 LATTICE DEPENDENT YOUNG'S MODULUS AND POISSON'S RATIO - 69 -
5.2 LATTICE STRAIN IN THE REGION 2 - 72 -
5.3 LATTICE STRAIN EVOLUTION IN REGION 3 - 73 -
5.4 LATTICE STRAIN EVOLUTION IN REGION 4 - 74 -
5.5 LATTICE STRAIN EVOLUTION IN REGION 5 - 75 -
5.6 DISCUSSION - 76 -
5.7 SUMMERY OF THE LATTICE STRAIN EVOLUTION - 80 -

6. DISLOCATION DENSITY EVOLUTION DURING TENSION: IN SITU MEASUREMENT - 81 -

6.1 CALIBRATION OF THE MISALIGNMENT OF THE DETECTOR - 81 -
6.2 THICKNESS CORRECTION - 82 -
6.3 INSTRUMENTAL CORRECTION - 84 -
6.4 FWHM CHANGING TREND DURING TENSION - 85 -
6.5 PEAK BROADENING ANALYSIS - 86 -
6.6 DISLOCATION EVOLUTION DURING TENSILE LOADING - 88 -
6.7 DISLOCATION DENSITY AND FLOW STRESS - 90 -
6.8 SUMMERY OF DISLOCATION DENSITY EVOLUTION - 92 -

7. ANISOTROPIC MECHANICAL BEHAVIOR ALONG DIFFERENT DIRECTIONS OF AS-RECEIVED AA 7020 PLATE - 93 -

7.1 MACRO TENSILE CURVES AND MEASURED POINTS - 93 -
7.2 CALCULATIONS OF THE LATTICE STRAIN - 95 -
7.3 RESULTS AND DISCUSSION - 96 -
7.3.1 Lattice strain in elastic region - 99 -
7.3.2 Lattice strain in elastic plastic transition regime - 101 -
7.3.3 Lattice strain in the plastic region - 102 -
7.4 SUMMERY OF THE ANISOTROPIC MECHANICAL BEHAVIOR - 105 -

8. CONCLUSIONS AND RECOMMENDATIONS - 106 -

REFERENCES - 109 -

1. Introduction and Aims

1.1 Introduction

Most engineering materials respond to an external stimulus in anisotropic way due to the presence of preferred orientation, called texture, which leads to the physical properties of the material depending on directions, thereby having a profound influence on the formability of the material. Macroscopically, a well-known example in industry is the earing occurred during deep drawing of a textured sheet [1-4], which is attributed to the texture-induced different radial elongations in different directions. Figure 1.1 shows the 0°/90° earing and the 0°/90° and 45° mixed earing and the corresponding textures.

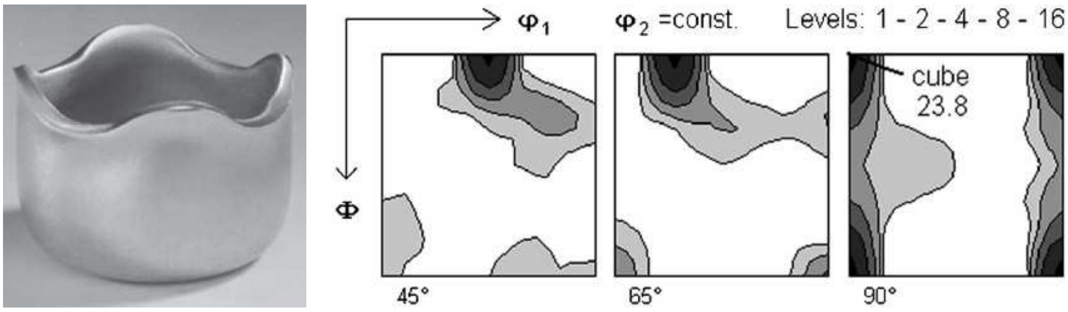

(a) 0°/90° earing and its texture

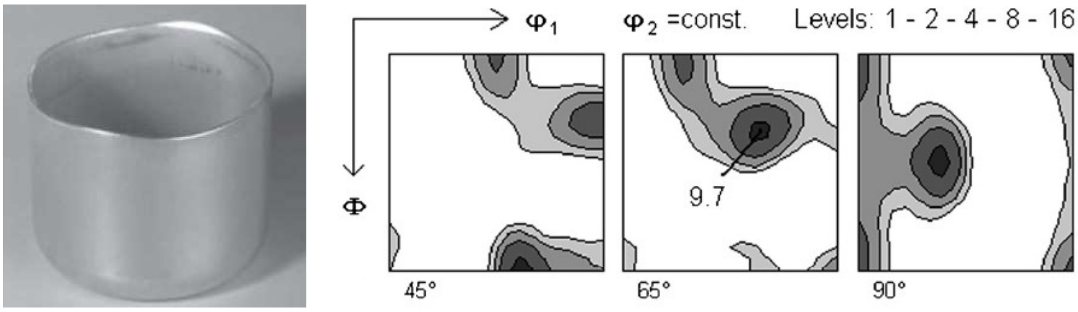

(b) 0°/90° and 45° mixed earing and its texture

Figure 1.1: Earing in deep drawing textured sheet [5-6].

Texture-induced anisotropy has been investigated by many researchers and the theoretical calculations are in good agreement with the experimental observations in many cases [7-10]. Plastic anisotropy of rolled sheet is normally characterized by r-value [11], which is defined as the ratio of plastic strain in width direction to that in through-thickness direction during tensile testing. Also plastic anisotropy can be characterized by yield locus, which is a mathematic way of expressing the stress state causing yielding [12-13]. However, it is not convenient to obtain the above-mentioned two parameters from both experiment and the theoretical calculations for textured materials [14]. Moreover, these two parameters cannot give information about what is the cause of the anisotropy in a vivid way. Other parameters which are simple and clear should be utilized to exhibit the anisotropic behavior. Lattice strain evolution offers a way to investigate the anisotropic behavior. Lattice strain can be obtained directly by diffraction methods such as neutrons and X-rays which allows to determine the lattice spacing of individual {hkl} lattice planes oriented in a specific direction[15-17]. Therefore, in the present study, orientation dependent lattice strain evolution of a highly textured AA 7020 is investigated in three orientations during uniaxial tensile loading using synchrotron X-ray diffraction, which gives insight into the reasons for the anisotropy. According to previous investigations, for a randomly oriented material, the lattice strain is dominated by single crystal anisotropy in elastic region, but for a textured one, lattice strain is determined by both single crystal anisotropy and preferred orientations [18-20]. In plastic region, many factors may contribute to the anisotropic behaviors. They include single crystal anisotropy, plastic anisotropy (slip prefers in special orientations), preferred orientations etc. Preferred orientations strongly influence the orientation correlation between a grain and its adjacent grains, thereby playing an important role in plastic anisotropy. Besides, preferred orientations also decide the amount of grains with specific {hkl} planes orientated in a special direction, resulting in the anisotropic behavior along different directions.

Furthermore, it is important to investigate how the grains rotate and how the defects in a material develop during deformation, both of which influence the lattice strain evolution. In situ investigation using synchrotron radiation coupled with the fast read-out area detector makes it possible to get a set of Debye-Scherrer rings in a short time, due to the high brilliance of the X-ray beam and the short acquisition time. Grain rotation can be determined by the pole figure measurement within several minutes while defects and lattice spacing by the diffraction pattern measurement within several seconds. Therefore, one can get the instant microstructure information at any points during deformation.

1.2 Aims and Objectives

- Study the texture evolution of a textured AA 7020-T6 (maximum orientation density 9 mrd) under uniaxial tension using in situ synchrotron X-ray diffraction.
- Study the lattice strain evolution of the crystallites oriented in specific directions such as loading direction (LD) and perpendicular to LD under uniaxial tension using in situ synchrotron X-ray diffraction. It is aimed to understand how the grains oriented in different directions with respect to LD behave during uniaxial tension. The initial maximum orientation density of the investigated sample is 10 mrd.
- Study the dislocation evolution of a textured AA 7020-T6 (maximum orientation density 10 mrd) under uniaxial tension through peak broadening analysis using *in- situ* synchrotron X-ray diffraction.
- A peak broadens as the thickness of the sample increases when the sample is investigated by X-ray diffraction in transmission geometry. Thus, it is aimed to develop a method to correct the peak broadening caused by sample thickness.
- Study the anisotropic mechanical behavior of grains oriented in different directions with respect to the rolling coordinate, i.e. 0° to RD, 45° to RD and 90° to RD through the lattice strain evolution under uniaxial tension using in situ synchrotron X-ray diffraction. The maximum orientation density of the investigated AA 7020-T6 samples is 29.7 mrd.
- Study the mechanisms which contribute to the different stress-strain behavior of the {hkl} lattice planes oriented in the different directions of highly textured AA 7020-T6 (maximum orientation density 29.7 mrd).

2. Literature survey

2.1 Introduction to Aluminum and its alloys

Aluminum, the third most abundant element in the Earth’s crust, is the most utilized non-ferrous metal in the world. Aluminum and its alloys have become increasingly important in many aspects of industry such as in the production of automobiles and aerospace equipment, construction of building etc., due to low density, high strength-to-weight ratio and high resistance to corrosion.

Large varieties of aluminum alloys are being utilized in industrial applications. According to forming procedures, aluminum and its alloys are divided into two groups: cast or wrought. For casting alloys, the products are formed by pouring the molten alloys into molds which have cavities similar to the shapes of the finished components. For the wrought alloys, the products are formed by hot and/or cold deformations, such as hot and cold rolling, drawing, forging, and extrusion. According to the alloying elements, wrought aluminum alloys are mainly divided into the following categories: unalloyed Al, Al-Cu, Al-Mn, Al-Si, Al-Mg, Al-Mg-Si, Al-Zn-Mg and Al plus other elements alloys. Therefore, there are 8 groups of Aluminum wrought alloys.

AA 7020 alloy belongs to the Al-Zn-Mg system in 7xxx series aluminum alloys, which are called high strength aluminum alloy. Zn and Mg are the principle alloying elements of this group. Mg addition in 7xxx series aluminum alloys greatly reduces the low temperature solubility of Zn in Al [21]. The alloys in this series have high age-hardening potential, especially with addition of Cu, leading to ultimate tensile strength from 220 to 610 MPa, depending on the amount of Cu. Cu addition above 0.25 % (weight percent) increases the strength of Al-Zn-Mg alloys [22], and it can improve the resistance to the stress corrosion cracking [23]. However, the addition of Cu up to 1% copper to the Al-Zn-Mg alloys does not have significant influence on the precipitation mechanism. In this case Cu remains mainly in the solid solution. Aging of AA 7020 alloy, the following phases are formed: GP (Guinier-Preston) zone (MgZn), η’ (metastable phase of $MgZn_2$), η ($MgZn_2$) and T ($Al_2Mg_3Zn_3$ or $(AlZn)_{49}Mg_{32}$). Spherical GP zones are formed after quenching and during aging from room temperature up to around 162 ℃. Firstly, the GP zones are mainly in the form of Zn clusters. Then, Mg diffuses to the clusters with the help of vacancies [24] to form GP zones with average Zn:Mg ratio of 4:1 [25]. The GP zones formed during low temperature aging have considerably low coherency strains, making deformation before aging have little or no effect on the precipitation behavior [26-27]. The strengths of the materials depend on the size and distribution of the precipitations. The maximum strength is achieved by T6 treatment (470 °C solution treatment plus 160°C artificially aged). Due to the superior strength, the alloys are widely applied in aircraft construction, military, structural parts in building construction, etc.

2.2 Crystallography of Aluminum

Aluminum possesses face-centered cubic (fcc) structure after crystallizing, the space group of which is Fm-3m (No.225). The fcc unit cell consists of an atom at each corner of the unit cell and an atom situated in the center of each face. Therefore, a unit cell contains four atoms. Figure 2.1 (a) shows the unit cell of fcc structure and (b) shows the primitive rhombohedral unit cell of fcc structure. Each atom has 12 nearest neighbors at distance of $a/\sqrt{2}$ where a is the lattice constant of Aluminum. The proportion of the space filled by the atoms in a unit cell, i.e. the packing fraction, is 0.74.

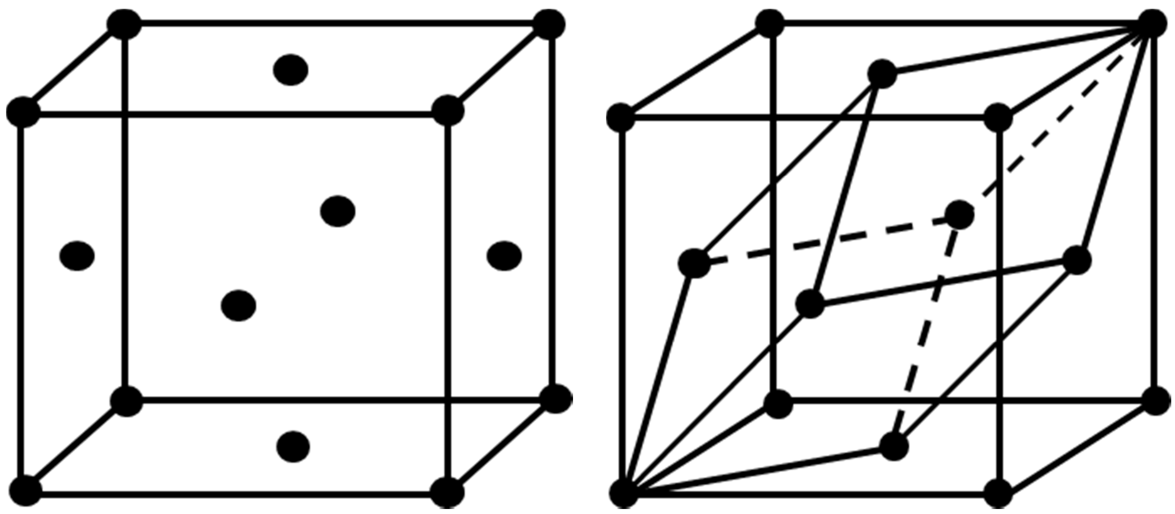
(a) (b)

Figure 2.1: (a) The unit cell of fcc crystal structure, (b) the primitive unit cell of fcc crystal structure.

Atoms are in contact along the line joining their centers in the <110> directions of the lattice, which are called close-packed directions. Viewing the fcc lattice space from any of <111> directions, each atom in the {111} planes is in contact with other six atoms with equal distance in the same plane, as shown in Fig. 2.2. The {111} planes are termed as closed-packed plane due to the closest packing arrangement of atoms. In a specific {111} planes, for example, (111) plane, the centers of atoms are located at A in Fig. 2.2. Projecting the centers of the atoms in the adjacent (111) plane onto this plane, they are located at positions marked as B in Fig. 2.2. The atoms in the adjacent (111) plane are shown in dotted cycles. Projecting the centers of atoms in a third adjacent (111) plane onto the plane marked as A, they occupy the positions marked as C. If stacking the close-packed planes successively such that they follow the sequence ABCABC…, an fcc crystal structure forms.

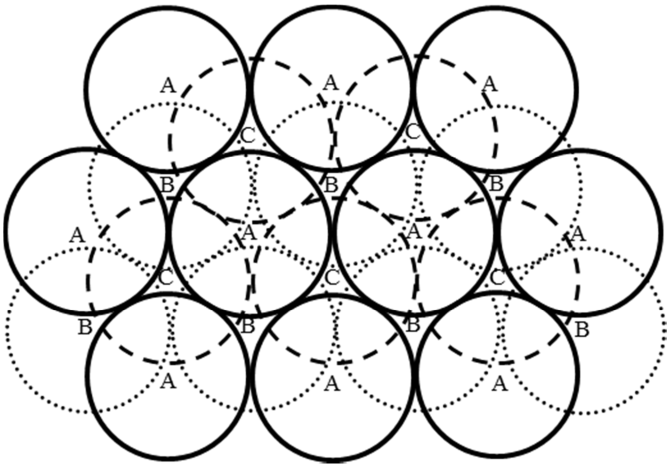

Figure 2.2: Atoms arrangements in the {111} planes.

2.3 Basic dislocation theory

2.3.1 Dislocation types and slip

Dislocations are one dimensional crystallographic defects in a crystal structure, the lines of which separate the regions on the slip plane where slip has occurred from those it has not, with atoms misaligning around the dislocation lines in a distance smaller than interatomic distance along the <110> direction in the case of fcc materials with respect to the perfect crystal structure, and atom misalignment gets smaller as the distance from the dislocation line increases. Two main types of dislocations are existed in a crystal structure, i.e. edge dislocation and screw dislocation. An edge dislocation is a linear defect with an extra half-plane of atoms inserted in a crystal, making distortion of atoms on the neighboring planes, as shown in Fig. 2.3 (a). The dislocation line of an edge dislocation is the line extending along the end of the extra half-plane. A screw dislocation forms when one part of the crystal is sheared from another part, causing spiral distortion close to the dislocation line, as shown in Fig. 2.3 (b). The dislocation line of a screw dislocation is the line along the center of the spiral of it. The Burgers vector of an edge dislocation is perpendicular to the dislocation line whereas that of a screw dislocation is parallel to the dislocation line. In real crystals, most dislocations have mixed edge and screw characters, as shown in Fig.2.3 (c). The dislocation on the left hand possesses edge dislocation character while the dislocation on the right hand possesses screw dislocation character. Between them, the dislocation has mixed characters.

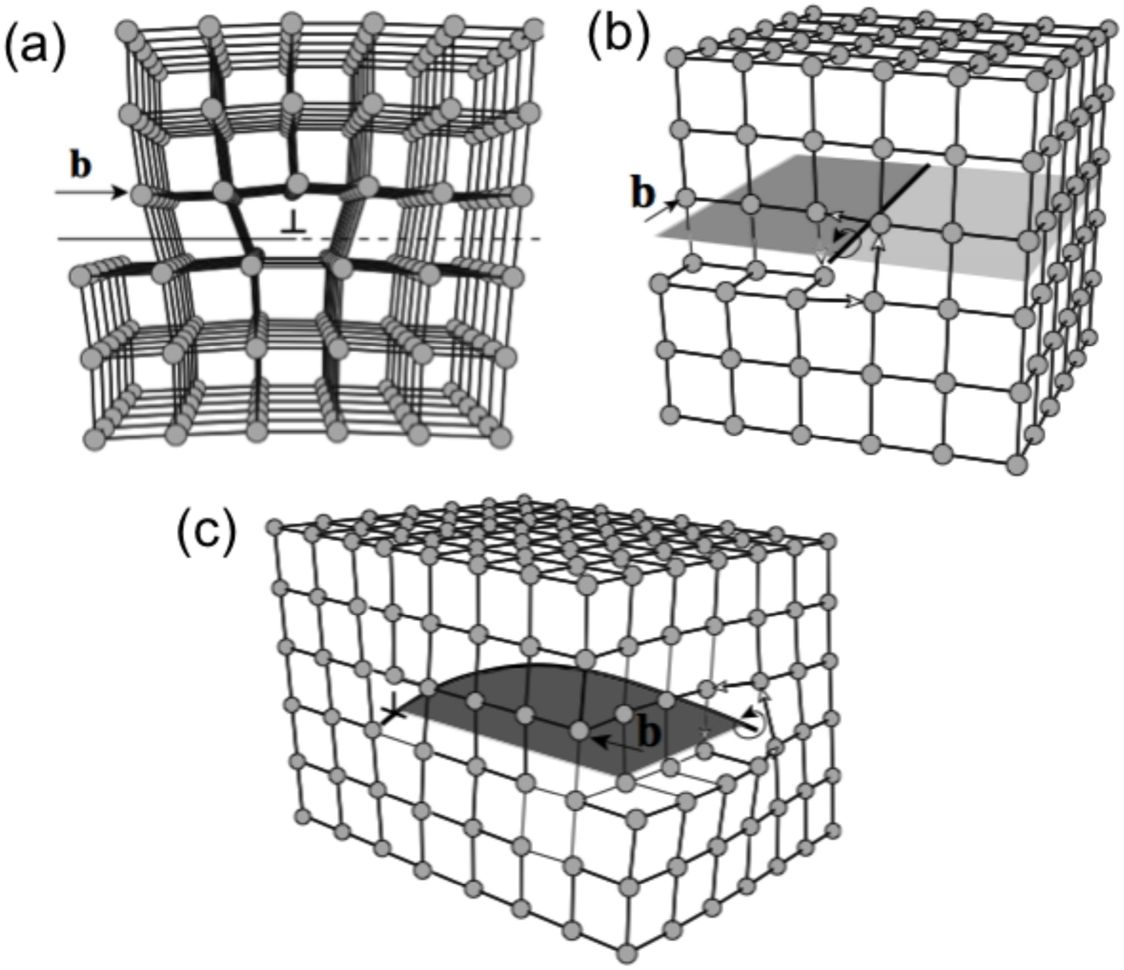

Figure 2.3: Atomic alignment around (a) edge and (b) screw dislocation and (c) a curved dislocation with mixed characters of edge and screw dislocations [28].

Dislocations start to slip when an external applied stress reaches the critical resolved shear stress (CRSS) of the material. Slip occurs on the planes containing the dislocation line and Burgers vector which are called slip plane, and in the directions where the atoms are closed packed, called slip direction. The combination of a slip plane and a slip direction forms a slip system. Table 2.1 shows the slip systems in fcc metals. Figure 2.4 shows the slip of an edge dislocation.

Table 2.1: Slip systems in fcc metals.

Plane	a = (111)			b = (-1-11)			c = (-111)			d = (1-11)		
Direction	01-1	-101	1-10	0-1-1	101	-110	01-1	101	-1-10	0-1-1	-101	110
Abbreviation	a_{I}	a_{II}	a_{III}	b_{I}	b_{II}	b_{III}	c_{I}	c_{II}	c_{III}	d_{I}	d_{II}	d_{III}

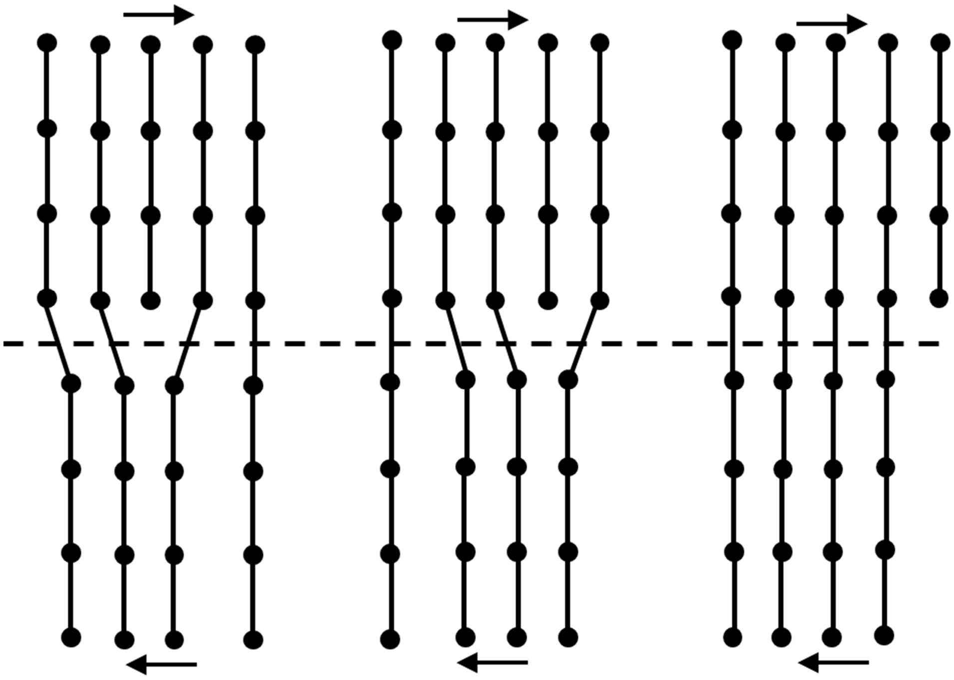

Figure 2.4: Slip of an edge dislocation.

2.3.2 Partial dislocations and stacking faults

Slip systems in fcc crystals determine that the Burgers vector in such crystal is a/2<110>, corresponding to the shortest lattice vector. A dislocation with Burgers vector a/2<110> may dissociate into two dislocations, called partial dislocations, as shown in Fig. 2.5. The displacement produced by b1 can be dissociated by two steps, b2 + b3, which decomposes the perfect dislocation into two partial dislocations, called Shockley partials [29].

$$\frac{a}{2}\left[01\bar{1}\right]\rightarrow\frac{a}{6}\left[11\bar{2}\right]+\frac{a}{6}\left[\bar{1}2\bar{1}\right] \qquad \text{(Eq. 2-1)}$$

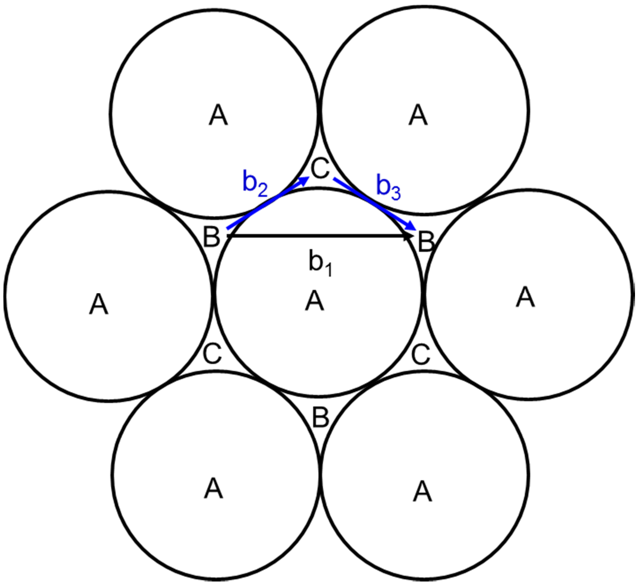

Figure 2.5: Dissociation of a dislocation into two partial dislocations [30].

When a perfect dislocation dissociates into two partial dislocations, there is a fault formed in the stacking sequence of the {111} planes, called stacking fault. It will change the stacking sequence ABCABC into ABCBC. The sequence at the fault becomes BCBC, which is a locally close-packed hexagonal structure. The region around stacking fault stands for a part of the crystal which undergoes slip between full slip and no slip. It has higher free energy than the fcc structure. The width between the two partial dislocations is determined by both the stacking fault which exerts a surface tension to pull the two dislocations together and the repulsion force between the two dislocations. The higher stacking fault energy, the smaller repulsion between the two partial dislocations and the narrower the stacking fault [31].

2.3.3 Cross slip in fcc metals

The Burgers vector of an edge dislocation is perpendicular to the dislocation line while that of a screw dislocation is parallel to the dislocation line [32]. Therefore, screw dislocations can move from one slip plane to another, especially when they meet precipitates on the original slip plane. Figure 2.6 shows the process of cross slip in an fcc crystal. A dislocation loop is moving on a (111) plane. The dislocation loop is pure edge at positions of w and y, whereas at x it is a pure right-handed screw dislocation and at z it is a pure left-handed screw dislocation.

The dislocation loop tends to move on to the intersecting (1-11) plane due to the shear stress which causes the loop to expand (see figure 2.6 (b)). The pure screw dislocation at z is free to move on to the (1-11) plane (see figure 2.6 (c)). The dislocation loop slips back to a (111) plane in Fig. 2.6 (d), which is called double cross slip. Cross slip is easier to be activated in materials with high stacking fault energy, compared to low stacking fault energy materials. And the frequency of cross slip decreases as temperature drops down. It plays an important role in dislocation generation and annihilation.

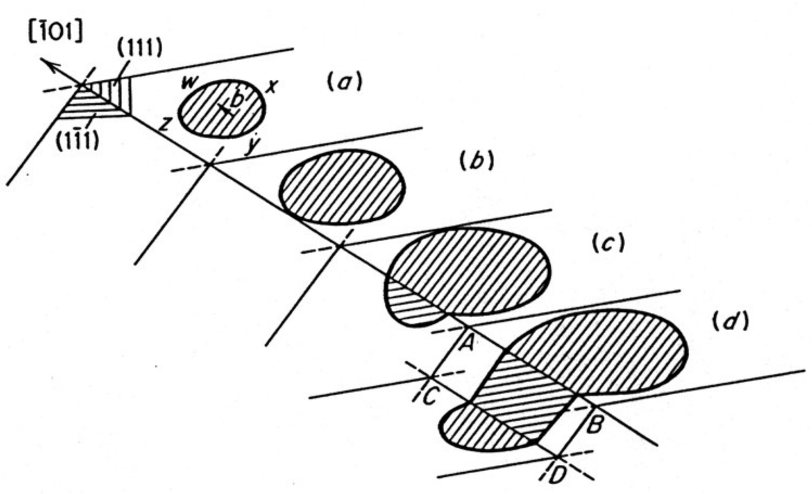

Figure 2.6: Cross slip in an fcc crystal [32].

2.3.4 Vacancies and dislocation climb

Point defects inside a material include vacancies, interstitials and substitutional atoms. A vacancy forms when an atom is missing from a normal lattice position. Vacancies can be generated by thermal excitation and increase rapidly as temperature rises. At a given temperature and at equilibrium, the fraction of vacancies is constant, depending on the energy required to move an atom from the interior to the surface. More than equilibrium number of vacancies at room temperature can be generated by rapid quenching or by extensive plastic deformation. Vacancies are related to edge dislocation climb as shown in Fig. 2.7. A vacancy moves to the dislocation core while an atom at the dislocation core moves to the vacancy position, which makes a vision that the dislocation moves up to another plane, called dislocation climb. Dislocation climb increases the probability for dislocation annihilation as dislocations moves from one slip plane to another [33].

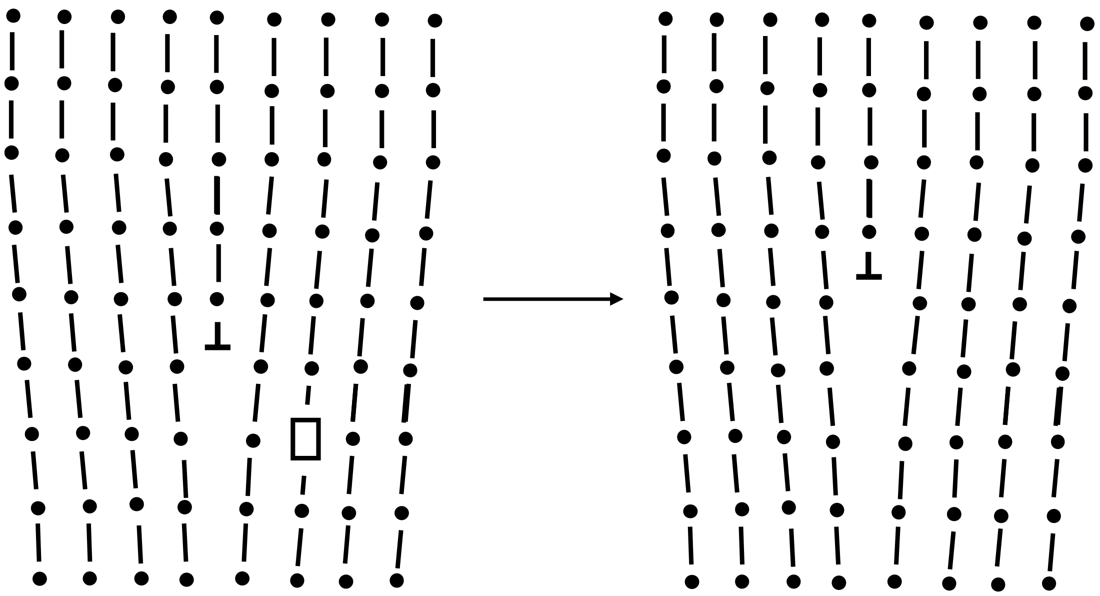

Figure 2.7: Climb of an edge dislocation.

2.4 Deformation mechanism of fcc single crystals

2.4.1 Schmid law

The deformation of most fcc crystals is primarily by slip, which occurs on specific crystallographic planes in special crystallographic directions when the shear stress on the slip system reaches a critical value τ_c, called critical resolved shear stress. The criterion for initiation of slip is called Schmid law [34]. In the case of uniaxial tension, it can be written as

$$\tau_c = \sigma \cos\lambda \cos\varphi \qquad \text{(Eq. 2-2)}$$

or $$\sigma = \tau_c / m \qquad \text{(Eq. 2-3)}$$

Where σ is the applied stress along the tensile axis; λ is the angle between the slip direction and tensile axis; φ is the angle between the slip plane normal and tensile axis; m = $\cos\lambda\cos\varphi$ which is called Schmid factor. Figure 2.8 schematically shows the relative orientations among the slip direction (**s**), slip plane normal (**n**) and tensile axis (TA).

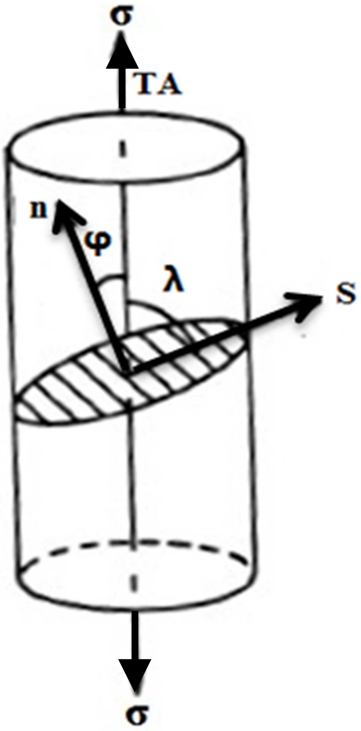

Figure 2.8: slip plane normal and slip direction in uniaxial tension.

2.4.2 Tensile deformation of fcc crystals.

Representing the tensile axis in the basic stereographic triangle with [111], [110] and [100] at the corners, as shown in Fig. 2.9, the firstly initiated slip system can be found. For all orientations of fcc crystals within this triangle, the [101](11-1) slip system, called primary slip system, has higher Schmid factor than that of any other slip system, making this slip system slide first. If the tensile axis is located in any other stereographic triangle, the primary slip system may be found in the remote corners of the three neighboring triangles. The <111> in one of the three triangles is the normal of slip plane, and the <110> in another triangle is the slip direction.

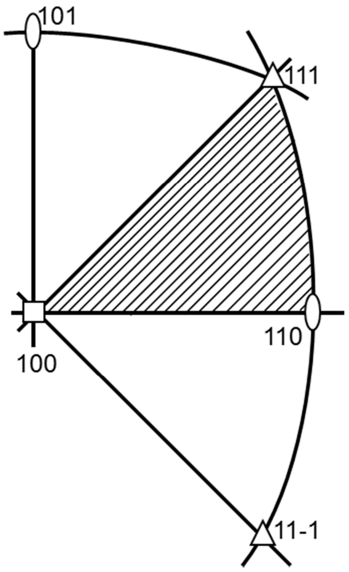

Figure 2.9: Basic orientation triangle. If the tensile axis of an fcc crystal lies in this triangle, the most heavily stressed slip system is [101](11-1) [35].

The Schmid factors for the orientations within the basic stereographic triangle are shown in Fig. 2.10. When the tensile axis is located on the great circle between the slip direction and the normal of slip plane and the angles from tensile axis to the slip direction and to the slip plane normal are both equal to 45°, the Schmid factor has its highest value, m = 0.5.

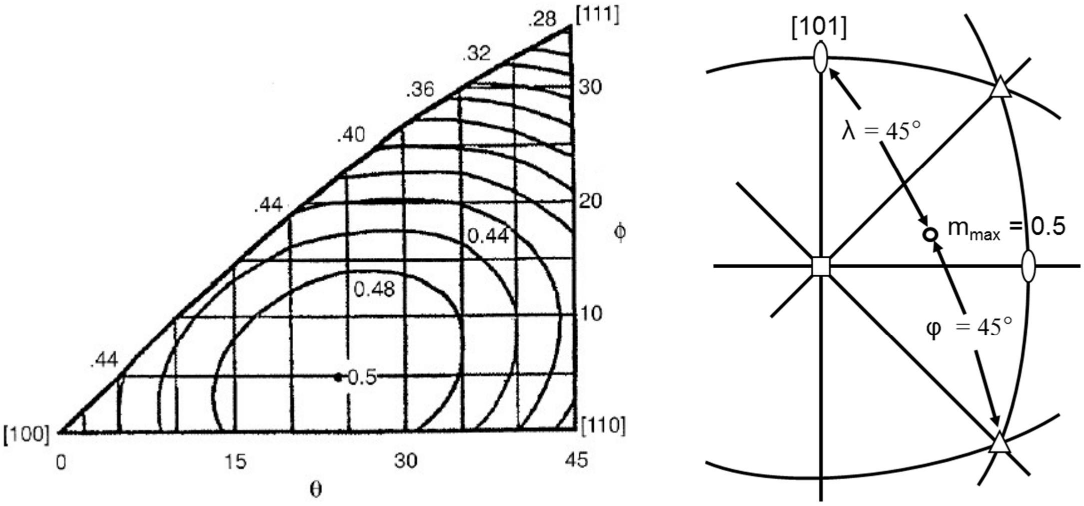

Figure 2.10: Orientation dependence of the Schmid factor for fcc single crystals [35].

If the tensile axis is located on a boundary of the basic triangle, two slip systems are equally favored. The first system is the primary slip system while the second one is in the adjoining triangle. For example, the second system is [110] (1-11), called conjugate system, if the tensile axis is located at the [100]-[111] boundary. There are two other slip systems within the triangle. One is called critical slip system with Miller indices [10-1](111). The other one is called cross slip system with Miller indices [101](1-1-1), sharing the same slip direction with primary slip system. Screw dislocations can move from the primary plane to cross slip plane when they meet precipitates. Slip systems having the same slip plane as the primary system but having different slip directions are called coplanar slip system. The slip systems of fcc crystals are shown in their favored triangles in Fig. 2.11.

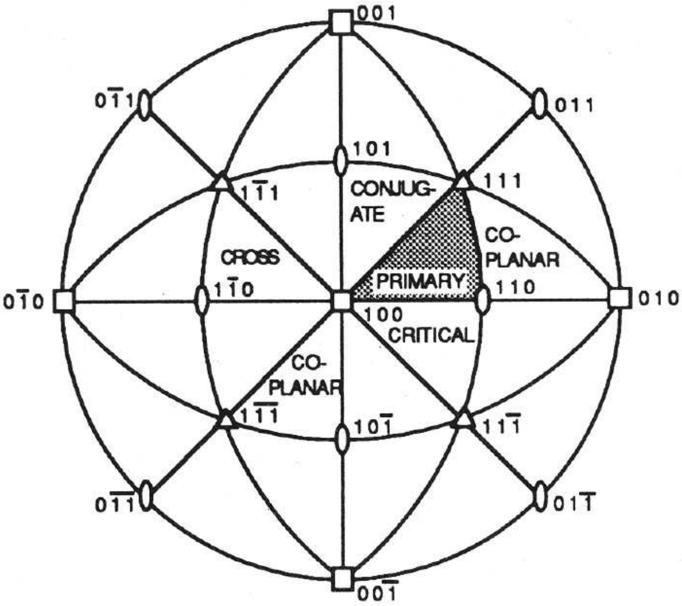

Figure 2.11: Slip systems for fcc crystals in stereographic projection [35].

2.4.3 Lattice rotation during tension

During tension, the angle between tensile axis and slip plane normal, φ, gets larger while the angle between the tensile axis and slip direction, λ, gets smaller. The changing rates of φ and λ as a function of engineering strain (ε) are written as:

$$\frac{d\varphi}{d\varepsilon} = \cot\varphi \qquad \text{(Eq. 2-4)}$$

$$\frac{d\lambda}{d\varepsilon} = -\tan\lambda \qquad \text{(Eq. 2-5)}$$

If the tensile axis lies in the plane consisted of the slip direction and the slip plane normal, $\lambda + \varphi = 90°$. In other cases, $\lambda + \varphi > 90°$. Therefore, $\cot\varphi \le \cot(90° - \lambda) = \tan\lambda$. Thus,

$$\left|\frac{d\lambda}{d\varepsilon}\right| \ge \left|\frac{d\varphi}{d\varepsilon}\right| \qquad \text{(Eq. 2-6)}$$

Equation (Eq. 2-6) shows the rotation rate of the slip direction towards the tensile axis is equal to or larger than the rotation rate of the slip plane normal away from the tensile axis. This rotation is regarded as the primary rotation, as shown in Fig. 2.12 (a).

For an fcc crystal with orientation that the tensile axis is in the primary triangle, the tensile axis rotates towards the primary slip direction [101] along a great circle until it reaches the [100] – [111] boundary of the triangle. When the tensile axis reaches this boundary, the primary slip system and the conjugate slip system are equally favored. Slips by the two systems make the tensile axis rotate towards [211] along the [100] – [111] boundary. When the tensile axis reaches [211], the rotation towards the [101] direction will cancel the rotation towards the [110] direction. Therefore, [211] is the stable end direction.

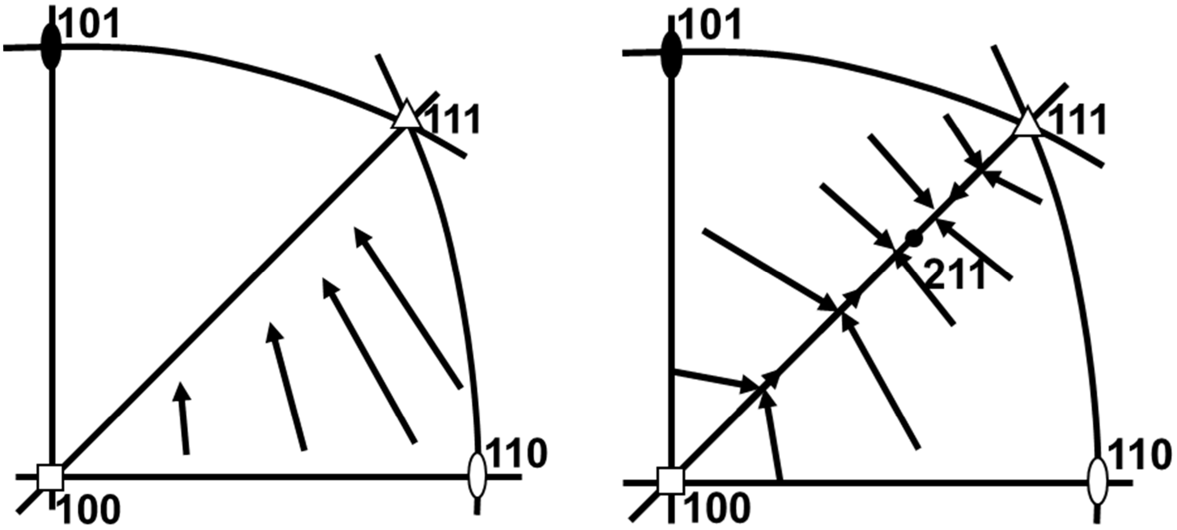

(a) Slip by [101](11-1) (b) Slip by both [101](11-1) and [110] (1-11)

Figure 2.12: Rotation of fcc crystals by slip [35].

2.5 Orientation dependence of Young's modulus in fcc crystals

The stiffness of a single crystal is anisotropic and depends on the crystallographic direction. According to the linear elasticity, strain components are linear function of stress components, which can be written as:

$$e_{ij} = s_{ijmn}\sigma_{mn} \qquad \text{(Eq. 2-7)}$$

The compliances, s_{ijmn}, have the following matrix format for the fcc structure:

$$\begin{matrix} s_{11} & s_{12} & s_{12} & 0 & 0 & 0 \\ s_{12} & s_{11} & s_{12} & 0 & 0 & 0 \\ s_{12} & s_{12} & s_{11} & 0 & 0 & 0 \\ 0 & 0 & 0 & s_{44} & 0 & 0 \\ 0 & 0 & 0 & 0 & s_{44} & 0 \\ 0 & 0 & 0 & 0 & 0 & s_{44} \end{matrix} \qquad \text{(Eq. 2-8)}$$

In order to find the Young's modulus along any direction **d**, a single tensile stress σ_d along the direction vector **d** is supposed to exert on a cubic crystal, as shown in Fig. 2.13. The axes 1, 2, 3 stand for the crystal axes [100], [010] and [001], and α, β and γ stand for the direction cosines of the vector **d** with the three axes.

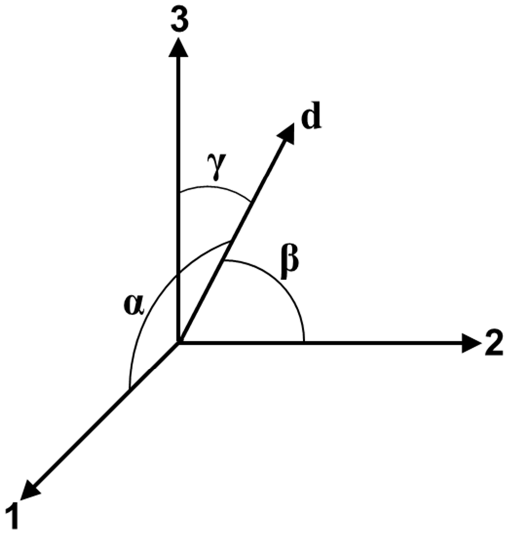

Figure 2.13: A direction vector **d** relative to the crystal coordinate.

The stress along the crystal axes can be expressed as:

$$\sigma_1 = \alpha^2\sigma_d\ , \sigma_2 = \beta^2\sigma_d\ ,\ \ \sigma_3 = \gamma^2\sigma_d\ ,\ \ \sigma_{23} = \beta\gamma\sigma_d\ ,\ \ \sigma_{31} = \gamma\alpha\sigma_d\ ,\ \ \sigma_{12} = \alpha\beta\sigma_d \qquad \text{(Eq. 2-9)}$$

According to Eq. 2-8, the corresponding strains are:

$$\begin{aligned} e_1 &= (s_{11}\alpha^2 + s_{12}\beta^2 + s_{12}\gamma^2)\sigma_d\ ,\ \ \gamma_{23} = s_{44}\beta\gamma\sigma_d \\ e_2 &= (s_{12}\alpha^2 + s_{11}\beta^2 + s_{12}\gamma^2)\sigma_d\ ,\ \ \gamma_{31} = s_{44}\gamma\alpha\sigma_d \qquad \text{(Eq. 2-10)} \\ e_3 &= (s_{12}\alpha^2 + s_{12}\beta^2 + s_{11}\gamma^2)\sigma_d\ ,\ \ \gamma_{12} = s_{44}\alpha\beta\sigma_d \end{aligned}$$

Resolving these strain components onto the d axis,

$$e_d = \left(\alpha^2 e_1 + \beta^2 e_2 + \gamma^2 e_3 + \beta\gamma\gamma_{23} + \gamma\alpha\gamma_{31} + \alpha\beta\gamma_{12}\right)\sigma_d \qquad \text{(Eq. 2-11)}$$

Substituting Eq. 2-10 into Eq. 2-11, and using ($\alpha^2 + \beta^2 + \gamma^2$) = 1 and ($\alpha^4 + \beta^4 + \gamma^4$) = [1 – 2 ($\beta^2\gamma^2 + \gamma^2\alpha^2 + \alpha^2\beta^2$)], the reciprocal of Young's modulus along the direction **d** can be expressed as:

$$1/E_d = e_d/\sigma_d = s_{11} + (-2s_{11} + 2s_{12} + s_{44})(\beta^2\gamma^2 + \gamma^2\alpha^2 + \alpha^2\beta^2) \qquad \text{(Eq. 2-12)}$$

If d is expressed by the Miller indices [hkl], then

$$\begin{aligned} \alpha &= h/\sqrt{h^2 + k^2 + l^2} \\ \beta &= k/\sqrt{h^2 + k^2 + l^2} \qquad \text{(Eq. 2-13)} \\ \gamma &= l/\sqrt{h^2 + k^2 + l^2} \end{aligned}$$

Equation 2-12 can be expressed as:

$$1/E_d = s_{11} + \frac{(-2s_{11} + 2s_{12} + s_{44})(k^2l^2 + l^2h^2 + h^2k^2)}{\left(h^2 + k^2 + l^2\right)^2} \qquad \text{(Eq. 2-14)}$$

Substituting $1/E_{[100]} = s_{11}$, and $1/E_{[111]} = (s_{11} + 2s_{12} + s_{44})/3$, Eq. 2-14 can be written as:

$$1/E_d = 1/E_{[100]} + f\left(1/E_{111} - 1/E_{100}\right) \qquad \text{(Eq. 2-15)}$$

where $f = 3(\beta^2\gamma^2 + \gamma^2\alpha^2 + \alpha^2\beta^2)$.

2.6 Deformation models of polycrystalline materials

The deformation mechanism models of polycrystalline materials are based on the properties of single crystals, although in real materials the interactions between neighboring grains make the deformation more complicated.

2.6.1 Sachs model

Sachs [36] proposed that all crystals inside the material undergo the same stress, and the tensile yield strength of the polycrystal is the average of yield strengths of all crystallites. The yield strength is

$$\sigma_y = \frac{1}{m}\tau_c \qquad \text{(Eq. 2-16)}$$

where m is the Schmid factor for the most stressed slip system and τ_c is the critical resolved shear stress. For randomly oriented fcc polycrystal, the average value of (1/m) = 2.4. Therefore, the yield strength of fcc polycrystal $\sigma_y = 2.4\tau_c$.

In Sachs model, it is assumed that only one slip system is activated in each crystallite, by which the shape compatibility cannot maintained, although the stress continuity is maintained at grain boundary. The advantage of Sachs model is that it gives a valid lower bound to the strength in uniaxial tension.

2.6.2 Taylor model

Assuming the plastic strain is identical in all grains, Taylor model satisfies the strain compatibility requirement [37-38]. If uniaxial stress σ_z is applied to the z-axis, deformation occurs by axially symmetric flow. Therefore,

$$d\varepsilon_x = d\varepsilon_y = -\frac{1}{2}d\varepsilon_z \quad \text{and} \quad d\gamma_{xy} = d\gamma_{xz} = d\gamma_{yz} = 0 \qquad \text{(Eq. 2-17)}$$

The work done on all slip systems within all grains in the unit volume is

$$dw = \sum_i \tau_c d\gamma_i = \tau_c \sum_i d\gamma_i \tag{Eq. 2-18}$$

where the critical shear stress for all slip systems is assumed to be the same and $d\gamma_i$ is the shear strain increment on individual slip systems. For uniaxial tension the work done by external force per volume is:

$$dw = \sigma_z d\varepsilon_z \tag{Eq. 2-19}$$

Therefore,

$$dw = \tau_c \sum_i d\gamma_i = \sigma_z d\varepsilon_z \quad \text{or} \quad \frac{\sigma_z}{\tau_c} = \frac{\sum_i d\gamma_i}{d\varepsilon_z} = M \tag{Eq. 2-20}$$

The M is the Taylor factor, which depends on the orientation of individual grains. The following discusses how to calculate the Taylor factor. Firstly, the external strains, $d\varepsilon_x$, $d\varepsilon_y$, $d\varepsilon_z$, $d\gamma_{yz}$, $d\gamma_{zx}$ and $d\gamma_{xy}$ relative to the 1, 2, 3 crystal axis are expressed as $d\varepsilon_1$, $d\varepsilon_2$, $d\varepsilon_3$, $d\gamma_{23}$, $d\gamma_{31}$ and $d\gamma_{12}$. Secondly, in order to represent the strains caused by the {111}<110> slip systems in fcc crystals, each slip system is given a short name, as shown in Table 2.1.

Projecting the strains caused by each slip system on the crystal axis, the expressions are as follows:

$$\begin{aligned}
d\varepsilon_1 &= (-d\gamma_{a\mathrm{II}} + d\gamma_{a\mathrm{III}} - d\gamma_{b\mathrm{II}} + d\gamma_{b\mathrm{III}} - d\gamma_{c\mathrm{II}} + d\gamma_{c\mathrm{III}} - d\gamma_{d\mathrm{II}} + d\gamma_{d\mathrm{III}})/\sqrt{6} \\
d\varepsilon_2 &= (+d\gamma_{a\mathrm{I}} - d\gamma_{a\mathrm{III}} + d\gamma_{b\mathrm{I}} - d\gamma_{b\mathrm{III}} + d\gamma_{c\mathrm{I}} - d\gamma_{c\mathrm{III}} + d\gamma_{d\mathrm{I}} - d\gamma_{d\mathrm{III}})/\sqrt{6} \\
d\varepsilon_3 &= (-d\gamma_{a\mathrm{I}} + d\gamma_{a\mathrm{II}} - d\gamma_{b\mathrm{I}} + d\gamma_{b\mathrm{II}} - d\gamma_{c\mathrm{I}} + d\gamma_{c\mathrm{II}} - d\gamma_{d\mathrm{I}} + d\gamma_{d\mathrm{II}})/\sqrt{6} \\
d\gamma_{23} &= (+d\gamma_{a\mathrm{II}} - d\gamma_{a\mathrm{III}} - d\gamma_{b\mathrm{II}} - d\gamma_{b\mathrm{III}} + d\gamma_{c\mathrm{II}} - d\gamma_{c\mathrm{III}} - d\gamma_{d\mathrm{II}} + d\gamma_{d\mathrm{III}})/\sqrt{6} \\
d\gamma_{31} &= (-d\gamma_{a\mathrm{I}} + d\gamma_{a\mathrm{III}} + d\gamma_{b\mathrm{I}} - d\gamma_{b\mathrm{III}} + d\gamma_{c\mathrm{I}} - d\gamma_{c\mathrm{III}} - d\gamma_{d\mathrm{I}} + d\gamma_{d\mathrm{III}})/\sqrt{6} \\
d\gamma_{12} &= (+d\gamma_{a\mathrm{I}} - d\gamma_{a\mathrm{II}} + d\gamma_{b\mathrm{I}} - d\gamma_{b\mathrm{II}} - d\gamma_{c\mathrm{I}} + d\gamma_{c\mathrm{II}} - d\gamma_{d\mathrm{I}} + d\gamma_{d\mathrm{II}})/\sqrt{6}
\end{aligned} \tag{Eq. 2-21}$$

Due to the constant volume during tension, the first three equations are not independent, i.e. $d\varepsilon_1 + d\varepsilon_2 + d\varepsilon_3 = 0$. Therefore, there are five independent relations in Eq. 2-21, which means at least five slip systems are required to be activated to satisfy a shape change.

In Eq. 2-21, there are five independent equations but 12 unknowns. Thus, Eq. 2-21 cannot be solved directly. To solve this problem, Taylor assumed the shape changes on the premise that the work done by slip is minimized and the critical shear stress is the same for all active systems and all slip systems work harden at the same rate, i.e.

$$\sum_i \tau_i d\gamma_i = \tau \sum_i d\gamma_i = \min \qquad \text{(Eq. 2-22)}$$

Taylor proposed that the minimum work would require slip on as few systems as geometrically possible, i.e. 5 systems, and the other slip systems are inactive. Therefore, he calculated the shear strains and found the average Taylor factor to be M = 3.06 for randomly oriented fcc polycrystal, i.e. $\sigma_y = 3.06\tau_c$, which corresponds to an upper bound. The prediction by Taylor model was in reasonable agreement with the experimental flow curve of a randomly oriented aluminum polycrystal.

2.6.3 Bishop and Hill model

Considering the stress states which could physically activate the required slip systems, Bishop and Hill made an equivalent analysis to Taylor. They first figured out 28 stress states that would activate five or more slip systems simultaneously [39-40], using the principle of maximum plastic work, i.e.

$$dw = \sum_1^3 \sum_1^3 \sigma_{ij}\varepsilon_{ij} = \max \qquad \text{(Eq. 2-23)}$$

These 28 stress states make the stress on either six or eight systems reach the critical shear stress, which explains Taylor’s results that the same minimum of Taylor factor, M, were produced by several combinations of five slip systems.

Bishop and Hill model and Taylor model are based on the same assumptions and give the same solutions. One assumption is that all grains deform homogeneously and experience the same shape change in a polycrystal, which ensures the deformation compatibility. Another one is that the critical shear stress is the same for all active slip systems.

2.7 General description on texture

Both man-made and natural polycrystalline materials, composed of large quantities of single crystals, exhibit preferred orientation of crystallites, which has a profound influence on the anisotropy of physical and mechanical properties. The preferred orientations of crystallites termed as crystallographic texture or texture, form during growth or deformation and can be further modified by heat or mechanical treatments to optimize the properties of final products. It is a big challenge to explore deforming behavior of grains in a material with highly preferred orientations, and to interpret relationship between the direction dependent mechanical properties (with respect to sample coordinates) and the texture.

Representation of texture is made according to the orientation distributions of crystallites with respect to a given sample coordinate [41]. To achieve this, two coordinate systems are needed. One is the sample coordinate system K_A = (X, Y, Z), made in terms of the external shape of a sample, which corresponds to the rolling direction (RD), transverse direction (TD) and normal direction (ND) as in the case of rolled plate. The other one is the crystal coordinate system K_B = (X', Y', Z') consisted of the crystal axes which are chosen according to the crystal symmetry. For instance, [100], [010] and [001] are chosen for the cubic structures. The orientation of a crystallite is then described by the rotation g, which transforms K_A into K_B as shown in Fig. 2.14.

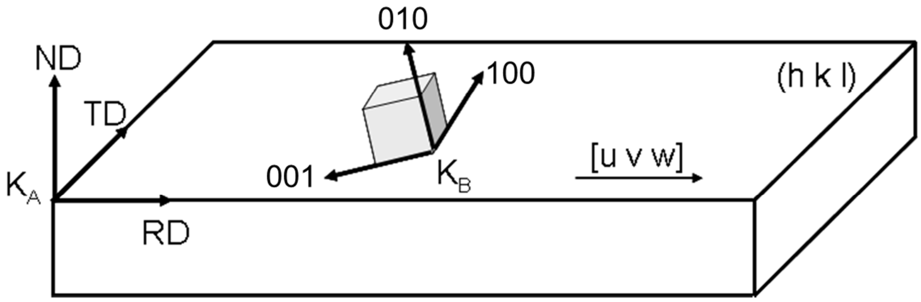

Figure 2.14: Schematic illustration of the sample and crystal coordinate systems.

$$K_B = g.\, K_A \qquad (K_A \frac{\quad}{} g \longrightarrow K_B) \qquad \text{(Eq. 2-24)}$$

The rotation g can be represented in different ways, for example, by Miller-indices (hkl) [uvw] or by Euler angles {φ_1, Φ, φ_2}. As to the Miller-indices, (hkl) refers to crystallographic planes parallel to the RD-TD plane, and [uvw] refers to the crystallographic direction parallel to the RD as in the case of rolled plate, shown in Fig. 2.14. As for the case of Euler angles, they are defined as three rotation angles around three axes. After rotations according to these three angles successively, the sample coordinate system is overlapped with the crystal coordinate system. Following the terminology defined by Bunge [41] and assuming that the crystal coordinate system is first coincide with the sample coordinate system as shown in Fig.2.15 (a), the three rotations are as follows:

1. about the z**'** axis = [001] through the angle φ_1 (Fig. 2.15 (b)).

2. about the x**'** axis = [010] through the angle Φ (Fig. 2.15 (c)).

3. about the new z**'** (in its new orientation) = [001] through the angle φ_2 (Fig. 2.15 (d)).

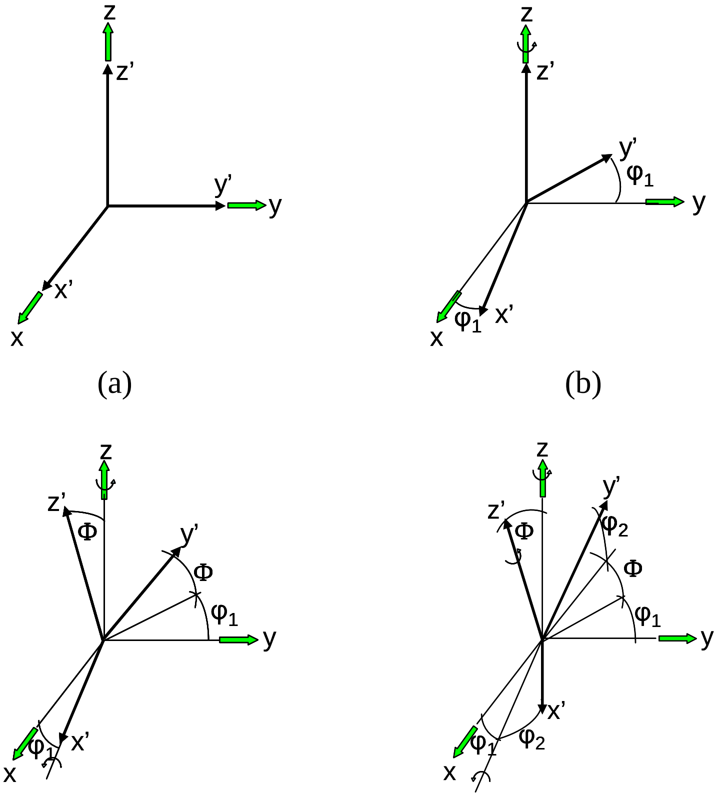

(a) (b)

(c) (d)

Figure 2.15: Schematic interpretation of Euler angle.

The rotation g is represented by the three Eulerian angles φ_1, Φ, φ_2, which describes the orientation of the crystal in the sample.

$$g = \{ \varphi_1, \Phi, \varphi_2\} \quad \text{(Eq. 2-25)}$$

It is convenient to plot the three angles in Cartesian coordinates in three-dimensional space, called orientation space or Euler space (see figure 2.16). All possible orientations can be represented within the range of $0° \leq \varphi_1 \leq 360°$, $0° \leq \Phi \leq 180°$ and $0° \leq \varphi_2 \leq 360°$ in Euler space. An individual crystal is represented by several points in this space due to the symmetry of the crystal. For example, all equivalent orientations of an fcc material can be represented by 24 different sets of Euler angles [42]. Therefore, the ODF (orientation distribution function) can be represented in a reduced Euler space. The reduced Euler space for the ODF of a sample possessing fcc structure and orthorhombic symmetry is within the range of $0° \leq \varphi_1 \leq 90°$, $0° \leq \Phi \leq 90°$ and $0° \leq \varphi_2 \leq 90°$.

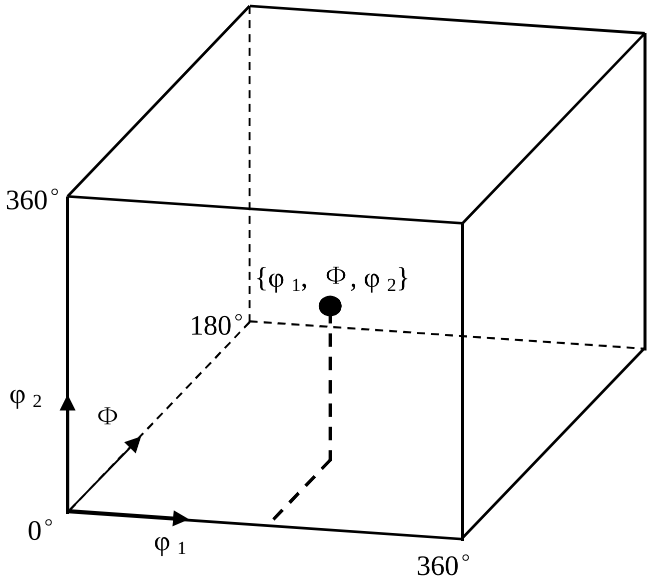

Figure 2.16: Euler space of triclinic crystal symmetry or asymmetric unit [41].

The orientation distribution function (ODF) of crystallites is defined by the volume fraction of crystallites having their orientation g within an infinitesimal orientation element dg.

$$f(g) = \frac{dV(g)/V}{dg} \qquad \text{(Eq. 2-26)}$$

The orientation distribution function f (g) is given as the multiples of random distribution (mrd) in such way that it equals 1 for every g in the case of random distribution, i.e.

$$f_{random} = \oint f(g)dg = 1 \qquad \text{(Eq. 2-27)}$$

ODF is normally calculated from measured pole density distribution functions (P_{hkl} (α, β), pole figures), the procedure of which is called pole figure inversion. Pole figure gives information about the probability of poles of lattice plane which is located at a specific position with respect to the sample coordinate. The probability is then projected on a plane using equal area or stereographic projections. Two angles are used to characterize a position on the pole figure. One is called polar angle, α, which describes the distance from the center of the pole figure. The other one is called azimuth angle, β, which describes the rotation of the poles around the polar axis, starting from a specified reference condition. Pole figures can be directly measured by diffraction techniques such as laboratory X-ray, synchrotron radiation and neutron. However, pole figures exhibit orientation distribution information in two dimensions. It may occur that the poles of different orientations overlap with each other. And for many cases such as laboratory X-ray, the coverage of the pole figure is not complete, which further reduces the texture information in pole figures. To overcome the above mentioned disadvantages, ODF is used for quantitative analysis of texture, which represents orientation density of crystallites in three dimensions. Normally, ODF is not completely determined by one pole figure. Two or more pole figures are needed, the number of which depends on both crystal symmetry and sample symmetry [43]. There are two mathematical ways of calculating ODF from pole figure data. One is series expansion method introduced by Bunge [41] and Roe [44] . The other one is direct inversion method or is called WIMV (Williams-imhof-Matthies-Vinel) method [45]. In the present work, the iterative series expansion method (ISEM) introduced by Dahms and Bunge [46] is used to calculate the orientation distribution function. Using this method, a pole figure is expanded in a series of spherical harmonic functions:

$$P_{hkl}(\alpha,\beta)=\sum_{l=0}^{l\max}\sum_{v=l}^{N(l)}F_l^{v}(hkl).\dot{K}_l^{v}(\alpha,\beta) \qquad \text{(Eq. 2-28)}$$

$$F_l^{v}=\int_{\alpha=0}^{\pi/2}\int_{\beta=0}^{2\pi}P_{hkl}(\alpha,\beta).\dot{K}_l^{*\mu}(\alpha,\beta)\sin\alpha d\alpha d\beta \qquad \text{(Eq. 2-29)}$$

where *l* is series expansion degree; *F* are the pole figure coefficients; *k* are the symmetrized spherical harmonic functions. The *F* coefficients can be calculated using the iteration of the experimentally determined pole density distribution, called pole figure inversion. In this case the normalized pole figure intensities are utilized:

$$F_l^{v}(hkl)=\frac{4\pi}{2l+1}\sum_{\mu=1}^{M(l)}C_l^{\mu v}.\dot{k}_l^{*\mu}(hkl) \qquad \text{(Eq. 2-30)}$$

Eq. 2-28 to Eq. 2-30 show calculations of the unknown *C* coefficients of orientation distribution function from the known F coefficients. Once the *C* coefficients are calculated, the ODF expanded in series of generalized spherical harmonics can be achieved:

$$f(g)=f(\varphi_1,\phi,\varphi_2)=\sum_{l=0}^{l\max}\sum_{\mu=l}^{M(l)}\sum_{v=l}^{N(l)}C_l^{\mu v}.\ddot{T}_l^{\mu v}(\varphi_1,\phi,\varphi_2) \qquad \text{(Eq. 2-31)}$$

In the Eq. 2-28 to 2-31 the symbol ´*´ denotes the complex conjugate, and dots over the harmonic function denotes the symmetrization of the functions. M (*l*) and N (*l*) are the number of independent values for each expansion degree, *l*, after the sample and crystal symmetry, respectively. As mentioned above, ODF is calculated from pole figure data. The number of pole figures needed for ODF calculation depends upon the crystal symmetry of the sample. For fcc materials, three pole figures, (111), (200) and (220), are needed such as in the case of aluminum.

2.8 Deformation textures of fcc metals

2.8.1 Fiber texture

Deformations having axial symmetry such as tension, drawing, extrusion and compression, of polycrystalline materials make special crystallographic direction <uvw> of crystallites rotate parallel to the loading axis, and make other crystallographic directions distribute with equal probability around the loading axis. This kind of orientation distribution is termed <uvw> fiber texture [47].

Before the advent of ODF analysis, early investigations of Hibbard [48-49] showed that the <111> fiber texture in Cu, Ag, Au, Ni, Pb and Al after drawing, and a mixture of <111> and <100> fiber texture in certain Cu alloys. Grewen and Wassermann [50] concluded that the initial texture had a profound influence on the development of fiber texture and can lead to misinterpretations. Bunge [51] investigated the textures of Al wires by drawing, which had initial textures of both <111> fiber and <100> fiber. After 84% of deformation, the texture was still a mixture of the two components, but after 99% deformation, the <100> component completely disappeared. He concluded that in pure aluminum, the <100> component was not stable while the <111> was the stable component. McHargue et al. [47] made systematic investigations on the fiber texture, which showed that the extrusion texture of 99.99% pure aluminum depended on temperature and strain rate. A duplex <111> + <100> fiber texture was observed at all temperatures with slow strain rate and up to 232°C with fast rate. With the fast strain rate, at 343°C, a <115> texture was observed, but at 454°C the observed texture was <118>. Besides, a sample extruded slowly at low temperature had a texture consisted of 92% <111> component compared with 76% <111 > component at room temperature. The authors concluded that the <100> texture component was largely due to recrystallization and the main effect of strain rate was to increase the temperature of aluminum, which led to the <115> or <118> “recrystallization" fiber texture at high strain rates. The researchers also concluded that the <100> component had a lower dislocation density than the <111> component.

However, English and Chin [52] demonstrated that the axial deformation texture of fcc metals was a mixture of <111> and <100> fibers, and it was not attributed to the occurrence of recrystallization. In their study, several fcc metals ranging from high stacking fault energy (SFE) to low SFE were investigated, with particular attention paid to several very low SFE alloys. After 99% deformation by drawing, they obtained the volume percentage of the two fibers and the volume percentage of the <100> fiber was plotted as a function of SFE, as shown in Fig. 2.17. As SFE decreases, the percentage of <100> component increases, but at very low SFE area, it decreases again with the decreasing SFE. This trend was confirmed by the literatures such as [52-54].

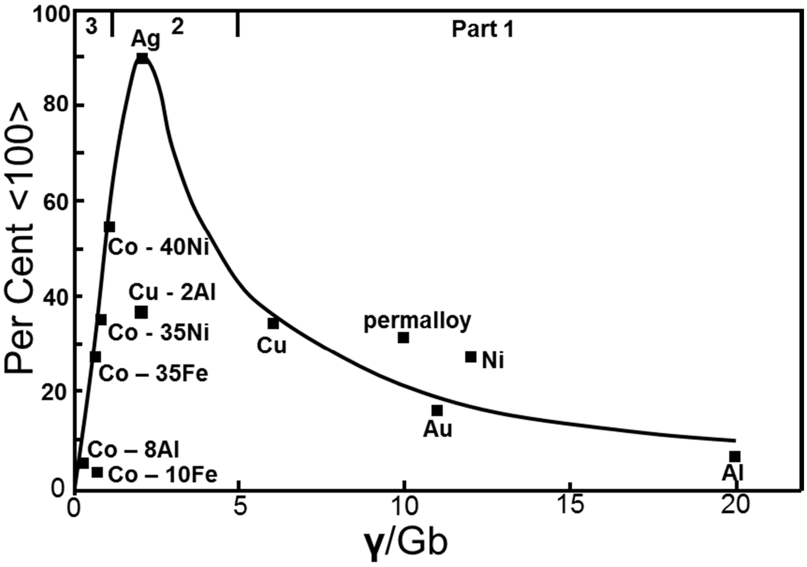

Figure 2.17: The percent of <100> component as function of stacking fault energy [52].

Several deformation mechanisms such as cross slip, latent hardening and twinning were applied to interpret phenomena in Fig. 2.17 in [53-55]. According to these interpretations, the curve in Fig. 2.17 can be divided into three parts. Each part of the curve has its own deformation mechanism. Part 1 is associated with the ease of cross slip, corresponding to the high SFE materials such as aluminum or to high temperature deformation behavior. When all slip systems are hardened equally, six slip systems are activated in the <111> component, which have 3 different slip planes and 3 different slip directions, i.e. 3 pairs of collinear systems. This kind of cross slip was observed in aluminum in [56-57]. Part 2 is associated with mechanical twinning, corresponding to intermediate SFE materials. For fcc materials, the twinning system is on (111) plane along [11-2] direction. Twinning happens in fcc materials if the SFE is low or if the deformation temperature is very low. Twinning transposes the <111> orientation into <115> orientation, which will rotate towards <100> through slip. Therefore, when twinning happens, the relative proportion of the <100> component will increase. Part 3 shows the <100> component decreases with the decreasing SFE. Several interpretations have been proposed to explain it. They are as follows.

1). When twinning becomes so easy that all orientations favor twins, the <100> fiber orientation loses its preferential role [54].

2). Venables [58] concluded that, with decreasing SFE, twin nucleation is made easier, but propagation of twin may become more difficult, which indicates that the amount of twinning will reach a maximum for some intermediate SFE, as shown in Fig. 2.17. Therefore, the percentage of <100> fiber will also reach a maximum at some intermediate SFE.

3). Another interpretation of part 3 is related to the occurrence of deformation faulting. A (111)[01-1] dislocation is split into two {111}<112> type Shockley partials which are connected by a strip of stacking fault. The width of stacking fault is inversely proportional to the SFE of the material. The separated partials move in a "zig-zag" way firstly along [-12-1] and then along [11-2], which has the same effect as the (111)[01-1] slip. Hu et al. [59] proposed that when the width of stacking fault is beyond a certain value, i.e. the SFE is lower than a certain value, the slip direction switches from <110> to <112>, which makes the dominance of the <111> component in low SFE materials. Chin [53] also concluded that intrinsic faulting, which enhances coplanar slip for very low SFE alloys, favors <111 > fiber texture.

The above mentioned mechanisms can be concluded as follows: the ease of cross slip of high SFE metals primarily attributes to the form of <111> component. The preference of <111> component in very low SFE metals is probably related to twinning in all the grains or coplanar slip or intrinsic faulting. The dominance of <100> component in intermediate SFE metals can be ascribed to the mechanical twinning.

2.8.2 Rolling texture

Numerous investigations on the texture evolution during rolling were carried out before the ODF was invented. Therefore, the results of early studies were mainly expressed by pole figures. And at that time research works were considerably performed on Cu, Cu-Zn alloy and Al. Two types of rolling textures develop during rolling of α-brass and copper, which are called brass type texture and copper type texture, respectively, and the two types of textures are found in most fcc metals after rolling [59-60]. The differences between the two type textures were first studied by Hu et al. [61]. Figure 2.18 shows the (111) pole figures of the two type textures. The brass type texture consists of two components, i.e. the brass component {110}<112> and the Goss component {110}<100>. The copper type texture is composed of three components, i.e. copper component {112}<111>, S component {123}<634> and brass component {110}<112>. The locations of the components are also indicated in Fig. 2.18.

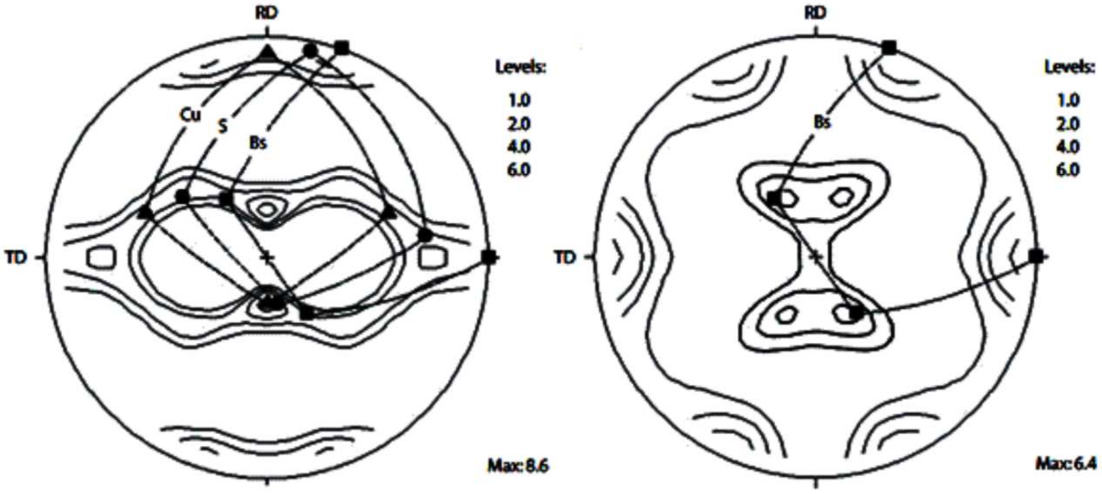

(a) (b)

Figure 2.18: (111) pole figures for (a) pure copper and (b) brass (Cu-37%Zn) [5].

The transition from brass type to copper type texture and vice versa was observed in the early studies. It depends on the alloy composition and deformation temperature, mainly associated with SFE changes. Solute addition can change the SFE. Investigation of the effect of solute addition on texture transition showed that a minimum amount of a certain solute is required to initiate texture transition, and for complete transition, a certain amount of the solute is required, which is different for different kinds of solute [62-64].

Hu and co-worker [65-67] made systematical investigation on temperature induced texture transition in electrolytic copper, high-purity silver and 18-8 austenitic stainless steel. The results showed that deformation temperature has an influence on the transition between copper type texture and brass type texture. The texture changes from brass type to copper type as the temperature increases, whereas it changes from copper type to brass type as the temperature decreases. For instance, rolled at room temperature (RT), copper has copper type texture, but rolled below a certain temperature under RT, it has brass type texture. Another example is silver. Silver possesses brass type texture when it is rolled at RT, but it has a copper type texture when the rolling temperature is beyond a certain value.

In low SFE materials, the development of brass type texture is due to the mechanical twinning or deformation faulting. In high SFE materials, the development of copper type texture is due to cross-slip. Some critical explanations of texture development are summarized as follows.

1). Transition owning to cross-slip

Dillamore and Roberts [57] and Smallman and Green [56] proposed that the formation of copper type texture is attributed to the extensive cross-slip. Cross-slip rate is dependent on the SFE of the material and deformation temperature. Dillamore and Roberts declared that brass type texture develops by normal slip in all fcc materials. For low SFE materials, plastic deformation continues by the normal slip and the final texture remains brass type, because cross-slip is difficult to start. But for high SFE materials, cross-slip makes the reorientation of crystallites, which transforms the brass type texture into copper type texture. Texture transition is related to the composition of an alloy and the deformation temperature. The addition of elements decreases SFE, resulting in difficulty in cross-slip, whereas the thermal fluctuation can activate cross-slip at high temperature.

2). Transition owing to non-octahedral slip

Haessner [68] proposed that brass type texture is related to the normal octahedral slip, whereas the copper type texture results from the slip on {100} planes along <110> directions.

Haessner claimed that cubic slip is more difficult to occur in low SFE materials, because the dislocation partials on the {111} planes gets wider with decreasing SFE. Slip on the {100} planes was observed in aluminum [69], which considerably depended on the initial orientation of the crystallites and on deformation temperature.

3). Transition owing to mechanical twinning

The {111}<112> type mechanical twinning is believed to be an additional plastic deformation mechanism besides slip. It rotates the copper component (112)[111] to the (552)[115] component, and further slip rotates the (552)[115] component to (110)[001] Goss component. On the contrary, the brass component (011)[211] maintains its orientation during deformation. The rolling textures developed in silver single crystal support this mechanism [70].

4). Transition owing to deformation faulting

The influence of deformation faulting on the texture evolution in fcc metals was investigated by Hu, chine and Goodman [59]. Their study was performed on single crystals of high-purity Cu and a Cu alloy containing 4% Al, with (110)[1-12] and (112)[11-1] orientations.

Deforming the single Cu crystal with (110)[1-12] orientation (brass component), the orientation keeps stable. For Cu, the slip systems are {111}<110>. The primary and conjugate slip systems are (111)[01-1] and (11-1)[101], respectively. If the primary slip system (111)[01-1] was initiated to large extent, the normal of the slip plane (111) rotates to the normal of rolling plane while slip direction [01-1] rotates to the rolling direction, which leads to decrease of the resolved shear stress in the active slip system and increase of the resolved shear stress in the conjugate slip system (11-1)[101]. When the conjugate slip system (11-1)[101] is initiated, the crystal starts to rotate in the opposite direction. Therefore, the orientation changes caused by these two systems counteract each other. Whereas in the Cu-4%Al crystal the orientation density of the brass component decreased until the crystal was deformed into two brass-oriented crystals. Deformation faulting or slip by partials will result in slip on {111}<112> systems. The (111)[2-11] and (111)[-12-1] slip systems will not cause orientation change, but the other two systems, (11-1)[112] and (111)[11-2], will cause orientation changes which cannot counteract each other. Therefore, for low SFE metals such as silver, the (110)[1-12] orientation is expected to be unstable.

Deforming single crystals with (112)[11-1] orientation (copper component), the copper crystal maintains its initial orientation, whereas the Cu-4% crystal shows a strong orientation spread and a strong component at (552)[-1-15].

In copper crystal the (-111)[110] and (1-11)[110] slip systems make the crystal rotate towards rolling direction. During rotation, the resolved shear stress on these two slip systems decreases. At the same time, the resolved shear stress in the other two systems, (111)[-101] and (111)[0-11], increases. When it reaches the CRSS, the two slip systems are initiated, which makes the crystal rotate in the opposite direction. Therefore, in Cu crystal, the orientation keeps unchanged. In Cu-4%Al crystal, deformation faulting forms by slip on the (111)[-1-12] system, resulting in developing a (552)[-1-15] component. As the deformation goes further, the matrix rotates to the (111)[11-2] orientation, while the (552)[-1-15] component rotates to (110)[001] orientation, which means the original (112)[11-1] orientation splits into 2 orientations, (111)[11-2] and (110)[001].

However, Mecking [71] made similar investigation on copper single crystal and brass single crystal with the same orientations, and claimed that the deformation behavior difference between these two crystals was attributed to the mechanical twinning.

Summarizing the rolling texture studied by pole figure, it is evident that at room temperature, there is a texture transition from the brass type to copper type with increasing SFE. Deformation faulting and/or mechanical twinning are considered to be responsible for the brass type texture, while cross-slip and/or newly activated slip systems lead to the formation of copper type texture.

As described in section 2.7, texture can be represented in Euler space by ODF. It is a normal practice to exhibit ODF in discrete sections through Euler space. ODF for fcc materials are usually presented by φ_2 sections with 5° per section. The intensity distribution in individual sections can be displayed by contour lines or different colors or different gray values.

Figure 2.19 (a) shows the copper type texture and (b) the brass type texture in Euler space by φ_2 sections with 5° per section. Hirsch and Lücke [72] and Kallend and Davies [73] reported similar results as shown in Fig. 2.19. Bunge and Haessner [74] found the same ODF results of rolled pure copper as Hirsch. Copper type texture is commonly described by copper, S and brass components, while the brass type texture by brass and Goss components. The Miller indices and Euler angles of these ideal components are listed in Table. 2.2

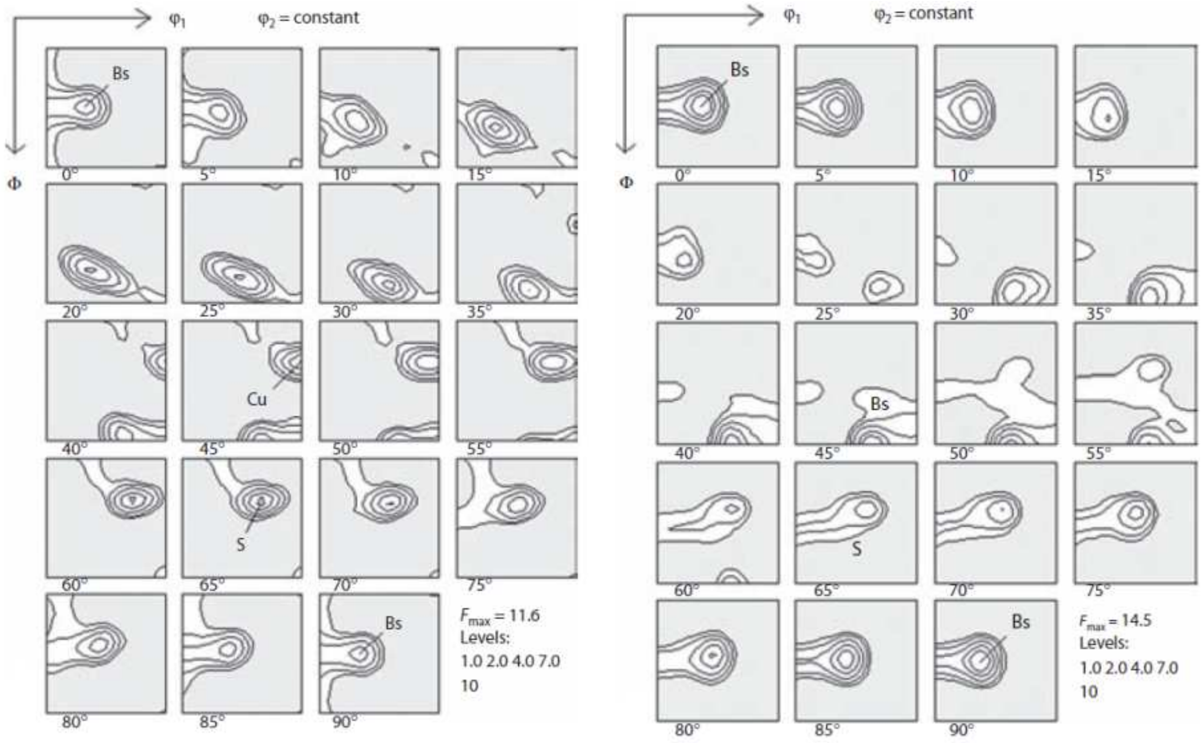

(a) (b)

Figure 2.19: ODF of rolling textures of fcc metals: (a) pure copper, (b) brass (Cu-37%Zn)[5].

Table 2.2: The Miller indices and Euler angles of the ideal components.

Designation	Miller indices {hkl}<uvw>	Euler angles φ_1 Φ φ_2
Copper	{112}<111>	90° 30° 45°
S	{123}<634>	59° 34° 65°
Brass	{011}<211>	35° 45° 0°/90°
Goss	{011}<100>	0° 45° 0°/90°

However, description of the rolling texture by ideal components is not adequate. The copper type texture can be described as a spread of orientations from copper component through S component to Brass component (β fiber), and the brass type from brass component to Goss component (α fiber). Figure 2.20 (a) shows the two orientation tubes in Euler space in the branch within the range of 45° ≤ Φ ≤ 90°. In fcc materials, the intensity variations along α fiber and β fiber give information about the texture differences. Figure 2.20 (b) shows the intensity changes along β fiber for pure Cu and Cu alloys with different amount of Zn, from which one can see how the texture changes with decreasing SFE.

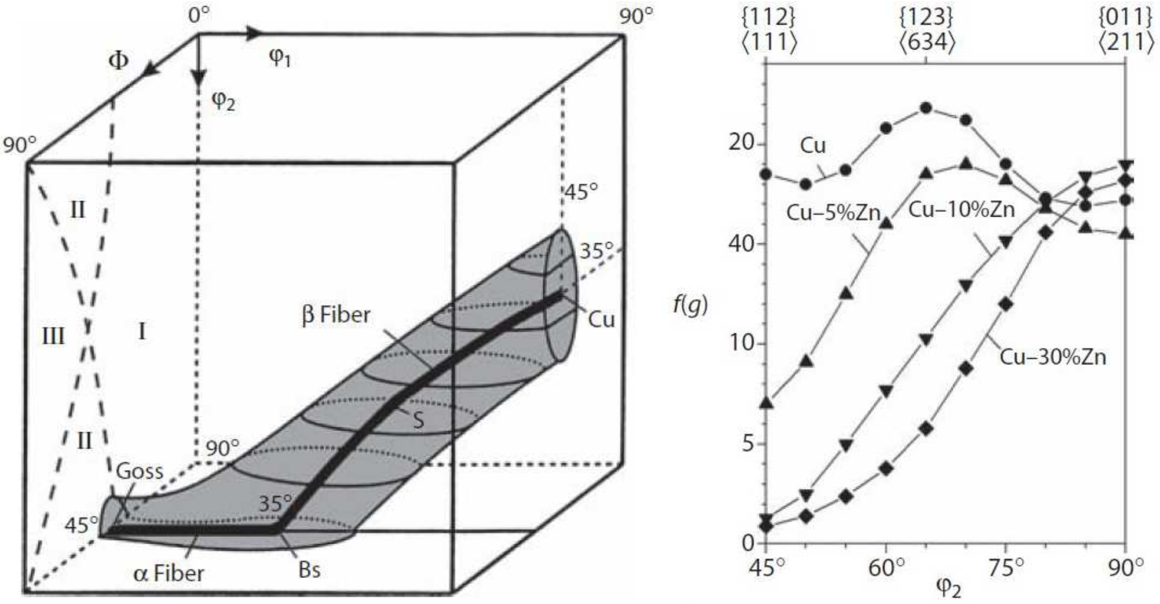

(a) (b)

Figure 2.20: (a) Positions of α and β fibers in Euler space [72]; (b) intensity variations along β fiber of pure Cu and different Cu-Zn alloys after 95% reduction [5].

Hirsch et al. determined the rolling texture of different Cu-Zn alloys at room temperature and found that with decreasing SFE, the texture transited from Copper type to brass type texture [72]. They reported that in low Zn alloys, the orientation density of copper component increases as the deformation increases. However, in higher Zn alloys, for example, the 70/30 brass, the orientation density of copper component, firstly, increases up to around 50% reduction. With further deformation, the copper component shifts from {552}<115> to {332}<113> [75].

The influence of initial texture on final texture was also investigated by Hirsch et al. At room temperature, in rolled aluminum, they found that a brass texture could be obtained if the initial texture mainly consisted of Goss component. If the initial texture was mainly cube component, a strong S component was produced. If the initial cube or Goss component was rotated 45° around the compression axis, a strong copper component was obtained.

The influence of precipitation states on the final texture was investigated by Engler et al. and Lücke and Engler [76-77]. The size, volume fraction and distribution of precipitations affect the deformation behavior through interactions between the precipitates and dislocations. Figure 2.21 shows the rolling texture of an Al-1.8%Cu alloy with different aging treatments before rolling.

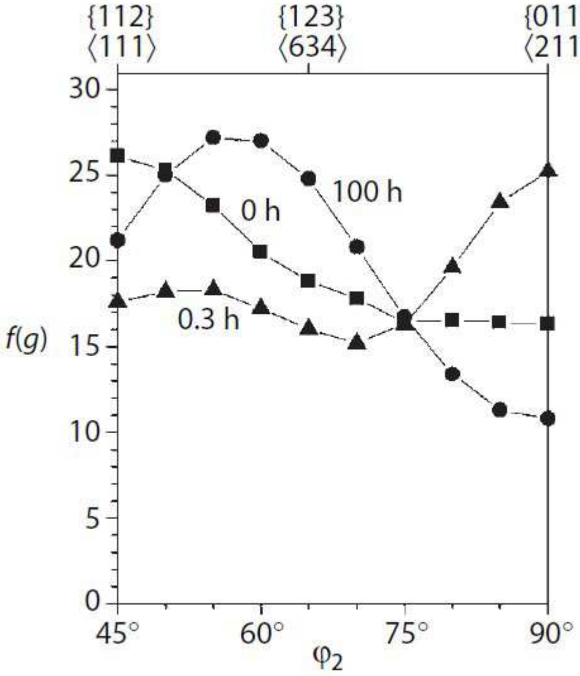

Figure 2.21: After 95% rolling reduction, orientation density variations along β fiber of the rolled Al-1.8%Cu with different aging treatments ahead of rolling [76].

2.9 Texture measurement using high energy X-ray

2.9.1 A short introduction to Synchrotron radiation

When electro-charged particles such as electrons or positrons move in a speed close to light in storage ring and are forced to change flight direction by magnetic field, photos ranging from the infrared to hard X-rays, i.e. energy ranging from meV to around 100 MeV, are generated in the direction tangential to the forward direction, which is called synchrotron radiation. The magnetic components generating the magnetic fields are different from beamline to beamline, including bending magnets, wigglers and undulators, which will lead to different brilliance and divergence of the X-ray beam, as shown in Fig. 2.22. The energy range of the generated X-ray can be chosen by adjusting the spacing of the magnets. Therefore, it can meet the needs of many investigations. At present, there are many synchrotron facilities around the world, as shown in Table 2.3.

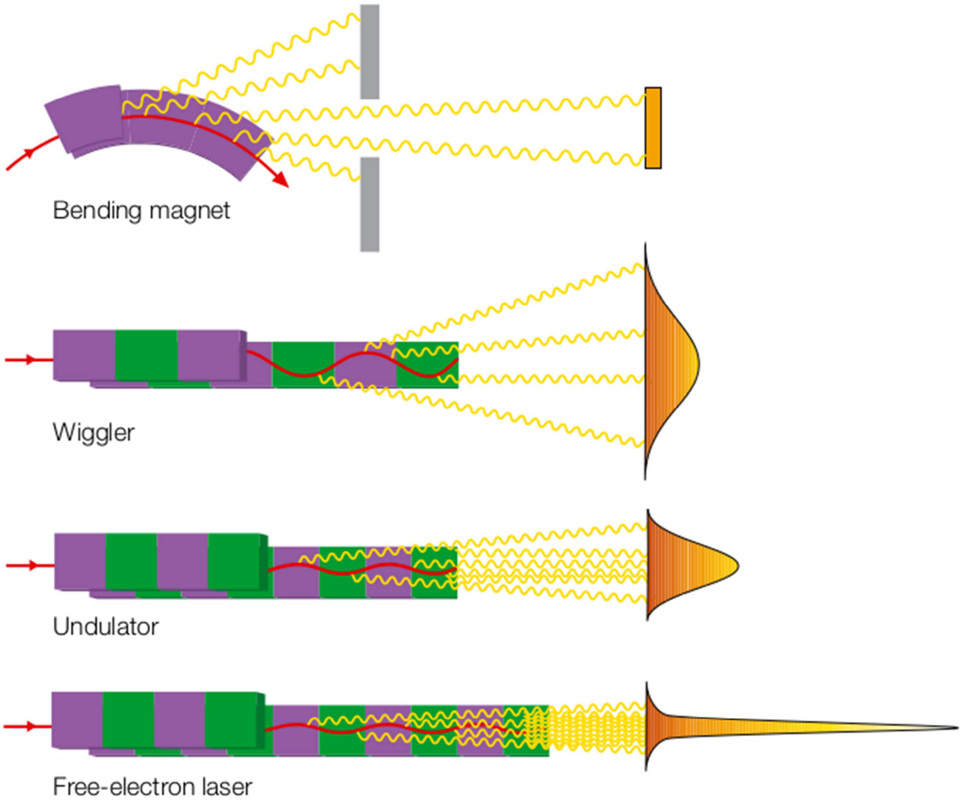

Figure 2.22: Synchrotron radiation generated by different magnetic components (for comparison, the synchrotron radiation generated by free electron laser is also shown) [78].

Table 2.3: Some synchrotron facilities around the world.

Name	Country	Name	Country
ALBA	Spain	Diamond	UK
ANKA	Germany	ELETTRA	Italy
APS	USA	ESRF	France
AS	Australia	HSRC	Japan
BESSY	Germany	LNLS	Brazil
BSRF	China	SLS	Switzerland
CESLAB	The Czech Republic	SOLEIL	France
CLS	Canada	Spring-8	Japan
DAFNE	Italy	SSLS	Singapore
DELTA	Germany	SSRF	China
DESY	Germany	SSRL	USA

Compared to laboratory X-rays, synchrotron radiation has, for example, the following advantages: 1). high intensity, which makes it possible to make measurement in a short time when coupled with fast read-out detector; 2) high brilliance, which leads to high angular resolution and makes it possible to use beam size in the scale of μm or even smaller; 3) high penetration depth, comparable with thermal neutrons, as shown in table 2.4; 4) sensitivity to magnetic properties due to the resonance effects of the polarized synchrotron radiation.

Table 2.4: Penetration depth of laboratory X-ray, synchrotron radiation and thermal neutrons.

	Energy /keV	Wavelength /Å	Penetration depth/mm				
			Al	Mg	Ti	Fe	Pb
Laboratory X-ray Cu - Kα	8.05	1.54	0.074	0.14	0.011	0.004	0.004
Laboratory X-ray Co - Kα	6.92	1.79	0.048	0.09	0.007	0.023	0.003
Synchrotron radiation	100	0.12	22	34	8	4	0.14
Thermal neutrons	6.88	1.80	96	61	17	8	27

2.9.2 Texture measurement using synchrotron radiation

Synchrotron radiation provides high energy X-rays with high brilliance, wherein the beam size is in the order of μm, which makes it possible to measure the local texture in a small volume of a polycrystalline material. Since the middle of 1990s, many researchers have been making contributions to the development of texture measurements using synchrotron radiation and to the ways of interpreting the measured data such as those in [79-82]. Furthermore, in situ measurement with synchrotron radiation is getting more and more important, because it makes possible to detect small changes in materials in a very short time.

Transmission method with monochromatic beam is normally applied to the texture measurement using synchrotron radiation. In the present study, the beamline at HEMS (High Energy Materials Science) P07B at Petra III DESY Hamburg, Germany, is taken as an example to illustrate how to carry out texture measurement using synchrotron radiation. Figure 2.23 shows the sketch of the beamline set-up for texture measurement. The white X-ray beam from the synchrotron radiation is monochromatized by a single bounce monochromator (SBM), a flat water-cooled Laue crystal Si (220), the resulting wavelength of which is around 0.1425 Å. Beam size (height and width) can be adjusted by the collimator in the monochromator chamber, ranging from 10 μm (or smaller) to 500μm. The sample is mounted on a ω rotation stage, which can be translated in vertical direction Z and in horizontal direction X (perpendicular to the incident beam). Through X and/or Z translation, local textures at different positions of a sample can be determined sequentially. Area detectors such as Mar345 and PE (Perkin Elmer) can be used, the read-out time of which are around 3 minutes or several seconds, respectively. The images obtained from the detector record the intensity variations along the Debye-Scherrer rings from different {hkl} lattice planes which satisfies the Bragg’s equation with respect to the incident beam. Figure 2.24 shows an image from NIST standard Al_2O_3 plate and an image from a rolled Aluminum plate, both of which are collected by PE detector. For the NIST standard Al_2O_3 plate, crystallites are randomly distributed such that there are no intensity variations along the Debye-Scherrer rings, as shown in Fig. 2.24 (a), whereas for the rolled aluminum, texture can be immediately indicated by the intensity variations along the Debye-Scherrer rings, as shown in Fig. 2.24 (b).

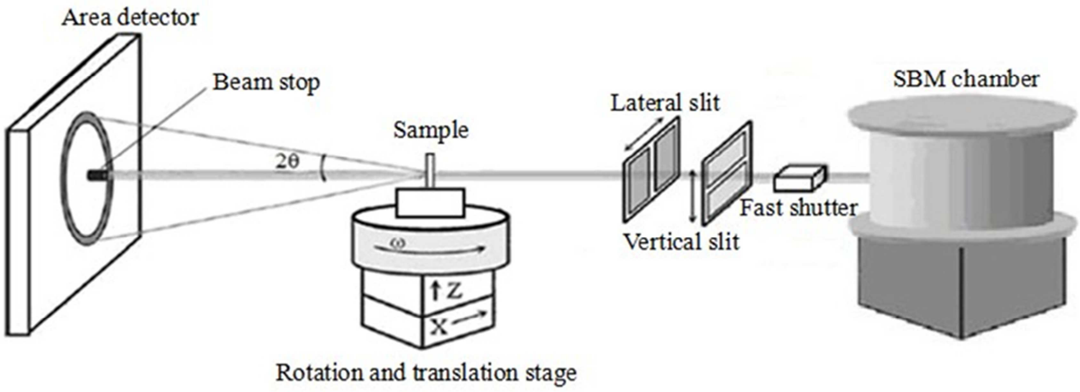

Figure 2.23: Sketch of the beamline set-up for texture measurement in HEMS P07B.

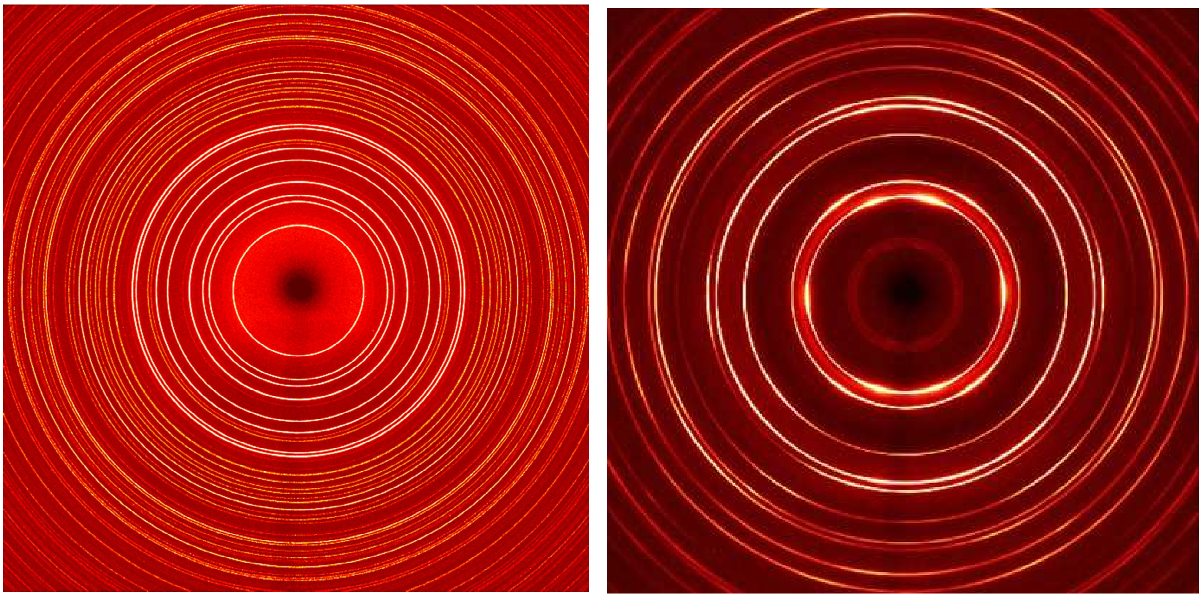
(a) (b)

Figure 2.24: Images from the PE area detector: (a) NIST standard Al_2O_3 plate, (b) a rolled aluminum alloy.

A {hkl} Debye-Scherrer ring from an image collected at one ω position covers only one circle in the {hkl} pole figure, as shown in Fig. 2.25. In order to cover the whole pole figure, a sample should be rotated by the ω stage and images are collected at each ω angle. For a texture which is not sharp, ω rotation can be carried out by 5° per step from 0° to 180°, but for sharp texture, it is better to use smaller step width. The sharper the texture, the smaller the step width has to be.

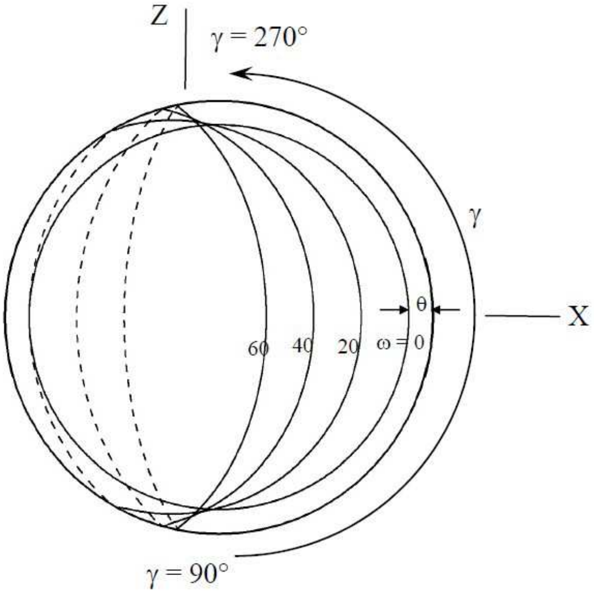

Figure 2.25: The coverage of Debye-Scherrer rings in a pole figure [83].

2.10 Lattice strain determination using high energy X-rays

2.10.1 Definition of lattice strain

When an external stress is exerted to a polycrystalline material, the stress and strain generated inside the material vary from grain to grain, depending both on single crystal anisotropy and individual grain orientations. Measuring the lattice spacing at a specific stress gives a way to characterize the lattice strains of different oriented grains. X-ray or neutron diffraction provides a non-destructive method to measure the lattice spacing of some specific grain sub-sets which are oriented in a special direction with respect to sample coordinate, for example, the LD in tensile experiment. The penetration depth of laboratory X-rays is in the order μm which can only be used to measure the surface of a material, whereas the penetration depth of X-rays from synchrotron radiation or neutrons can reach the order of cm, which makes it possible to measure average lattice spacing of a great amount of sub-set grains within a sample. In the present work, the monochromatic X-rays from synchrotron radiation (high energy X-rays) are used to determine the lattice spacing.

Diffraction occurs when the Bragg's law is satisfied, which has the following expression:

$$2d_{hkl}\sin\theta_{hkl} = \lambda \qquad \text{(Eq. 2-32)}$$

where d_{hkl} is the lattice spacing of a special oriented {hkl} lattice planes, θ_{hkl} is the diffraction angle of {hkl} lattice planes and λ is the wavelength of the radiation.

Lattice strain is determined using the following equation:

$$\varepsilon_{hkl} = \frac{d_{hkl} - d_{hkl}^{i}}{d_{hkl}^{i}} \qquad \text{(Eq. 2-33)}$$

where d_{hkl} is the measured lattice spacing under different applied stresses and d_{hkl}^{i} is the lattice spacing of the starting material.

2.10.2 Lattice strain in fcc randomly oriented polycrystals

The lattice strain developments of texture free fcc polycrystals such as aluminum, copper and austenitic stainless steel during uniaxial tensile load were investigated by Clausen et al. [84-85], which correspond to low and high elastic anisotropy, respectively. The elastic anisotropy is expressed by $2C_{44}/(C_{11} - C_{12})$ where C_{44}, C_{11} and C_{12} are the elastic stiffness constant of a material, aluminum being 1.22, Cu being 3.21 and austenitic stainless steel being 3.77. Results in [84, 86] show that different lattice planes deform elastically in the elastic region. In this region the elastic anisotropy controls the stress-strain response of individual {hkl} lattice planes. The material with small elastic anisotropy exhibits smaller lattice strain differences among different {hkl} lattice planes under a given external load than the ones with high elastic anisotropy. However, for the three materials mentioned above, under the same external load, the {111} lattice planes show the stiffest elastic response (smallest lattice strain), while the {200} lattice planes show the lowest stiffness (largest lattice strain). The {111} and {200} lattice planes corresponds to the highest and the lowest stiffness crystallographic lattice planes, respectively. Moreover, the slopes of the stress-lattice strain curve of individual {hkl} lattice planes in the elastic region give the Young’s modulus of {hkl} lattice planes. The Young’s modulus difference of aluminum between {111} and {200} is much less than those of Cu and austenitic stainless steel due to the lower elastic anisotropy.

When plastic deformation starts, stress redistribution among different lattice planes begins in both parallel and perpendicular to LD. For example, in aluminum parallel to LD, the {111} planes are the stiffest in elastic regime, but in plastic regime, {111} planes experience highest lattice strain at a given load. The {200} planes behave in an opposite way, experiencing the lowest lattice strain. However, the measured lattice strain data are not perfectly consistent to the modeling calculations, especially in the direction perpendicular to the LD[83, 84]. In [84], the authors attributed the deviation to that a grain with certain {hkl} plane normal lying perpendicular to the loading axis can have many different crystallographic directions lying parallel to the tensile axis. Thus, grains with {hkl} plane normal perpendicular to the LD can behave very differently to one another, resulting in the average lattice strain sensitive to the distribution of grain orientations. Moreover, Clausen et al. [87] also investigated an Al-2%Mg, but the simulated results were much different from the measured results. The authors gave the following reasons for the discrepancy. Firstly, the self-consistent model simulates the plastic deformation by multi-slip on the {111}<110> slip systems, but it does not take into account the effect of interaction between the slip systems. Secondly, for low elastic anisotropic materials such as aluminum, the anisotropic behavior is dominated by the plastic anisotropy, which makes the simulated data deviate from the measured data much. Thirdly, the single-crystal elastic constants used in their model are from pure aluminum.

Agnew et al. [88] investigated the lattice strain evolution of copper and stainless steel at finite strain and found that grain orientation is a major contributor to the variation in the internal strain within a single {hkl} reflection, and grains contributing to a {hkl} reflection in the direction perpendicular to LD have a variety of orientations parallel to LD. Kanjarla et al. [89] found that lattice strains in perpendicular to LD are more sensitive to the local neighborhood interaction than those in LD. Daymond et al. [20] investigated a textured (less than 3 mrd) austenitic stainless steel and concluded that if the loading axis is parallel to RD, the induced stresses are similar to the rolling process; consequently, the grains deform in the same directions in which they are pre-strained. If the loading axis is parallel to TD, the majority of grains have to deform in a different direction from the pre-strained direction, making the lattice strain less influenced by pre-strain. Pang et al. [90] investigated the generation of intergranular strains in Al7050 alloy during load and unload, and found that intergranular strains vary in different crystallographic directions which depend on the elastic and plastic properties, texture of the material and different deformation mechanisms producing different intergranular stresses. For instance, the intergranular stresses caused by rolling are more complicated than those by uniaxial tension. Dawson et al. [19] reported that the direction moduli ratio (E_{111}/E_{200}) has a profound influence on the lattice strain development during elastic to plastic transition, and they found that using $E_{111}/E_{200} = 1.7$ for AA-5182 alloy, the calculated lattice strains by finite element simulations are more close to the measured lattice strains (the direction modulus ratio for pure aluminum is 1.2), which indicates that single crystal anisotropy in alloys is higher than that of pure aluminum. The experimental data of above mentioned results are from almost texture free materials using neutron diffraction. However, there are also several investigations of lattice strain evolution using synchrotron radiation [91-93], which focuses on smaller volume and needs less time.

2.10.3 Diffraction pattern measurement using synchrotron radiation

In situ measurement during tensile loading using synchrotron radiation coupled with fast read-out area detector, has an advantage over neutron diffraction that exposure time and read-out time are considerably short so that one needs not stop tensile machine during irradiating a sample, whereas significant stress release always occurs using neutrons. Therefore, synchrotron radiation only averages a very small range of strains during exposure time if the loading speed is relatively low. Thus, there is no stress release influence on the measured lattice strain.

There is only one difference between beamline set-up for lattice strain measurement and the beamline set-up for texture measurement at HEMS P07B at Petra III DESY Hamburg, Germany. It is that a universal tensile machine (UTM) is mounted on the rotation and translation stage. The UTM was originally designed for neutron texture measurements [94], the maximum load of which is 20 kN. The attached load cell and Linear Variable Differential Transformer are used to monitor the applied load and sample displacement, both of which are written in a file generated by the main control program. Diffraction pattern measurement can be made under different loads, from which one can obtain different information simultaneously such as finger print of the measured material (d-value list), crystallographic texture (intensity variations), macros strain (peak shift) and micro strain and grains size (line broadening) from the complete Debye-Scherrer rings. Figure 2.26 shows the images collected at 0 kN and UTS. Details of the Debye-Scherrer ring changes can be observed, even though the texture does not change much due to the small deformation.

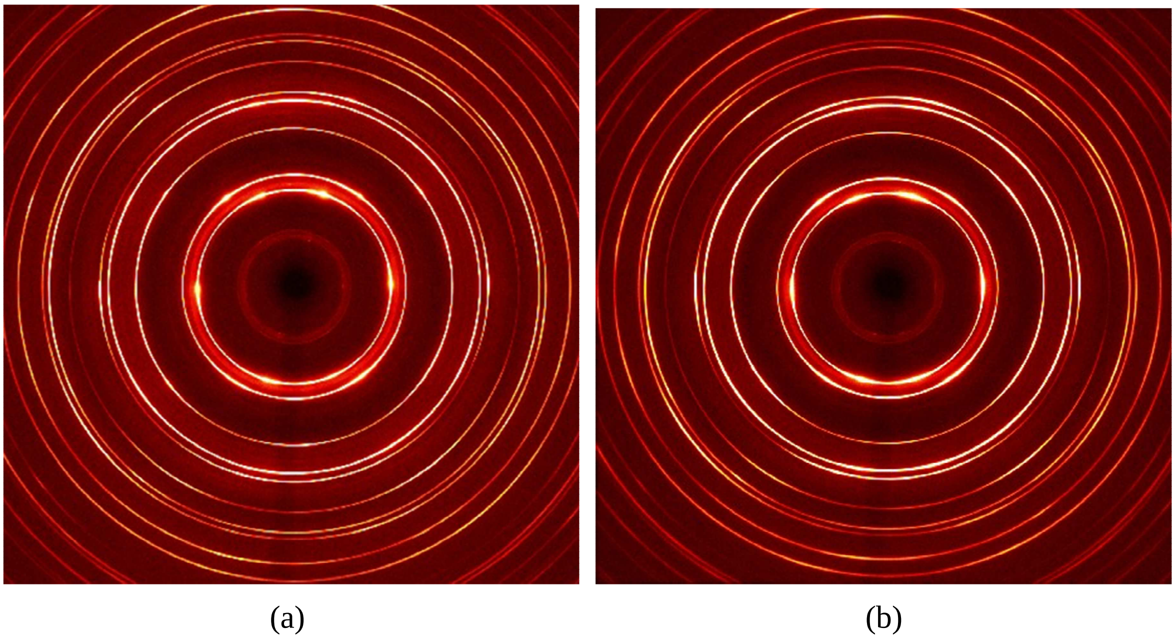

(a) (b)

Figure 2.26: Images collected at different load, (a) at 0 kN, (b) at UTS (10.8 kN).

In order to get how the special oriented grains such as those with plane normal parallel to the LD and those with plane normal perpendicular to the LD, behave during tension, one needs to integrate the sectors along these two directions using the software Fit2D [95], as shown in Fig. 2.27 (a). The angular range for the sector is 10° along the γ angle, i.e. the information got from the sector is averaged from grains whose plane normal are within 10° of the specific direction. After integrating the sector, one can get the corresponding spectrum, as shown in Fig. 2.27 (b).

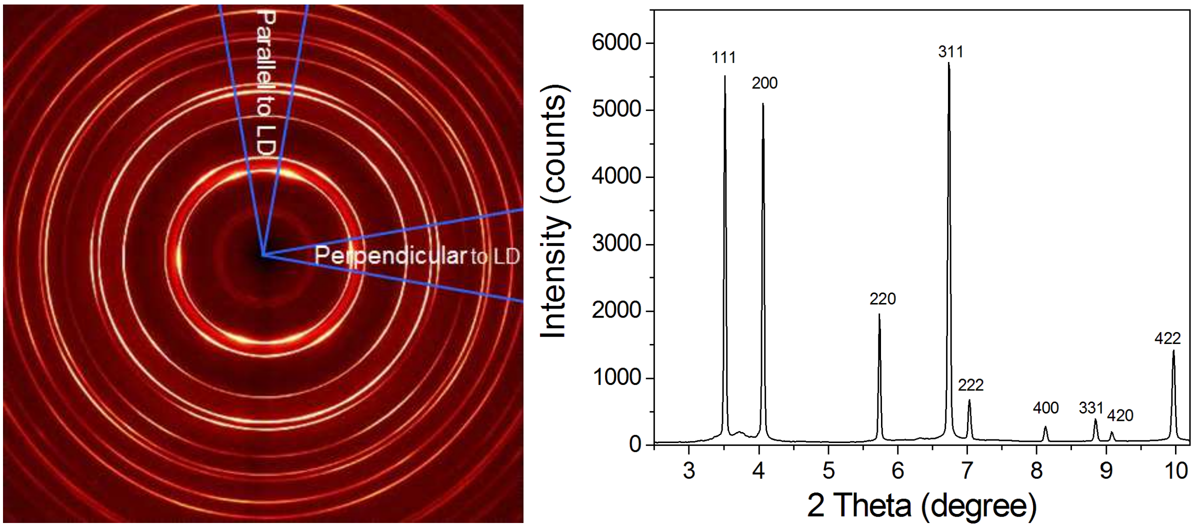

(a) (b)

Figure 2.27: (a) Integration sectors along LD (cake parallel) and along perpendicular to LD (cake perpendicular), (b) the integrated spectrum along LD.

Precise peak positions should be obtained to calculate the lattice spacing of {hkl} planes according to the Bragg's equation. In order to achieve this, a peak shape function is chosen to fit the experimental peak. The choice of peak shape function depends on the facility which is used for the measurement. Several peak shape function may be used such as Gauss function and Pseudo-Voigt function. The peak position differences determined by the Gauss function and Pseudo-Voigt function is in the order of 10^{-4} for the HEMS P07B, which is almost within the error bar. However, for a series of diffraction pattern measurements, one needs to use the same peak function to fit all the spectra. In the present work, Gauss function is used to fit the diffraction peaks. After fitting each peak, peak position is obtained in terms of 2-theta value. Dividing this value by two and using Eq. 2-32, the lattice spacing of special {hkl} planes is obtained. After that, the lattice strain at different load can be calculated using Eq. 2-33.

2.11. Estimation of dislocation density using modified Williamson-Hall plot

X-ray diffraction line broadening analysis is widely applied to characterize the defects in crystalline materials. Provided that the broadening is caused only by the coherently diffraction domains, Scherrer equation [96] can be used to evaluate the domain size using the full width at half maximum (FWHM) of the diffraction peak:

$$\beta = \frac{k\lambda}{D\cos\theta} \qquad \text{(Eq. 2-34)}$$

where β is the FWHM of the diffraction peak after instrument correction; k is constant; θ is the diffraction angle; λ is the wavelength of the X-ray; D is the domain size. Supposing the broadening is caused solely by micro strain, the micro strain can be calculated according to the function given by Stokes and Wilson [97]:

$$\beta = 2\xi\tan\theta \qquad \text{(Eq. 2-35)}$$

where ξ is the micro strain. However, in most cases, line broadening, besides instrumental broadening, is caused simultaneously by strain and size broadening, which are ascribed to the lattice defects and small coherently diffraction domains, respectively. According to the kinematical scattering theory, either crystallite smaller than 1000 nm or abundant enough lattice defects can broaden X-ray diffraction peaks. With regard to dislocations, the dislocation density should be larger than 5×10^{12} m^{-2} [98].

Strain and size broadening can be separated on the basis that size broadening is independent on the length of diffraction vector, whereas strain broadening is dependent on the length of diffraction vector. There are two commonly used ways for peak broadening analysis. One is Williamson-Hall plot (W-H) which is based on the FWHM or the integral breadth of the diffraction peak profile [99]. In Williamson-Hall plot, FWHM or integral width are expressed according to the reciprocal unit β* (β* = βcos(θ)/λ, where β is FWHM or integral width; θ is the diffraction angle; λ is the wave length of the X-rays.) as a function of d* (d* = 2sin(θ)/λ). Fitting this plot by linear regression method, the intercept indicates coherently diffraction domain size, and the slope gives the value of micro strain. The other one is Warren-Averbach (W-A) procedure which applies Fourier coefficients to analyze the peak profile [100-101]. In this method, the real parts of Fourier coefficients of the intensity distribution of the diffraction profile are the product of the size coefficient and the distortion coefficients. However, the preciseness of both methods depends on the source of X-ray which should have small instrumental broadening and small divergence.

Strain anisotropy makes the FWHM or integral width in Williamson-Hall plot not increase monotonously as the absolute value of the diffraction vector increases due to the nonuniform strain broadening [102-103]. In order to take strain anisotropy into account when making peak broadening analysis by Williamson-Hall plot, dislocation model based on mean square strain of dislocation has been suggested in [104-107], which assumes the strain broadening is caused by dislocations. The method is called modified Williamson-Hall [108]. In present article, the modified Williamson-Hall plot will be used, which has the following expression:

$$\Delta \mathrm{K} \cong \frac{\gamma}{\mathrm{D}} + \left(\frac{\pi\,\mathrm{M}^2\mathrm{b}^2}{2}\right)^{\frac{1}{2}} \rho^{\frac{1}{2}} K \sqrt{\overline{C}} + O(K^2\overline{C}) \qquad \text{(Eq. 2-36)}$$

where D, b and ρ are the coherently diffraction domain size, absolute value of Burgers vector of dislocation and dislocation density, respectively. γ equals 0.9 when using FWHM into analysis, and it equals 1 when using integral width into analysis. ΔK = cosθ [Δ(2θ)]/λ, and Δ(2θ) is the FWHM of the diffraction peak. M is called dislocation arrangement parameter [107, 109], and $M = Re^*\rho^{1/2}$, where Re is the effective outer cut-off radius of dislocations. K is the modulus of the diffraction vector, equaling 2sinθ/λ. O stands for the higher order term of $K^2\overline{C}$. $\overline{C}$ is the average contrast factor of dislocations, the value of which depends on the relative orientations among diffraction vector, Burgers vector and line vector of dislocations and the elastic constants of the materials [106, 109-110]. For cubic polycrystalline material, the contrast factor can be obtained by the fourth order polynomials of Miller indices as follows [111-112]:

$$\overline{C} = \overline{C}_{h00}\left(1 - \mathrm{q}\mathrm{H}^2\right) \qquad \text{(Eq. 2-37)}$$

where $\overline{C}_{\mathrm{h00}}$ is the average contrast factor of the {h00} reflections; q is dependent on the proportions of edge and screw dislocations and on the elastic constants of the investigated material; $H^2 = (h^2k^2 + h^2l^2 + k^2l^2) / (h^2 + k^2 + l^2)^2$.

3. Experimental procedures

3.1 As-received material and chemical composition

The as-received material is a commercial AA 7020 rolled plate with T6 heat treatment. The chemical composition of the material is listed in Table 3.1. The thickness of the as-received plate is 29.7 mm, as shown in Fig. 3.1.

Table 3.1: Chemical composition of the studied material in weight percent.

	Zn	Mg	Fe	Mn	Zr	Cu	Si	Ti	Al
AA7020	4.172 ± 0.014	1.215 ± 0.006	0.319 ± 0.009	0.300 ± 0.001	0.148 ± 0.004	0.078 ± 0.001	0.033 ± 0.001	0.013 ± 0.001	Balance

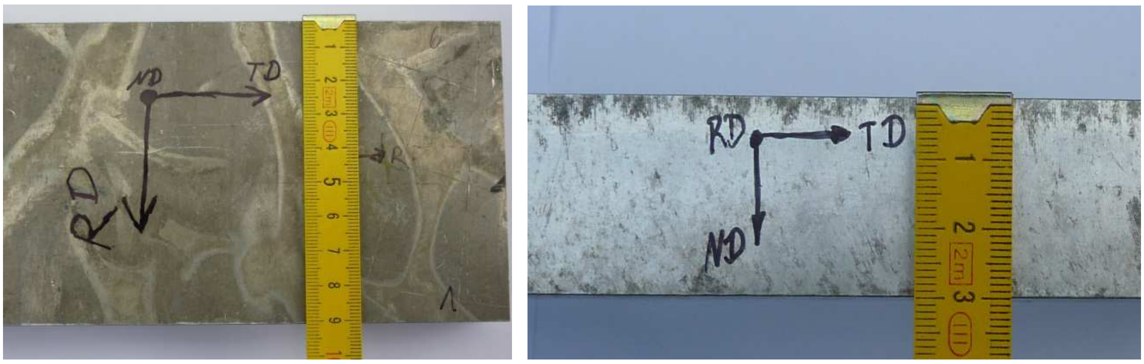

Figure 3.1: The as-received AA 7020-T6 plate.

The as-received material, in general, exhibits the rolling texture of high SFE fcc materials, the orientation components of which spread from the copper orientation {112}<111> through S orientation {123}<634> to the brass orientation {011}<211> in Euler space.

3.2 Sample preparations

3.2.1. Round tensile sample from 7.5 mm below the surface of the as-received plate

Two round samples were cut with its center line at 7.5 mm below the surface of the as-received plate, the axis of which were parallel to the RD. The dimensions of the samples were made according to DIN 50515 with diameter of 6 mm, as shown in Fig. 3.2. One sample was used to investigate the texture evolution. The other one was used to investigate the lattice strain evolution and dislocation evolution during uniaxial tension. The maximum orientation density is around 10 mrd for the round samples.

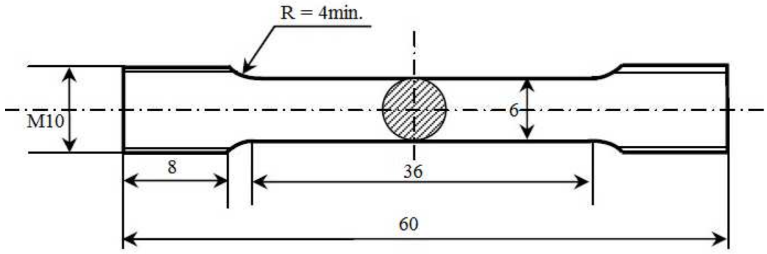

Figure 3.2: Sketch of the round tensile sample (mm).

3.2.2. Flat tensile sample from the center of the as-received AA 7020-T6 plate.

The flat samples were cut with its center line at 14.5 mm below the surface of the as-received plate. The dimensions of the samples are shown in Fig. 3.3. The samples were cut along RD, 45° to RD and 90° to RD, respectively. These samples are used to investigate the anisotropic behavior through lattice strain evolution.

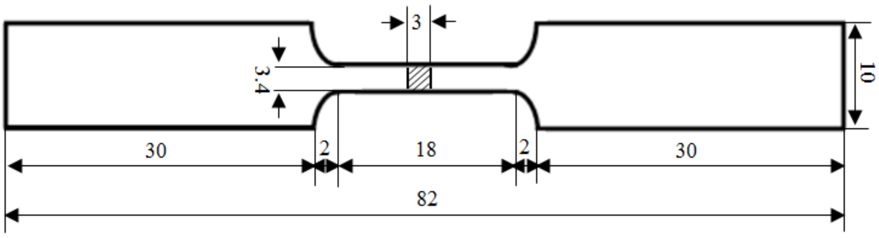

(a) Sample dimensions (mm)

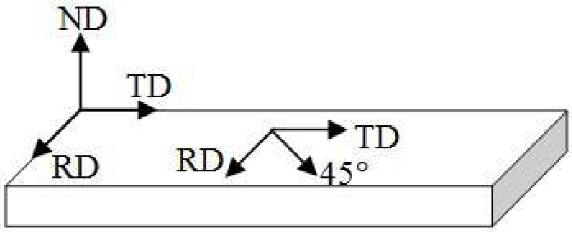

(b) Sample cutting directions

Figure 3.3: Sketch of the flat tensile sample (mm) and cutting directions from the as-received AA 7020-T6 plate.

3.2.3. Sample for texture gradient

The sample for texture gradient was cut from the as-received AA 7020-T6 plate through the thickness, as shown in Fig. 3.4. The dimensions of the sample are 7.00mm x 6.30 mm x 29.70 mm.

Figure 3.4: Sample for texture gradient investigation.

3.3 In situ pole figure measurements under different load

In situ pole figure measurements under different load were carried out at the high energy X-ray beamline HEMS P07B at PETRA III (DESY, Hamburg). The X-ray beam from the storage ring was monochromatized by a single bounce monochromator (SBM) consisted of two flat water-cooled Laue crystals Si(111) and Si(220), with which the energy can be changed between 53 and 87 keV. For the incomplete pole figure measurement, the resulting 87 keV beam (X-ray wavelength around 0.1423 Å) was chosen. The used beam size was 0.5×0.5 mm^2 and sample-detector distance was 1100 mm. The round sample was fixed in the UTM which can reach the maximum load of 20 kN [113-115], and the UTM was mounted on the rotation and translation stage. Only incomplete pole figure measurement can be carried out due to the shafts of the UTM, as shown in Fig. 3.5. The ω angle range for the incomplete pole figure measurement was from -65° to 65°. The incomplete pole figure measurement was carried out by discrete scanning method with 5° per step. The in situ tensile measurement was performed at room temperature with a loading speed of 5×10^{-4} mm/s till failure. The diffracted beams, Debye-Scherrer rings, were recorded by Perkin Elmer XRD 1622 detector, a kind of fast read-out area director which has 2048×2048 pixels with pixel size of 200×200 μm^2. With the above mentioned parameters, one incomplete pole figure measurement takes around 6 minutes. The orientation distribution function (ODF) was calculated from measured incomplete (111), (200) and (220) pole figures by MTEX [116-117].

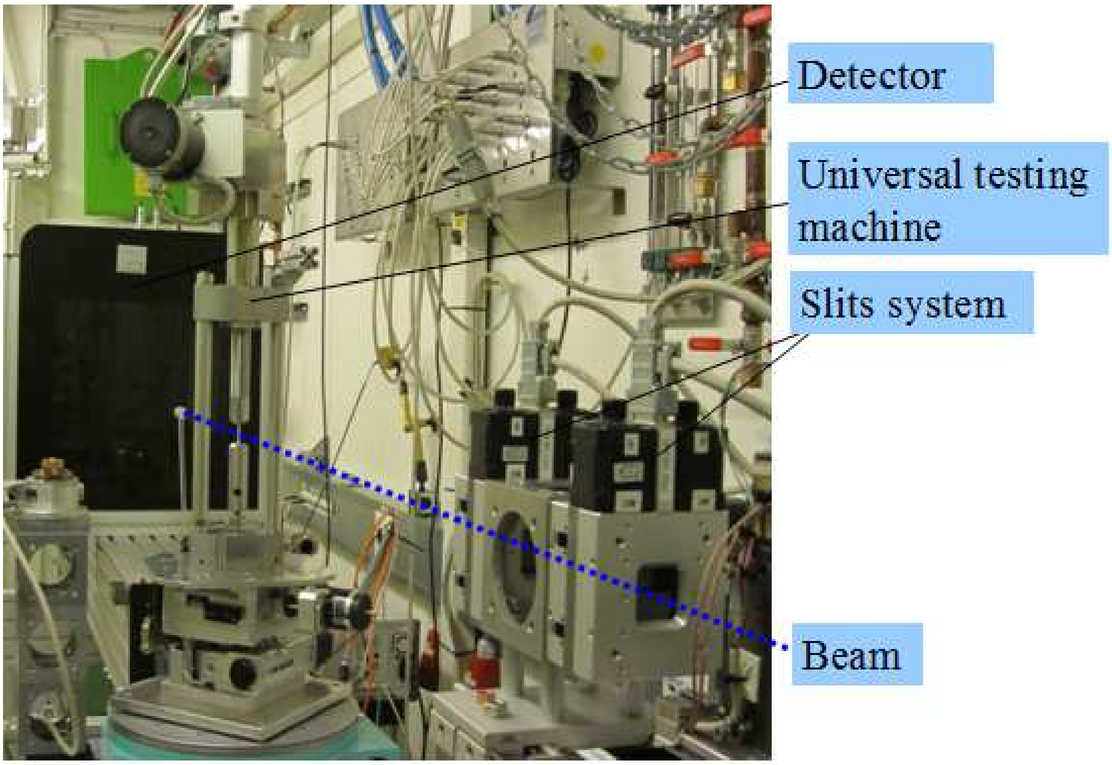

Figure 3.5: Photo of the beamline set-up for in situ texture evolution, lattice strain evolution and dislocation evolution in HEMS P07B.

3.4 In situ diffraction pattern measurements for the round sample

Diffraction pattern measurements can be carried out without stopping the loading machine using synchrotron diffraction coupled with fast read-out area detector. The beamline set-up was the same as the one shown in Fig. 3.6. The beamline set-up parameters were the same as those described in the section 3.3. The ω angle was fixed at 0° for all the diffraction pattern measurements. There were totally 386 measured positions at different loads, but it is enough to characterize the lattice strain evolution using less points. The measured points at different loads are shown in Fig. 3.6 (a). The analyzed points for lattice strain evolution are shown in

Fig. 3.6 (b). However, for the dislocation evolution, all the measured points were analyzed. The 5 regions are divided according to the lattice strain evolution, which will be discussed in chapter 5.

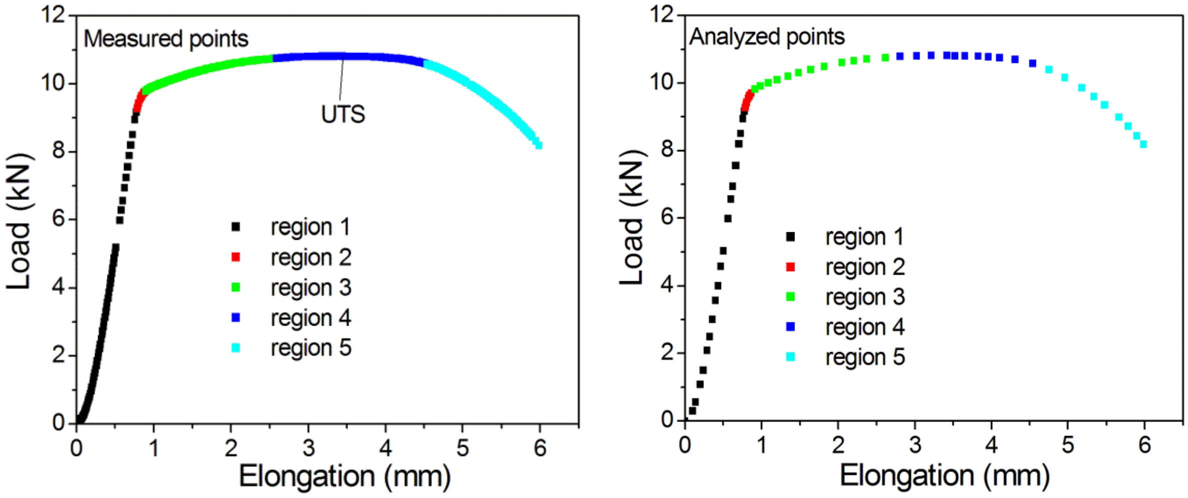

(a) (b)

Figure 3.6: Diffraction pattern measurement points: (a) measured points, (b) analyzed points for lattice strain evolution.

3.5 Pole figure measurement for texture gradient investigation

The as-received AA 7020-T6 block has a thickness of 29.7 mm, from which the texture-gradient sample was cut along the normal direction with dimensions of 7.09 × 6.36 × 29.7 mm^3. The investigated layers are described by the parameter $s = 2t/t_0$ (t is the distance from the center and t_0 is the plate thickness). Five layers were investigated, corresponding to the s values of 0.97, 0.73, 0.49, 0.26 and 0, respectively. Complete pole figure measurements were carried out at the high energy X-ray beamline HEMS P07B at PETRA III (DESY, Hamburg), with X-ray wavelength of 0.1422 Å, beam size of 0.5 × 0.5 mm^2, sample-detector distance of 1111 mm and mar345 detector, as shown in Fig. 3.7. The ω range for pole figure measurement was from -92.5° to 92.5° with 5° per step using continuous scanning mode. Complete orientation distribution function (ODF) was calculated from the measured (111), (200) and (220) pole figures by iterative series expansion method with an expansion degree of Lmax = 35 [46].

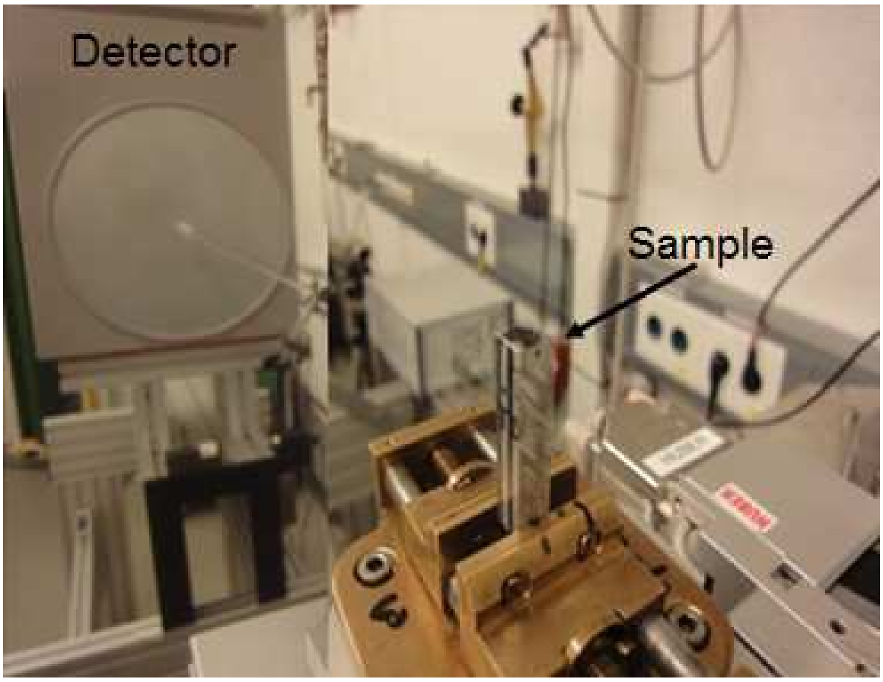

Figure 3.7: Complete pole figure measurement with Mar345 detector.

Due to the rolling process, the sample shows a texture gradient from the surface to the center of the as-received plate. Figure 3.8 shows the results of ODF analyses for different layers. Table 3.2 lists the main orientation components observed in Fig. 3.8.

In the surface layer (s = 0.97), the texture is consisted of the orientation components along the β fiber and weak shear components. The orientation components along the β fiber scatter towards the rotated cube component, i.e. the brass component scatters in the vertical direction in the φ_2 = 0° section, and the Copper component shifts to the Dillamore component which is at the lower Φ angle in the φ_2 = 45° section, and the S component also shifts the lower Φ angle in the φ_2 = 65° section. Besides, the rotated cube component scatters towards {112}<110> orientation which is located at {0°, 35°, 45°} in Euler space. In the subsurface layer (s = 0.73), rotated cube component becomes stronger, and the orientations along the β fiber get weaker than the surface layer. The scattering of the β fiber orientations also grow larger. In the quarter layer (s = 0.49), the orientations along the β fiber become stronger and shift back towards their ideal positions. The scattering of the Copper, brass and S components get smaller. The rotated cube component gets very weak. In addition, there is a weak Goss component. Further towards the center (s = 0.26 and s = 0), the texture is composed of the typical plain strain rolling texture, the orientations of which concentrate along the β fiber, and the shear components totally disappear.

Table 3.2: Miller indices and Euler angles of the main orientation components observed in the as-received AA 7020-T6 plate.

Designation	Miller indices	Euler angles		
	{hkl}<uvw>	φ_1/°	Φ/°	φ_2/°
Copper	{112}<111>	90	30	45
S	{123}<634>	59	34	65
brass	{011}<211>	35	45	0
Dillamore	{4 4 11}<11 11 8>	90	27	45
Goss	{011}<100>	0	45	0
Cube	{001}<100>	0	0	0
Rotated cube	{001}<110>	45	0	0
shear	{112}<110>	0	35	45

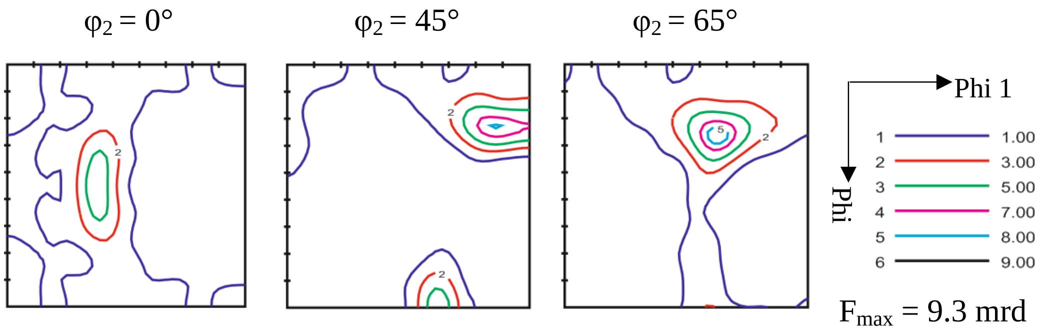

(a) s = 0.97

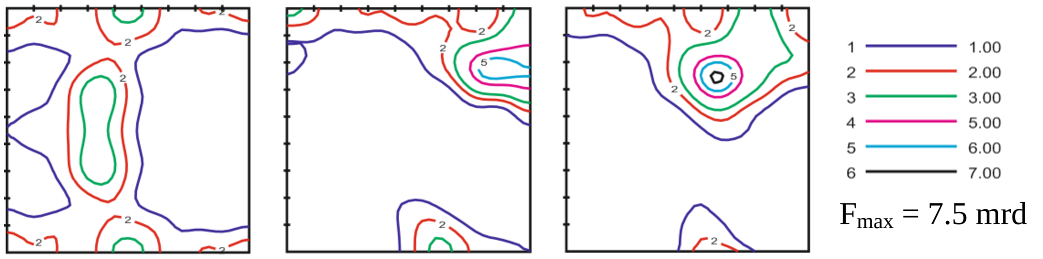

(b) s = 0.73

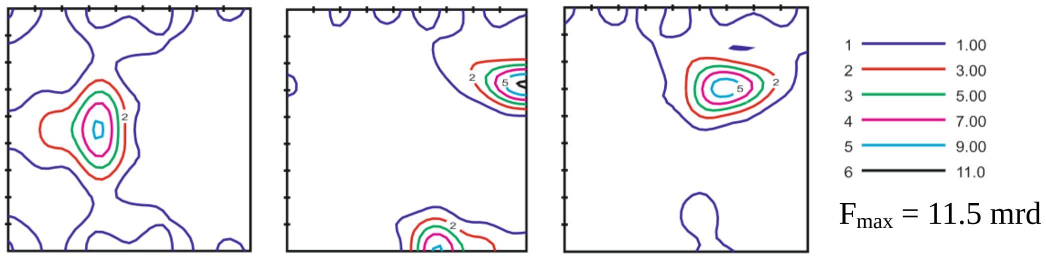

(c) s = 0.49

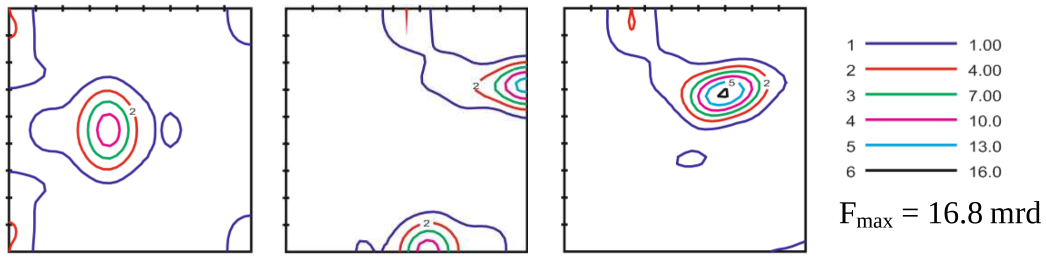

(d) s = 0.26

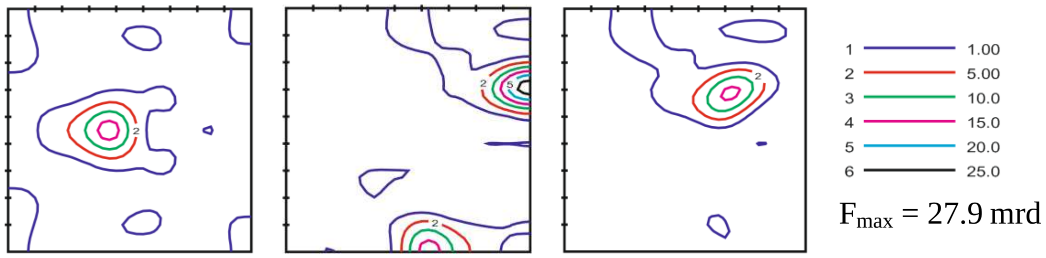

(e) s = 0

Figure 3.8: ODF analysis results of different layers of the as-received AA 7020-T6 plate.

3.6 In situ diffraction pattern measurements for flat tensile samples

The in situ tensile tests for the anisotropy investigation using flat tensile sample, were also carried out at HEMS P07B, with X-ray wavelength of 0.1420 Å, beam size of 0.5×0.5 mm^2, sample-detector distance of 1119 mm and Perkin Elmer XRD 1622 detector, on the universal tensile machine with loading speed of 5×10^{-4} mm/s till UTS at room temperature. In order to get lattice spacing d_{hkl} in both parallel and perpendicular to LD, the intensity-2θ spectra were integrated from the Debye-Scherrer rings within 10° sector in γ along the two directions. Lattice strains under different load were obtained by $\varepsilon = (d_{hkl} - d_{0,\,hkl}) / d_{0,\,hkl}$, where $d_{0,\,hkl}$ is the starting lattice spacing of stable elastic deformation. The misalignment of the area detector was calibrated by the LaB_6 standard powder using the software package FIT2D [95].

3.7 Metallographic Sample Preparation and Chemical Etching

The samples were firstly mounted in phenolic resin for metallographic preparation. After that, mounted samples were ground by silicon carbide paper 240, 400, 600, 800, 1000, 1200, 2400 at the speed of 150 rpm. Then, the samples were polished using micron diamond at the speed of 150 rpm for 15 minutes. The Struers model RotoPol-21 was used for grinding and polishing. The etching of the samples was carried out in the solution consisted of 200 ml distilled water and 5 g 35% tetrafluoroboric acid for 2 minutes under 30 V voltage. The optical microstructures were obtained by optical microscopy Olympus -PMG3.

4. Texture evolution during tension at RT: in situ measurement

4.1 Microstructure of the round tensile sample

The round tensile sample was cut from 7.5 mm below the surface of the as-received plate along RD, the microstructure of which is shown in Fig. 4.1. One can see that the grains are elongated along the RD. The average dimension of the grains along ND is around 40 μm.

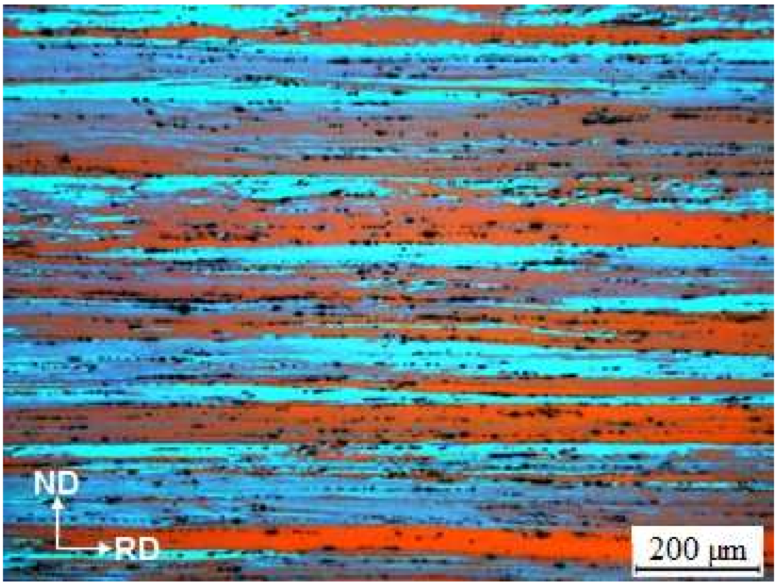

Figure 4.1: Microstructure of the ND-RD plane of the as-received material.

4.2 In situ texture measurements positions

The load-elongation curve for the texture evolution measurement is shown in Fig. 4.2. Six pole figure measurements were carried out, corresponding to the positions P1 (before load), P2 (after yield), P3 (half way between yield and UTS), P4 (UTS), P5 (shortly after UTS) and P6 (after failure). The load and elongations for each measured point are listed in Table 3.3. Furthermore, from Fig. 4.2 one can see that the stress released a little during each pole figure measurement.

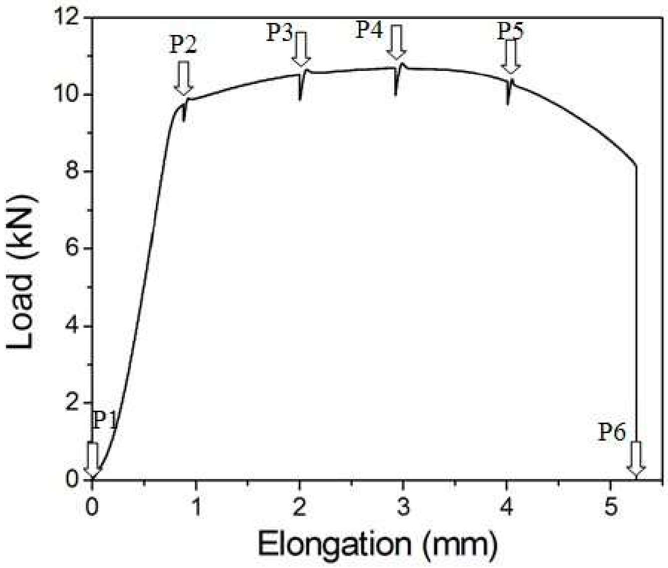

Figure 4.2: The load-elongation curve for the texture evolution measurement.

Table 4.1: The load and elongation for each pole figure measurement in Fig. 4.2.

	P1	P2	P3	P4	P5	P6
Load (kN)	0	9.75	10.52	10.68	10.33	0
Elongation (mm)	0	0.88	2.00	2.92	4.01	5.25

4.3 Results and discussion

4.3.1 Pole figure analysis

In order to see how the texture changes during tensile loading, the recalculated Al (111) pole figures of the sample under different loads are compared, as shown in Fig. 4.3.

In contrast with the initial pole figure (P1), the Al (111) pole figure after yield (P2) shows many changing details. Firstly, the pole densities at copper component positions decrease, especially for those near the center of the pole figure, which leads to the maximum pole density dropping down. Secondly, along the LD, the Dillamore component seems very clear due to the going down of the copper component, indicating Dillamore component is relatively stable at this stage. Thirdly, the pole densities of the component near the direction perpendicular to the LD, corresponding to the S component, also decrease. Fourthly, the pole densities of the four high-pole-density positions near the north and south of the pole figure also decrease a little, indicative of the decrease of brass and/or S components. From P2 to P3, details at the LD show that grains are rotating to the LD, making the pole density near LD higher and the two high-pole-density positions at the north and south of the pole figures, respectively, move closer to each other. It is observable that the pole densities near the center also start to increase. From P3 to P4, the high-pole-density positions at the north and south of the pole figures get further closer and the corresponding pole densities get higher. The maximum pole density close to the perpendicular to the LD moves outwards. From P4 to P5, the change is very small. From P5 to P6, the changes are more notable. Firstly, the maximum pole density increases. Secondly, the pole density near LD increases much, as can be seen from the color code. Thirdly, the pole densities at Copper, S and/or brass components increase. The maximum pole densities near perpendicular to the LD move outwards and reach the circumference.

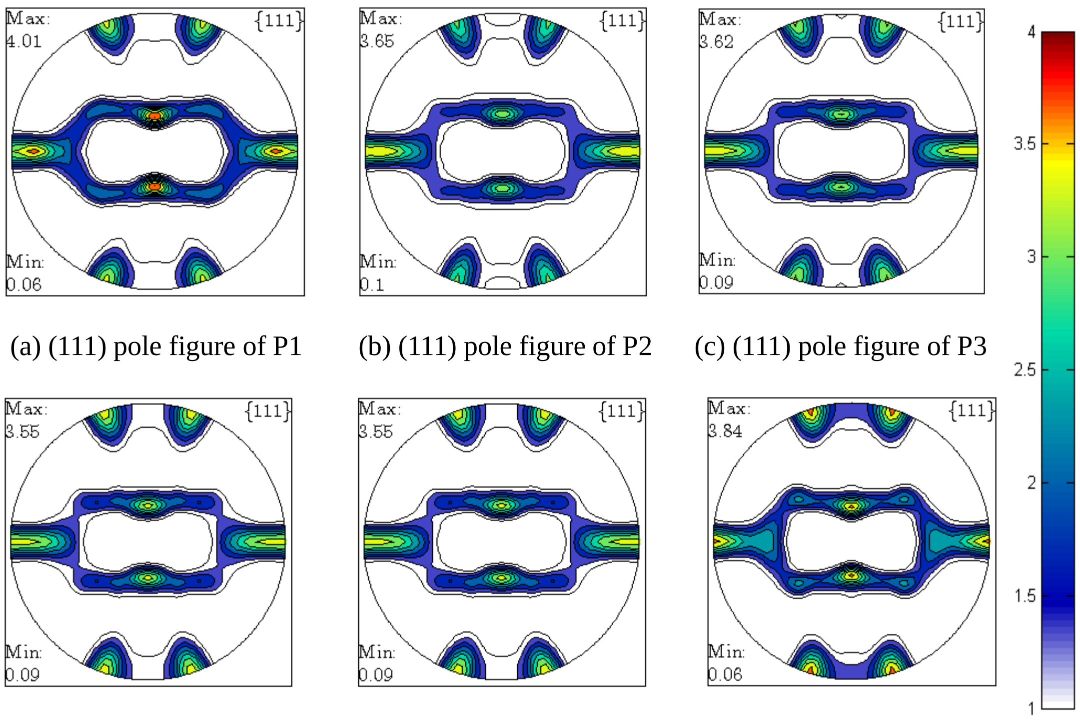

(a) (111) pole figure of P1 (b) (111) pole figure of P2 (c) (111) pole figure of P3

(d) (111) pole figure of P4 (e) (111) pole figure of P5 (f) (111) pole figure of P6

Figure 4.3: The recalculated Al (111) pole figures of the sample under different loads.

Table 4.2 shows the volume fractions of the different grains oriented with the normal of {111}, {200}, {220}, {311}, {331}, {420} and {422} parallel or perpendicular to LD at different loads during tensile loading. The volume fractions were calculated using the software MTEX [116-117].

Table 4.2: Volume fractions of grains oriented parallel and perpendicular to the LD.

Planes	{111}	{200}	{220}	{311}	{331}	{420}	{422}
	Volume fractions of the grains with plane normal parallel to LD (%)						
P1	0.073	0.032	0.054	0.303	0.121	0.074	0.423
P2	0.059	0.034	0.067	0.269	0.149	0.082	0.386
P3	0.067	0.034	0.053	0.276	0.139	0.072	0.401
P4	0.072	0.035	0.046	0.276	0.133	0.065	0.423
P5	0.074	0.036	0.043	0.273	0.131	0.061	0.428
P6	0.086	0.041	0.044	0.263	0.129	0.062	0.421
	Volume fractions of the grains with plane normal perpendicular to LD (%)						
P1	0.147	0.022	0.116	0.121	0.196	0.147	0.191
P2	0.153	0.016	0.111	0.109	0.212	0.156	0.173
P3	0.151	0.016	0.107	0.109	0.220	0.152	0.176
P4	0.150	0.016	0.107	0.107	0.225	0.149	0.173
P5	0.152	0.016	0.109	0.106	0.226	0.149	0.168
P6	0.151	0.028	0.138	0.119	0.223	0.136	0.158

Parallel to LD, four groups of grains can be summarized. The first group includes {111} and {422} grains, the volume fractions of which first go down after yield, and then increase gradually in the following process. The second group contains {200} grains whose volume fraction increases during all the process. The third group contains {331} and {420}, and the volume fractions of them first increase after yield, but after that they decreases gradually. {220} and {311} grains belong the forth group. The volume fraction change of this group has a tendency to decrease. The volume fractions of {111} and {200} grains increase monotonously after yield, indicating the plastic deformation tends to form {111} and {200} fiber textures at the early stage of tensile loading.

Perpendicular to LD, volume fraction changes are more complicated. The volume fractions of {200}, {220} and {311} grains first go down, and then go up. The volume fraction of {331} grains has a generally tendency of increase, whereas that of {422} has a tendency of decrease. The volume fraction of {420} first increases after yield, but it decreases gradually after that. The volume fraction of {111} grains fluctuates around a certain value. The complicity can be attributed to the grains constituting the reflections. For instance, the grains with the normal of {200} planes orientate to the direction perpendicular to the LD, meanwhile may have the normal of {hk0} or {h00} planes orientate to the LD.

4.3.2 ODF analysis

Tensile of both Al single crystal and polycrystals makes a specific crystallographic direction rotate to the LD. The specific crystallographic direction is defined as stable end orientation. The stable end orientation of tension of Al single crystal is <112>, while for Al polycrystals <111> is the stable end orientation for high degree deformation. Investigation in [118] shows that when the LD is parallel to RD, the LD is located close to the [-111], which is the stable end orientation during uniaxial tension. Therefore, grains need not rotate much to reach the stable end orientation. When LD is parallel to 90° to RD, firstly, the LD will rotate to the [-112], and then it will rotate to the [-111]. When LD is parallel to 45° to RD, the rotation path of LD cannot be determined by the low index ideal orientations, even though the grains show trend to rotate their [-111] towards the LD after 135% elongation [118].

It is worth noting that the above mentioned grain rotation behavior was observed after large tensile deformation. In the present study, grain rotation behavior was investigated at small tensile deformation using in situ synchrotron X-ray diffraction.

Figure 4.4 and 4.5 show the ODF analysis results of the sample under different loads. From them, one can see that the brass component increases gradually during the whole tensile test, and it also shows a trend to scatter in the vertical direction. In φ_2 = 45° section, for the initial texture, the ideal components are superimposed by Dillamore and Copper components. But as the tensile test continues, the local maximum orientation density near these two components shifts towards lower φ_1 angle till close to fracture where the local maximum orientation density shifts back to higher φ_1 angle. From Fig. 4.5, one can see that the orientation density of copper component drops down quickly from initial state to after yield. Then it stays stable up to the measured point P5. After that, the orientation density of copper component increases again. The orientation density of S component, firstly, decreases a little from initial state to after yield. Then it increases gradually from after yield to UTS. After that, it decreases gradually from UTS to after fracture.

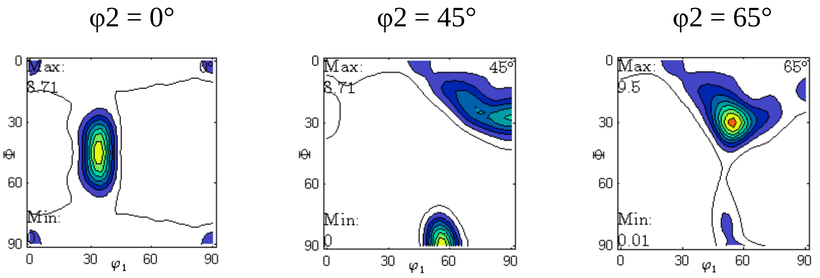

(a) P1 (initial state)

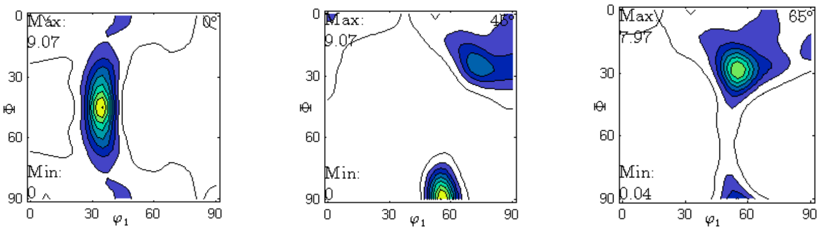

(b) P2 (after yield)

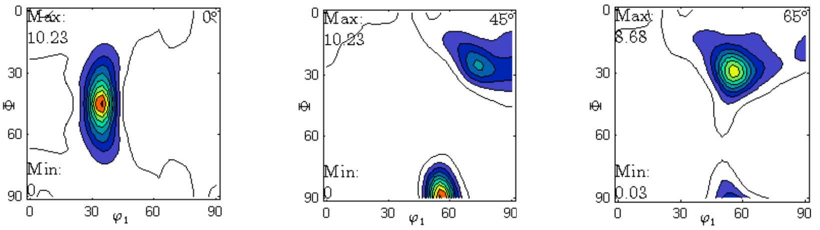

(c) P3 (between yield strength and UTS)

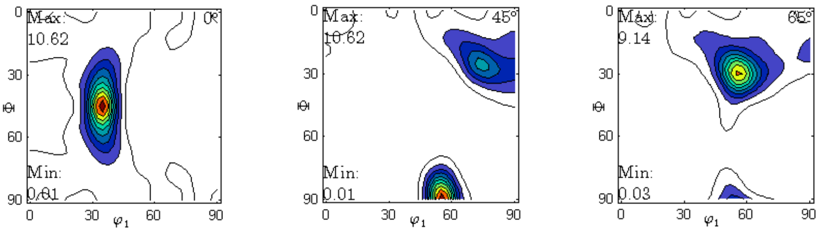

(d) P4 (at UTS)

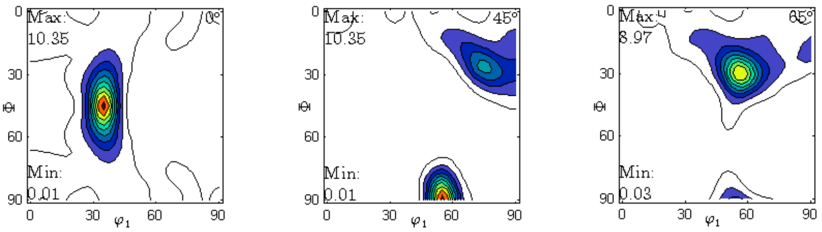

(e) P5 (between UTS and fracture)

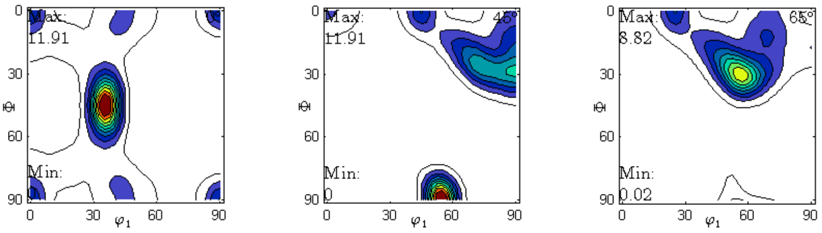

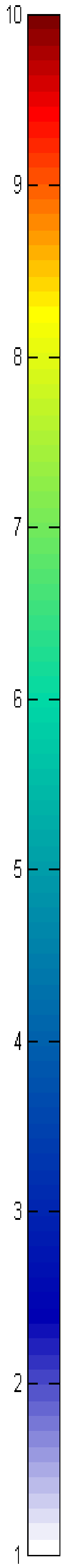

(f) P6 (after fracture)

Figure 4.4: ODF analysis results for the sample during tensile test.

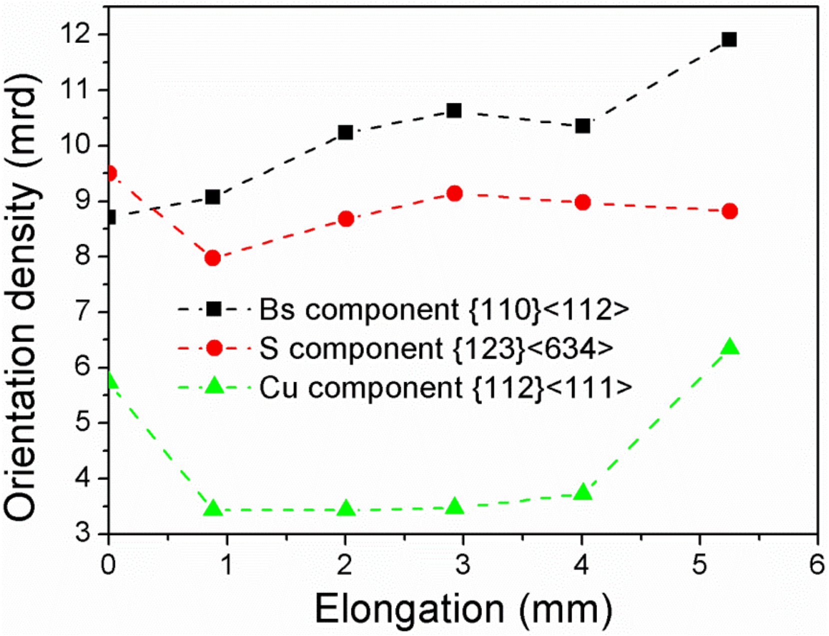

Figure 4.5: The orientation density changing trend of ideal components.

The initial texture shows that the orientations concentrate along β fiber with a weak cube component. However, the Dillamore component is more pronounced than the copper component, indicating that there was shear deformation during rolling at the layer where the sample was cut from the as-received block. Also the shear influences can be clearly seen from Fig. 4.4 (a) in $\varphi_2 = 0°$ section where the brass component scatters along the vertical direction (along Φ angle direction).

After yield, evident phenomena are that the orientation of copper component and S component decreases a lot, the rotated cube component increase a little. The reason can be attributed to the initial texture. When the shear component exists in the sample, the copper component is not stable [119]. Therefore, the orientation density of copper component decreases a lot after yield. The shear component also makes the maximum orientation density near the copper and Dillamore components shift towards lower φ_1 angle. But the brass component is relatively stable compared to the copper and S components and the orientation density of brass component increases a little in this stage, indicating the grains tend to rotate towards <112> direction at this stage.

From after yield to fracture, the volume fraction of grains with {111} and {100} plane normal parallel to the LD increases monotonously, as shown in Table 4.2, indicating the grains tend to rotate their <111> and <100> to the LD. Figure 4.6 shows the simulation results of lattice rotation from 3 to 5% tensile deformation by self-consistent model, Taylor model and Sachs model, respectively. All the three models show the general trend that the LD tends to rotate towards either <111> or <100>, which is in agreement with the experimental results from after yield to fracture.

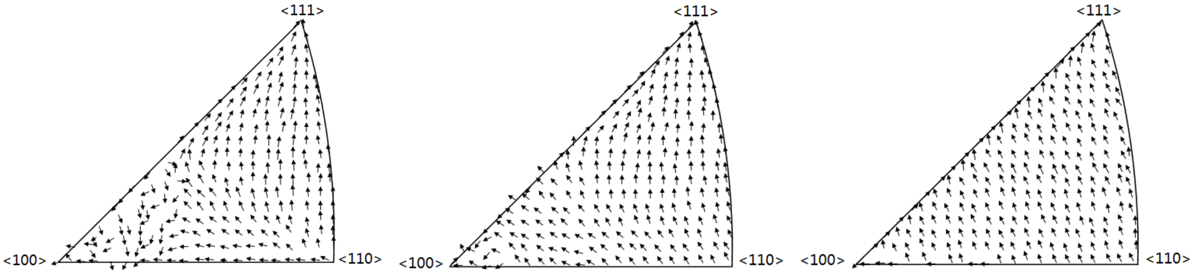

(a) Self-consistent model (b) Taylor model (c) Sachs model

Figure 4.6: Lattice rotations from 3 to 5% tensile deformation [86].

4.4 Summary of the texture evolution

Texture evolution of the sample from 7.5 mm below the surface of the as-received AA 7020 plate, the axis of which was parallel to the RD, was investigated in this chapter. The initial texture exhibits copper type texture with sharpness around 10 mrd and a weak cube component. The Dillamore component is more pronounced than the copper component. The texture evolution shows that the main orientations remain concentrated on copper type texture during tensile test due to the small deformation from initial state to sample fracture. The brass component shows an increasing trend during the whole test. From yield to fracture, the volume fraction of grains with <111> and <100> parallel to the LD increases monotonously, indicating some grains tend to align their <111> and <100> to the LD. However, due to the small deformation, one cannot see the formation of {111} and {100} fibers directly from the pole figures.

5. Lattice strain evolution during tension at RT: in situ measurement

From the diffraction pattern measurements, the lattice strain of the lattice plane oriented in a specific direction can be determined through the changes of lattice spacing at different loads, thereby giving information of how the differently oriented grains behave under uniaxial tension. In the present study, the lattice strains of the lattice planes with their normal oriented parallel to and perpendicular to the LD, which satisfy the Bragg’s law with respect to the incident beam, are determined. Figure 5.1 (a) and (b) show the lattice strain evolution during uniaxial tension in parallel to and perpendicular to the LD, respectively. One can see from the figure that the reflex-dependent lattice strain evolution varies from plane to plane, indicating different mechanical behavior of the differently oriented grains. The curve is divided into 5 regions according to the lattice strain evolution in the LD. In the region 1 (elastic region), the lattice strain of each reflex increases linearly as the elongation increases. In the region 2 (elastic plastic region), the lattice strain of each reflex starts to deviate from linearity, indicating grains start to yield. In the region 3, the lattice strain of each reflex exhibits increasing tread, indicating the work hardening of the each lattice plane, even though the {222} lattice planes show a relatively small hardening and the {311} lattice planes show no work hardening at the beginning of this region. In the region 4, the lattice strains of some reflexes start to decrease while those of the others still increase. In the region 5, the lattice strains of all lattice planes decrease as the elongation increases.

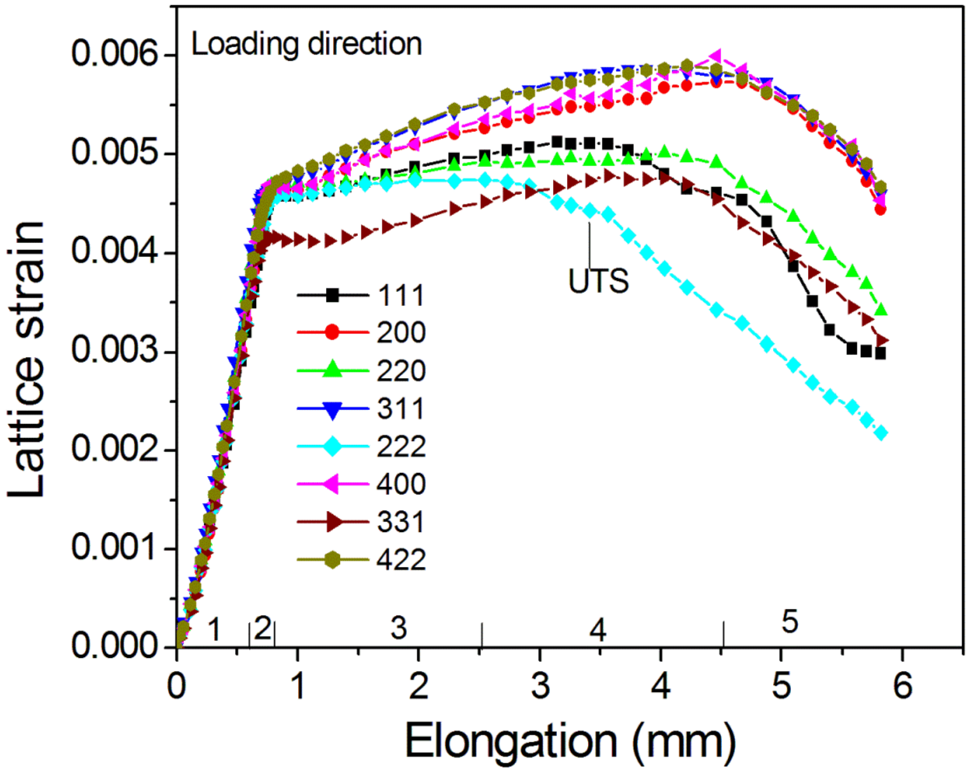

(a) Parallel to LD

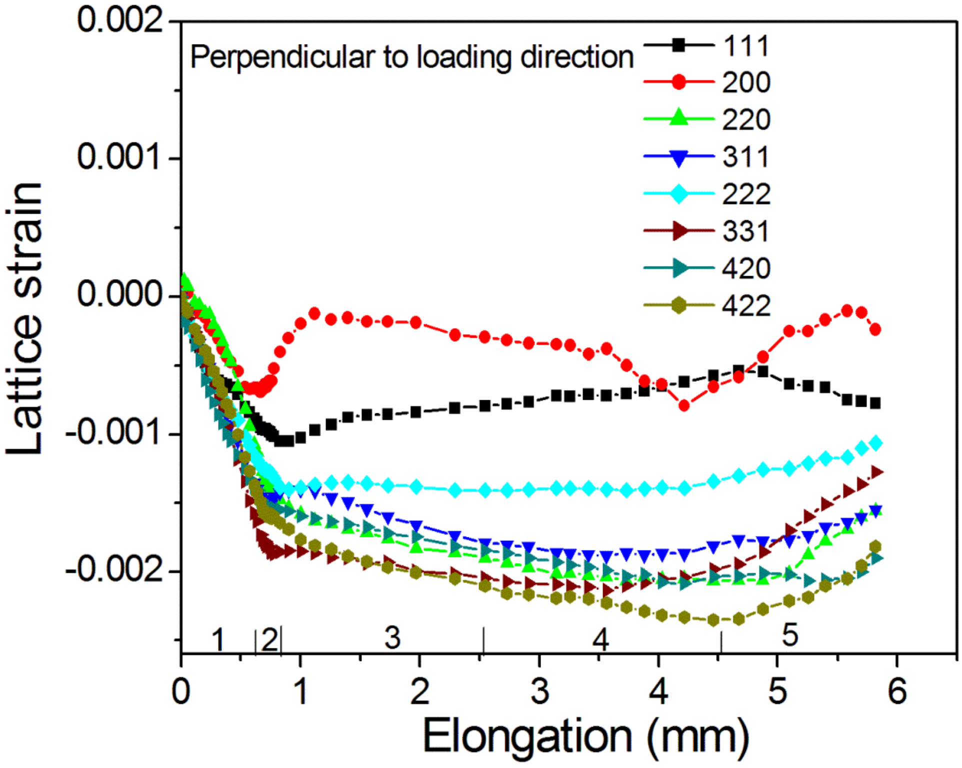

(b) Perpendicular to LD

Figure 5.1: Lattice strain evolution during uniaxial tension.

5.1 Lattice dependent Young's Modulus and Poisson's ratio

When a polycrystalline material deformed in elastic region, external stress is partitioned among the constituent grains in an inhomogeneous way, which can be attributed to the elastic anisotropy of the material and the interactions among the neighboring grains [89]. The elastic anisotropy is dependent on the single crystal properties, and has the expression of $2C_{44}/(C_{11} - C_{12})$. For aluminum, C_{11} = 108.2 GPa, C_{12} = 61.3 GPa and C_{44} = 28.5 GPa [120]. Therefore, the elastic anisotropic value of aluminum equals 1.22, indicating the elastic anisotropy is small. The interactions among neighboring grains depend mainly on the orientation correlations between neighboring grains and the amount of the differently oriented grains in a specific direction, i.e. the texture of the material.

Figure 5.2 shows the measured diffraction pattern points in elastic region. From it, one can see that the beginning of the curve is not linear due to the movements between the sample and the clamp of the tensile machine. Therefore, the measured points in the linear part are used to calculate the Young's modulus and Poisson's ratio, as illustrated in the Fig. 5.2. There are two measured points missing in the range of elongation of 0.5 to 0.6 mm due to a mistake during the measurement, but it does not hinder the analysis of the Young's modulus.

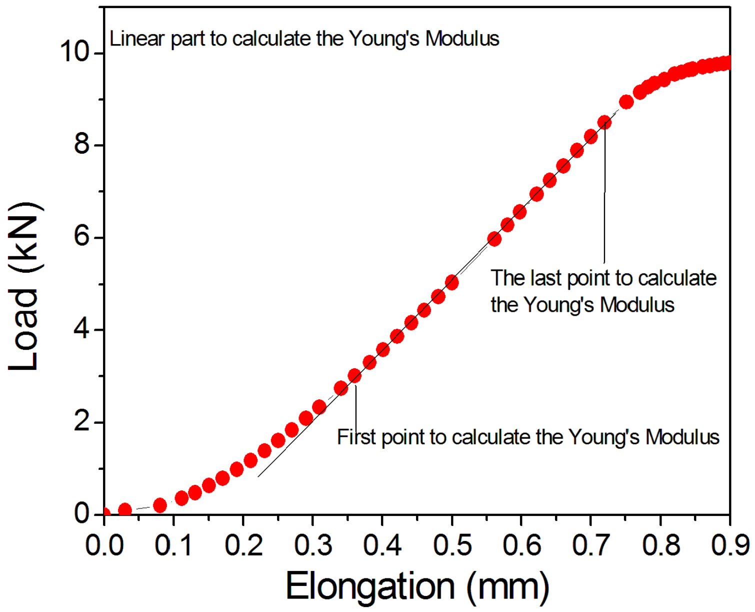

Figure 5.2: Linear part of the load elongation curve in elastic region and the measured points.

In order to get lattice spacing d_{hkl} in both parallel to and perpendicular to the LD, the intensity *vs.* 2θ spectra were integrated from the 10° sectors along the two directions, respectively, as shown in Fig. 2.27. The lattice strains under different loads were obtained by $\varepsilon = (d_{hkl} - d_{0,hkl})/d_{0,hkl}$, where $d_{0,hkl}$ is the starting lattice spacing of {hkl} lattice planes at stable elastic deformation. The misalignment of detector was calibrated by Zn powder.

Figure 5.3 shows the lattice strain evolution in both parallel to and perpendicular to LD in elastic region, taking the {111} and {311} planes as examples. The Young's modulus of different lattice plane can be obtained by

$$E_{hkl} = \Delta\sigma / \Delta\varepsilon_{//}^{hkl} \qquad \text{(Eq. 5-1)}$$

where $\Delta\sigma$ is the stress increment and $\Delta\varepsilon_{//}^{hkl}$ is the lattice strain increment of {hkl} lattice planes in the LD. Therefore, the E_{hkl} equals the slope of the linear fitting of the applied stress *vs.* lattice strain curve along the LD. The Poisson's ratio of different lattice plane can be obtained by

$$\nu_{hkl} = -(\Delta\sigma / \Delta\varepsilon_{//}^{hkl}) / (\Delta\sigma / \Delta\varepsilon_{\perp}^{hkl}) = -\Delta\varepsilon_{\perp}^{hkl} / \Delta\varepsilon_{//}^{hkl} \qquad \text{(Eq. 5-2)}$$

where $\Delta\varepsilon_{\perp}^{hkl}$ is the lattice strain increment of {hkl} lattice planes in perpendicular to LD. Thus, ν_{hkl} equals the slope of the linear fitting of the applied stress *vs.* lattice strain in the LD divided by that in the perpendicular to LD. Table 5.1 lists the Young's modulus and Poisson's ratio determined from the measured data together with the Young's modulus calculated from the Kröner model (E_k) for aluminum with random orientation.

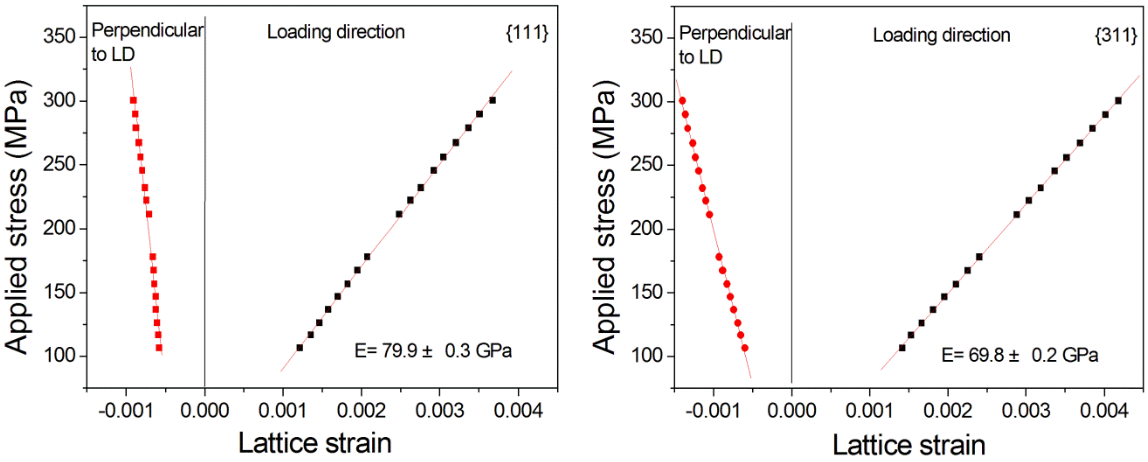

(a) {111} planes

(b) {311} planes

Figure 5.3: Example of lattice strain evolution in elastic region.

Table 5.1: Measured and calculated (Kröner model) Young's modulus and Poisson's ratio.

lattice planes	111	200	220	311	222	331	422
E/GPa	79.9±0.3	73.5±0.3	71.8±0.3	69.8±0.2	76.4±0.3	73.9±0.4	76.6±0.5
ν	0.138	0.173	0.349	0.284	0.218	0.388	0.338
E_k/GPa	72.3	66.7	70.8	69.2	72.3	71.2	71.8
ν_k	0.346	0.358	0.349	0.352	0.346	0.348	0.349

As can be seen from Table 5.1, the Young's moduli of different lattice planes determined by measurement are different from those calculated from the Kröner model. The possible reasons for the differences can be attributed to the following: crystallographic texture, alloying elements and grain morphology. Crystallographic texture decides the orientation correlations among neighboring grains, thereby influencing the distribution of external load to different lattice planes so that some lattice planes may undergo more stress than other lattice planes, which leads to larger lattice strains for these lattice planes. Besides, the interactions among the neighboring grains affect the lattice strains of individual lattice planes, especially for the textured materials [121]. However, the {311} lattice planes are less influenced by the current texture. Two reasons may contribute to this. The first one is that the amount of {311} lattice planes along the LD is relatively more than some other lattice planes, as shown in Table 4.2. The second one is that the multiplicity factor of {311} is 24. Texture has much less influence on the lattice planes with high multiplicity factor.

5.2 Lattice strain in the region 2

From Fig. 5.2, the macro yield strength of the sample was obtained to be 309.1 MPa, which is consistent with the values of Al 7020 alloy reported in [122-123]. The yield strengths of different lattice planes are shown in Table 5.2. From the table, one can see that the yield strengths of individual lattice planes are lower than the macro yield strength. The possible reason may be that the macro yield strength is the average value of all lattice planes oriented in all directions. The measured lattice planes account for a very small portion of all lattice planes, as shown in Table 4.2. There may be some lattice planes which cannot be measured by the area detector (reflexes at bigger two theta angles) or which are oriented in some other directions with respect to the LD, having higher yield strengths.

Table 5.2: The yield strengths of different lattice planes.

Lattice planes	111	200	220	311	222	331	422
Yield strength/MPa	294.6	290.7	302.1	309.1	296.7	295.8	294.3

The lattice strains of different lattice planes in yield region are shown in Fig. 5.4. The changes in lattice strain result from the load redistribution among different oriented grains. The load redistribution is determined by both elastic and plastic anisotropy. In the LD, the lattice strain of {331} lattice planes has the lowest lattice strain value when it yields. At the same time, other planes still deform elastically. It means {331} lattice planes experience lower load when the sample yields. The other lattice planes undergo higher load.

In the perpendicular to LD, the {200} lattice planes has the lowest lattice strain when the sample yields, whereas the {331} lattice planes have the highest lattice strain, which is on the contrary of the lattice strain in the LD. The lattice strain changing trend in the perpendicular to LD is smoother than that in the LD, because the deformation in the perpendicular to LD is mainly controlled by the Poisson contraction. The Poisson’s ratio can be seen from Table 5.1, and it shows that the Poisson’s ratio of {331} is the highest one, which makes the {331} lattice planes have the largest lattice strain in the perpendicular to LD.

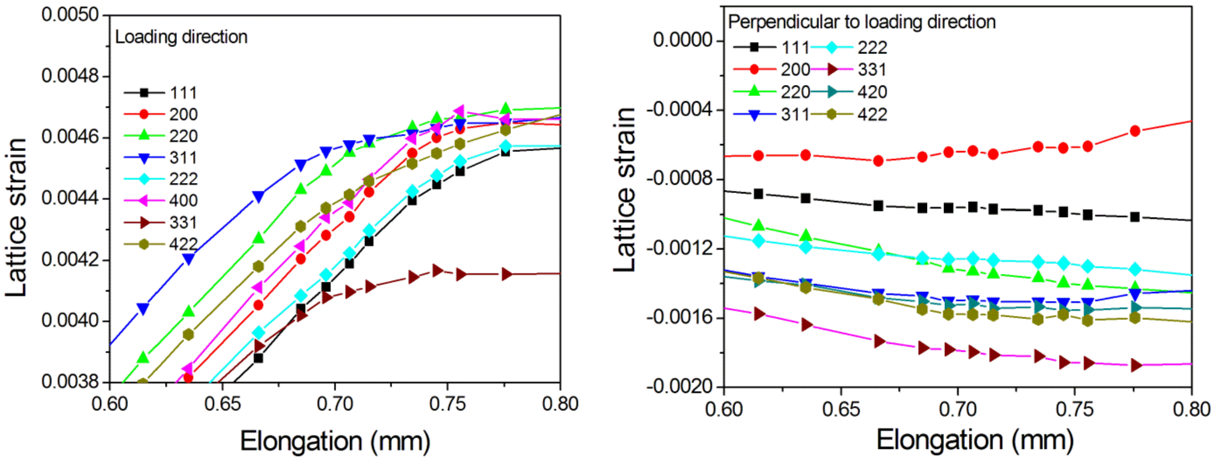

(a) Parallel to LD

(b) Perpendicular to LD

Figure 5.4: Lattice strain evolution in the region 2.

5.3 Lattice strain evolution in region 3

The lattice strain evolution form after yield to half way to the UTS, i.e. elongation from 0.8 mm to 2.6 mm, which corresponds to the green points in Fig. 3.6, is shown in Fig. 5.5. Parallel to the LD, work hardening can be seen from all the lattice planes, even though the {222} lattice planes shows very small work hardening and the {311} lattice planes do not get harder at the beginning of this region. The lattice strains increasing rate of {311}, {422}, {200} and {400} planes show bigger values than those of {111}, {220} and {222} planes. The working hardening behavior of different lattice planes depend on the dislocation slip. Different combinations of slip systems can cause various work hardening behaviors, which will be discussed in the section 5.6.

Perpendicular to LD, the lattice strain is mainly controlled by the Poisson contraction and interaction among the neighboring grains. The {200} planes show a dramatic difference from others. They experience a tensile stress after yield. The reason for this will be discussed in chapter 7. Except {200} planes, the {111} lattice planes undergo less compressive stress than the other planes, because the Poisson's ratio of {111} lattice planes is smaller than those of other lattice planes', as shown in Table 5.1. The lattice strains of {111} and {222} are different, because they are not from the same group of grains. Details will be discussed in section 5.6.

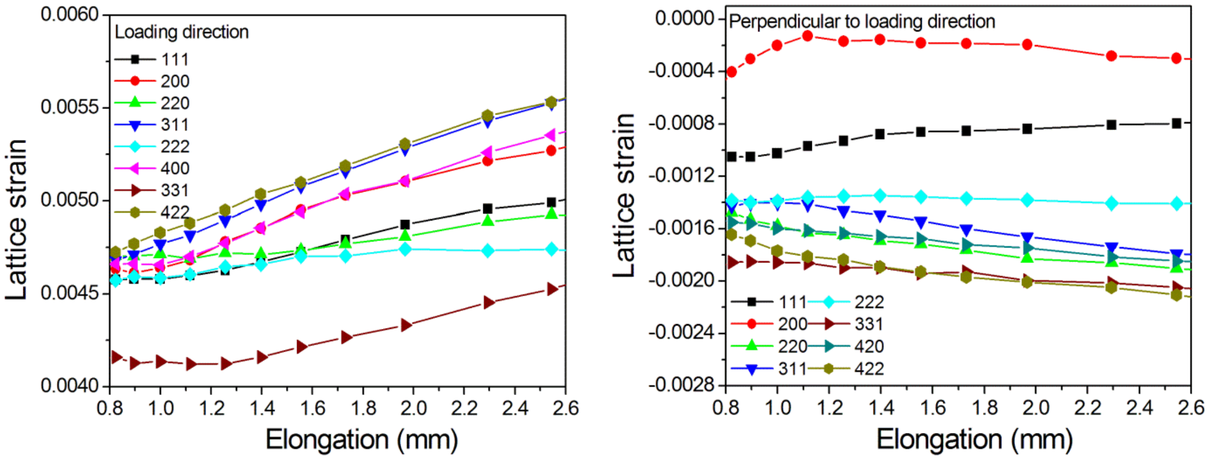

(a) Parallel to LD

(b) Perpendicular to LD

Figure 5.5: Lattice strain evolution in the region 3.

5.4 lattice strain evolution in region 4

The lattice strain evolution in region 4 is shown in Fig. 5.6, corresponding to the blue points in Fig. 3.6. In the LD, after UTS, the lattice strains of {200}, {400}, {311}, {331} and {422} continues to increase, indicating that these lattice planes reach their own ultimate tensile stresses after the sample’s UTS. The lattice strain of {222} starts to decrease at the beginning of this region, whereas the lattice strain of {111} starts to decrease around UTS. The lattice strain of {220} shows a decreasing trend at the end of this region. Before that, it keeps relatively stable. Perpendicular to LD, the lattice strains of some lattice planes show different changing trend as those in the LD, indicating again that the Poisson contraction is not the only factor which controls the grain behavior, and the interactions among neighboring grains have effects on the grain behavior.

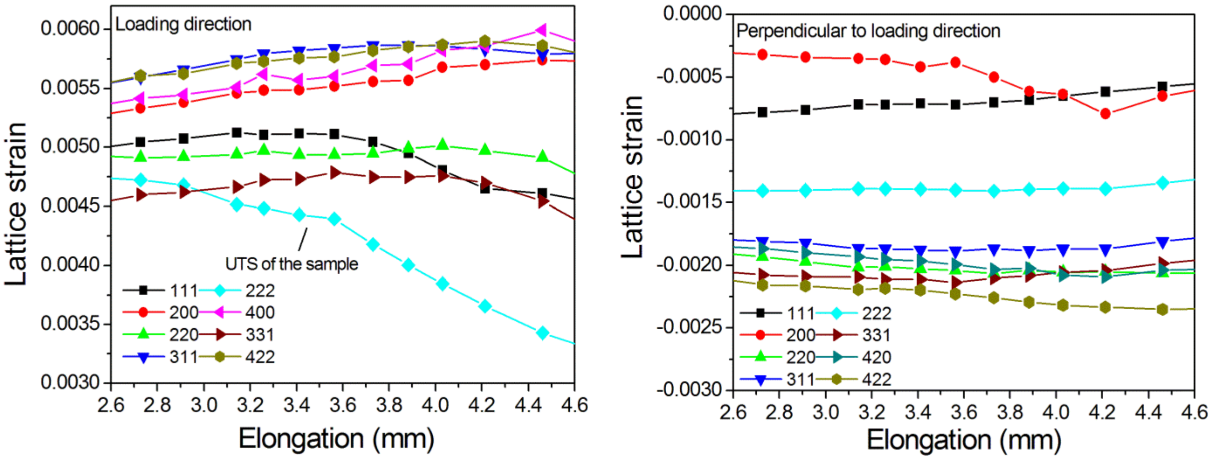

(a) Parallel to LD

(b) Perpendicular to LD

Figure 5.6: Lattice strain evolution in the region 4.

5.5 lattice strain evolution in region 5

The lattice strain evolution in region 5 is shown in Fig. 5.7, corresponding to the light blue points in Fig. 3.6. Along the LD, the lattice strains of all lattice planes decrease as the elongation increases, which indicates that all the lattice planes undergo a relatively compressive stress resulted from the reversal of the elastic deformation. The measured area is not the necking area, but close to the necking area. Therefore, when the necking starts, the reversal of elastic deformation exerts a relatively compressive stress to the measured area. Perpendicular to LD, except the {111} and {200}, the lattice strains (absolute value) of all the other lattice planes show a decreasing trend.

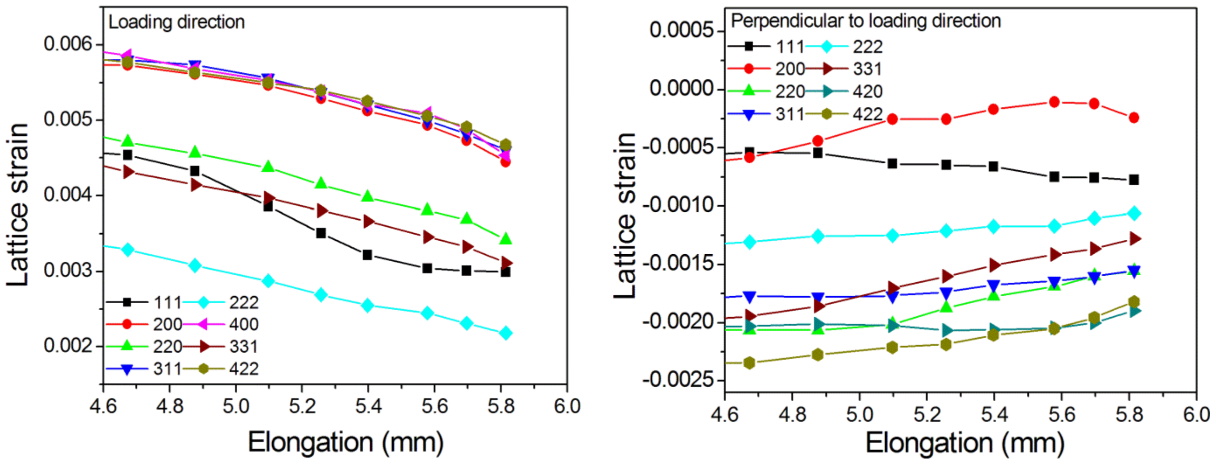

(a) Parallel to LD

(b) Perpendicular to LD

Figure 5.7: Lattice strain evolution in the region 5.

5.6 Discussion

The profile of diffraction peak changes when the deformation is exerted upon the measured area. Three main differences can be obtained, including peak shift, peak broadening and peak height change, as shown in Fig. 5.8. Peak shift is related to the change in the lattice plane spacing, which is attributed to the type I stress (macroscopic stress) and type II stress (intergranular stress). Peak broadening is mainly related to the defects density generated by plastic deformation. Peak height is mainly associated with the orientation changes of grains. The lattice strain discussed in this chapter is due to the peak shift.

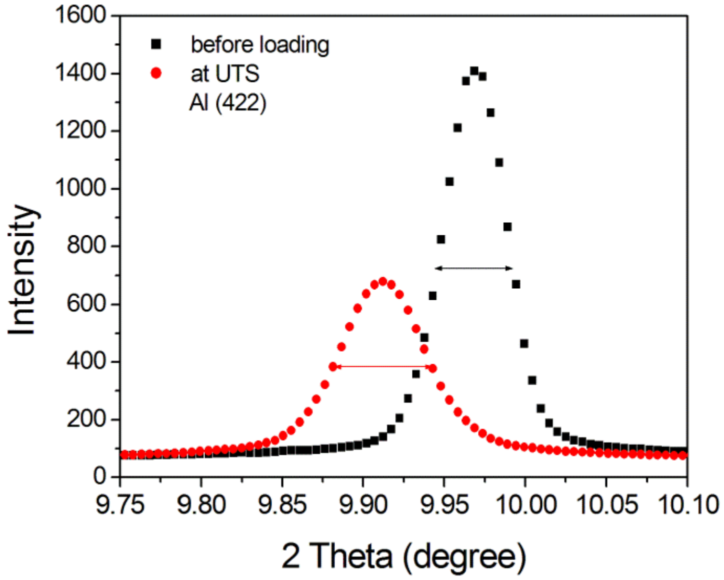

Figure 5.8: Peak comparison between unloaded state and at UTS.

For polycrystalline materials, the interaction among the neighboring grains plays an important role in the response of a grain to external load [124], especially when the texture is present in the material. Thus, the stress-strain response of specially oriented grains depends largely on the neighboring grains. In elastic region the measured Young’s moduli of different lattice planes are different from the calculated values by the Kröner model which assumes neighboring environment of a grain is homogeneous and has random orientations. In Knöner model, the {111} planes are stiffest while the {200} planes are the most compliant. However, texture changes the mounts of grains with special orientation in a specific direction. It exerts influences on the load distributions among different lattice planes oriented in the specific direction, making the measured Young’s modulus deviate from the theory. For example, in Table 5.1, the measured Young’s modulus of {200} planes is not the most compliant one. It can be attributed to the neighboring grains which surround the grains containing the {200} planes with plane normal parallel to the LD. The neighboring grains confine the deformation of the {200} grains, making the lattice strain of {200} planes smaller than when there is no confinement. Therefore, the Young’s modulus of {200} grains is larger than that of the theoretically calculated one.

The Young modulus difference between the {111} and {222} lattice planes can be attributed to the different diffraction 2θ angles. The 2θ angles are 3.48° and 6.97° for the {111} and {222} planes, respectively, under the experimental condition. It means that the normal of the measured {111} and {222} planes are 1.74° and 3.49° away from the LD, respectively, which makes the neighboring grains are different for the {111} and {222} planes. Thus, the interactions among neighboring grains of the two group planes are different, leading to the different measured lattice strains.

When plastic deformation starts, the lattice strains of lattice planes largely depend on the texture, because it exerts geometrical restrictions on the dislocation slip process. It is necessary to summarize which slip systems are activated for a given orientation. In fcc metals with high stacking fault energy, the slip systems are {111}<110>, totally 12 slip systems, as shown in Table 2.1. For a single fcc crystal, how many slip systems are equally stressed depends on along which crystallographic direction the crystal is stressed. If the loading axis is parallel to <111>, <100> and <110> directions, there are 6, 8, 4 equally stressed slip systems, respectively. If the loading axis is parallel to a direction lying on a boundary of the basic triangle, for example <311> direction, there are two equally stressed slip systems. If the loading axis is parallel to a direction inside the basic triangle, there is only one slip system which is favored [125-126]. The <111> orientation of polycrystalline aluminum has high work hardening rate, whereas the <100> orientation and the orientations with only one slip system work harden very slowly. The differences between the <111> orientation and <100> orientation are very evident, even though they have 6 and 8 equally stressed slip systems, respectively. Therefore, the number of equally stressed slip system cannot explain the different work hardening behavior. Special combination of slip systems must play an important role in the different work hardening behavior.

Bishop pointed out that there are four different crystallographic stress states that can activate polyslip [127]. Kocks divided the four types of stress states into five types when he investigated on the work hardening behavior of different stress states [125]. Polyslip by the so called [111] tension stress state has high work hardening rate, whereas polyslip by the so called [100] tension stress state shows very low work hardening rate, as shown in Fig. 5.9. Polyslip by the other three stress states, respectively, show work hardening between the [111] tension stress state and [100] tension stress state. Figure 5.10 shows the polyslip activated by the [111] tension stress state and [100] tension stress state.

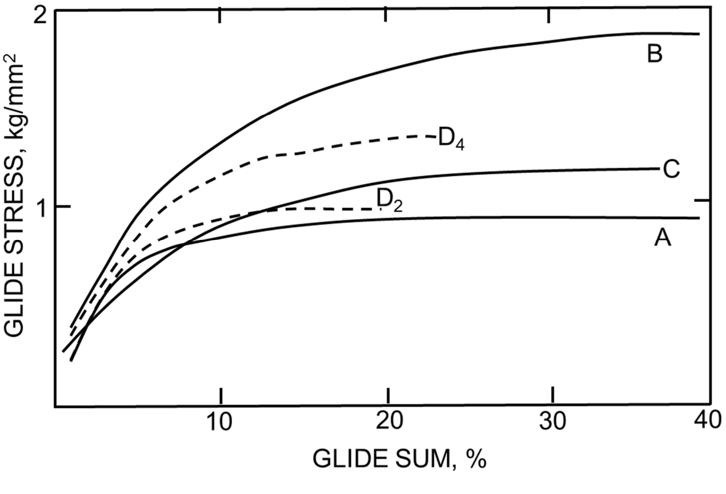

Figure 5.9: Work hardening behavior of different stress states. A is [100] tension. B is [111] tension. Details can be found in [125].

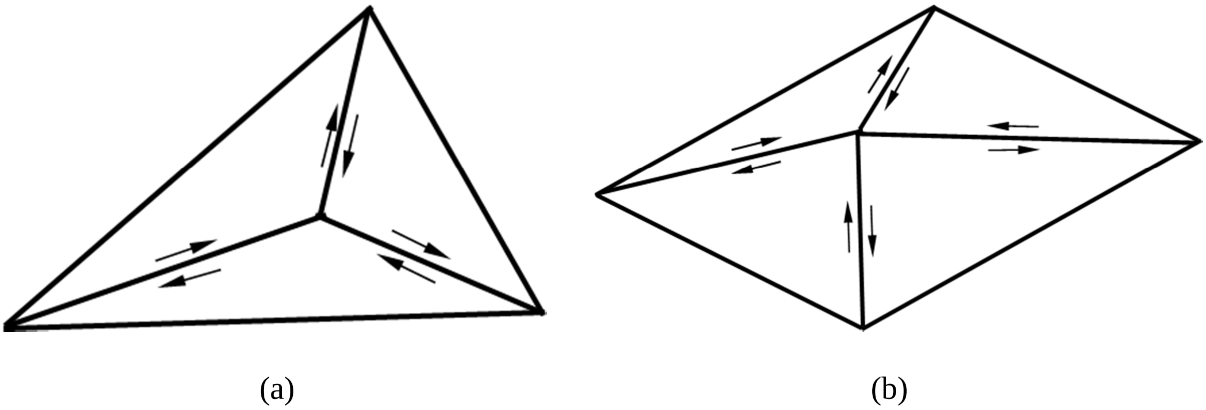
(a) (b)

Figure 5.10: Polyslip activated by (a) [111] stress state; (b) [100] stress state [125].

In the present study, the interactions among different oriented grains are very pronounced due to the preferred orientations in this sample, which may change the stress state in specific oriented grains. It is a big challenge to measure the stress states which cause the different work hardening behavior of individual lattice planes, but it is feasible to estimate which stress state is more dominant in specific oriented grains. For the lattice planes which show very high work hardening rate such as {311} and {422} in Fig. 5.5, the [111] tension stress state is dominate. For the lattice planes which show almost no work hardening such as {222}, the [100] stress state controls the lattice strain.

In the region 4, the lattice strains of {111} and {222} lattice planes decrease while the lattice strains of other lattice planes still shows an increasing trend, indicating the load release starts firstly in the {111} and {222} lattice planes. The ultimate tensile strength of {222} appears before the sample's UTS, but the ultimate tensile strengths of {200}, {400}, {311}, {331} and {422} appear after the sample's UTS. The UTS of the sample is the average value of all lattice planes when the average value reaches its maximum. From the beginning of region 5, lattice strains of all lattice planes decrease as the elongation increases due to the reversal of the elastic deformation. The reversal of the elastic deformation has much influence on the dislocation density in the sample, which will be discussed in chapter 6.

5.7 Summery of the lattice strain evolution

This chapter investigated the lattice strain evolution of a sample having copper type texture with maximum orientation density around 10 mrd. The tensile test was conducted till sample fracture. In the elastic region, the {111} lattice planes are the stiffest, as in theory, but the {200} lattice planes are not the most compliant ones due to the interactions with neighboring grains having other orientations. The Young's modulus of {311} lattice planes is less affected by the texture with 10 mrd sharpness, which is almost the same as that of the {311} calculated by Kröner model for randomly oriented polycrystalline aluminum. In the plastic region, the work hardening behavior is mainly controlled by the two types of dislocation arrangements, the so called [111] tension stress state and [100] tension stress state. Load release firstly starts on the {111} and {222} lattice planes before UTS. The ultimate strengths of some lattice planes appear before sample's UTS while those of other lattice planes appear after sample's UTS. The UTS of the sample is the average value of all lattice planes when the average value reaches its maximum.

6. Dislocation density evolution during tension at RT: in situ measurement

As mentioned in section 2.11, X-ray diffraction peaks get broader due to reduced crystallite size and/or increased defect density. The crystallite size should be smaller than around 1 μm, while the dislocation density needs to be larger than 5×10^{12} m^{-2}.[98], being able to be detected by X-ray diffraction, depending on the instrument. In addition, instrument based line broadening [128] and line broadening by sample thickness [129] (transmission method) will make an extra broadening of the diffraction peaks. Therefore, line broadening from these two parts should be deconvoluted before making peak broadening analysis, from which one can get the information of defect density and/or crystallite size.

6.1 Calibration of the misalignment of the detector

The misalignment of the detector was calibrated by stress and texture free Zn powder with 10 μm grain size using the software Fit2d. Firstly, the diffraction pattern of the Zn powder is input to the Fit2d. Secondly, one chooses the calibration option in the software. Thirdly, one input an ASCII file containing the lattice spacing values of the {hkl} lattice planes of which the whole Debye-Scherrer rings are collected by the area detector. The Debye-Scherrer rings chosen for the calibration should be the ones which are not overlapped by different {hkl} lattice planes. Fourthly, the software calculates the beam center position, the tilting angle of detector (in plane) and the rotation angle of the tilting plane based on the chosen Debye-Scherrer rings. The tilting angle of detector in our case is 0.1978°. Fig. 6.1 shows the diffraction pattern of the Zn powder and the 2θ-γ-intensity plot of the diffraction pattern after calibration. The γ is the azimuth angle along the Debye-Scherrer ring. From Fig. 6.1 (b), one can see that the misalignment of the detector is well calibrated.

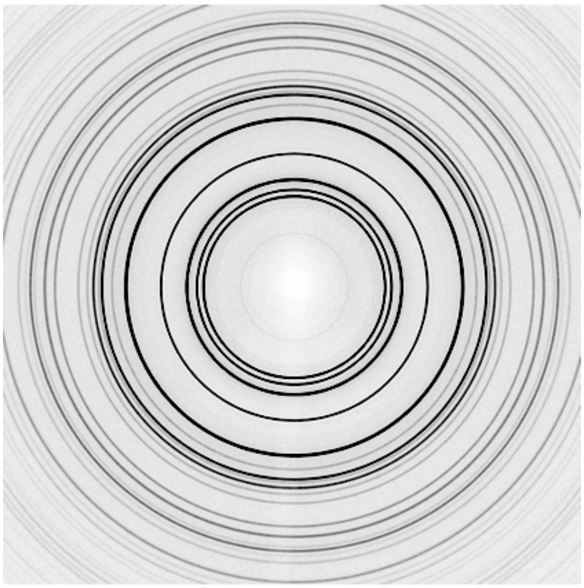

(a)

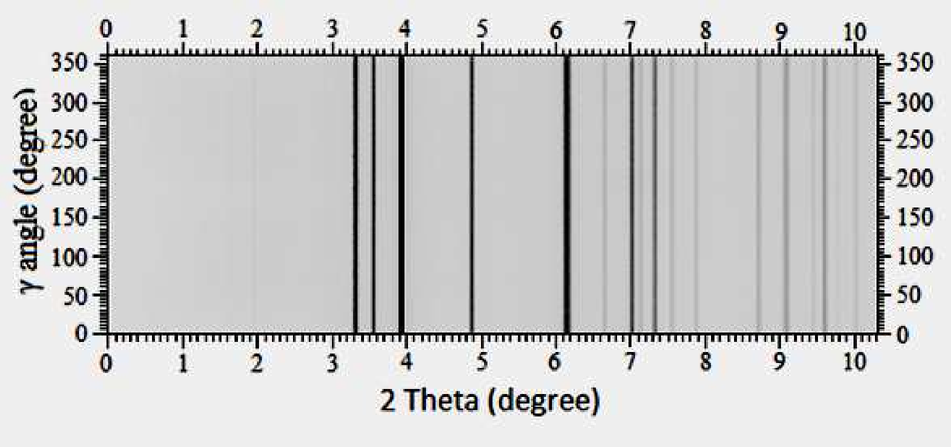

(b)

Fig. 6.1: (a) Diffraction pattern of Zn powder; (b) the 2θ-γ-intensity plot of the diffraction pattern of Zn powder after calibration.

6.2 Thickness correction

All the diffraction pattern measurements were carried out by transmission method, i.e. the high energy X-rays penetrated the sample thickness. Thus, it should make thickness correction before performing peak broadening analysis. Figure 6.2 shows the sketch of how the thickness of a sample contributes to the peak broadening.

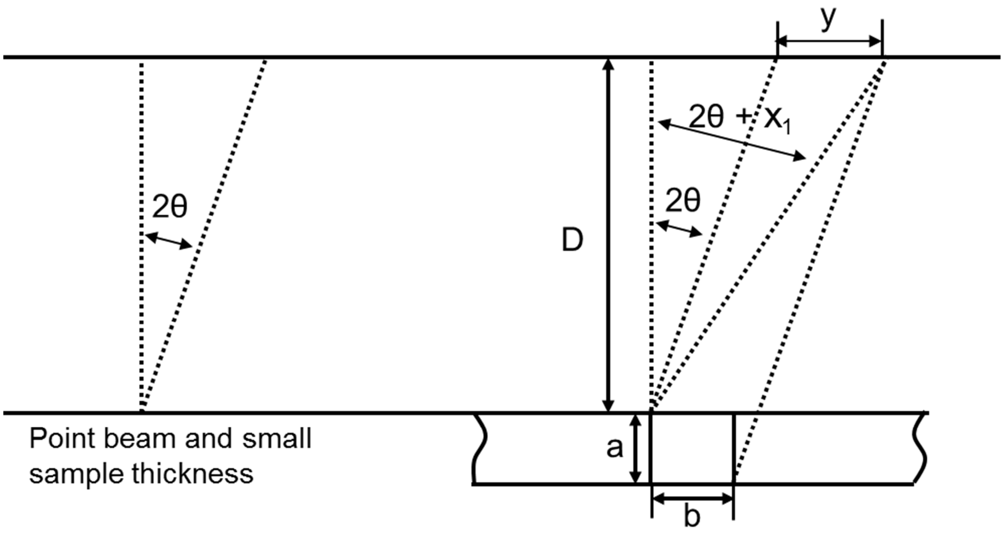

Figure 6.2: Sketch of the thickness effect on peak broadening.

The meanings of the symbols used in Fig. 6.2 are as follows: a: sample thickness; b: side length of the beam size; θ: diffraction angle; x_1: the delta 2 theta angle which is broadened by a and b; y: the length on the area detector caused by both a and b, y = b + a*tan2θ; D: sample-detector distance.

According to geometry relations among the above mentioned parameters, the following equation can be obtained:

$$x_1 = \arctan\left(\mathrm{b}/\mathrm{D} + \mathrm{a}/\mathrm{D}\tan 2\theta + \tan 2\theta\right) - 2\theta \qquad \text{(Eq. 6-1)}$$

Equation 6-1 contains the beam size effect on peak broadening, which will be also counted in the instrumental broadening in the following part. This part of peak broadening should be removed form thickness effect. Assuming the thickness of the sample to be 0 mm, the contribution form the beam size, x_2, at a given 2θ angle has the following expression:

$$x_2 = \arctan\left(\mathrm{b}/\mathrm{D} + \tan 2\theta\right) - 2\theta \qquad \text{(Eq. 6-2)}$$

Assuring the intensity distribution of the thickness effect and beam size effect, respectively, are Gauss distribution. Then using Gaussian deconvolution, the broadening effect from only the thickness effect, x, has the following expression:

$$x = \left(x_1^{\ 2} - x_2^{\ 2}\right)^{\frac{1}{2}} \qquad \text{(Eq. 6-3)}$$

Notice the x is the broadened 2θ on the area detector before integration. It should be converted to the broadened FWHM at a given 2θ. According to the definition of Gauss distribution, the standard deviation σ approximately equals x/6. So the broadened FWHM by the thickness effect, FWHM_1, has the expression:

$$\text{FWHM}_1 = 2\sqrt{2\ln 2} * (x/6) \qquad \text{(Eq. 6-4)}$$

6.3 Instrumental correction

Instrumental broadening is caused by the divergence of the beam, beam size, slits systems and all that related to the instrument. It should also be removed to get the physical broadening by lattice defects and/or small coherently scattering domain size. In the present study, the NIST Al_2O_3 plate is used as the standard sample to get the instrumental function, and the thickness of it is 1.5 mm. Furthermore, the measured instrumental function should also be corrected by thickness effect (removing the broadening caused by thickness). Figure 6.3 shows the measured instrumental function (IF) curve and the IF curve corrected by thickness effect using the calculation procedures mentioned in section 6.2. The correction is carried out in way of Gaussian deconvolution. In addition, the FWHM caused by thickness effect at each diffraction peak of Al_2O_3 plate are indicated by the green points. One can see that the thickness effect on peak broadening increases with the increasing 2 theta almost in a linear way.

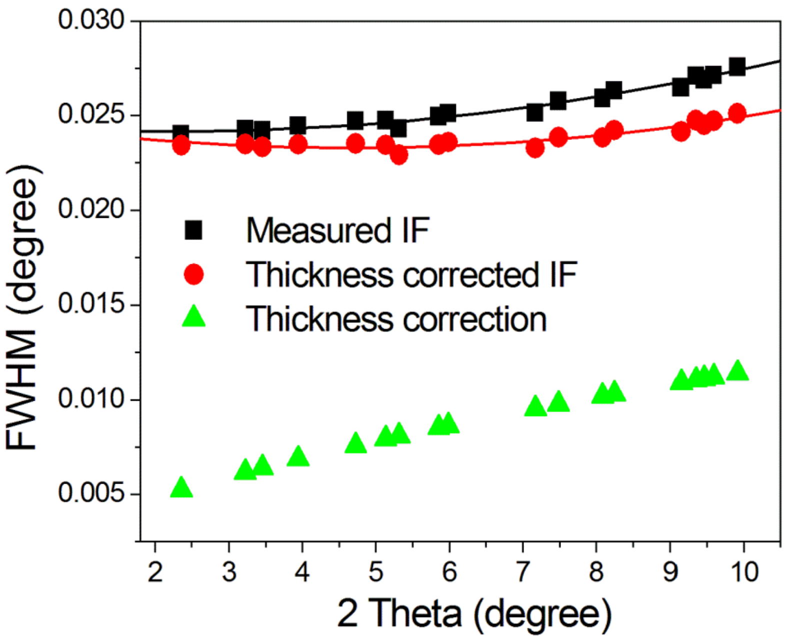

Figure 6.3: The measured and the thickness corrected instrumental functions and thickness correction values for the diffraction peaks of NIST standard Al_2O_3 plate.

6.4 FWHM changing trend during tension

The FWHM evolution of the Al (111), (200), (220), (311), (331), and (422) peaks are shown in Fig. 6.4 as a function of elongation during tensile loading. In the elastic region, with the exception of Al (220) and (422) peaks, the FWHM of all the other planes decreases as the elongation increases. From yield on, the FWHM of all peaks increases rapidly, indicating a rapid generation of defects and/or reduction of crystallite size, corresponding to the strain broadening and/or size broadening, respectively. However, at the end of region 3 and the beginning of the region 4, as the elongation increases, the increasing rate of FWHM slows gradually down. Around UTS, the FWHM of all peaks keep almost constant, except the Al (111) and (311). Close to the end of the region 4, the FWHM of Al (111) and (311) decrease a little. At the end of region 5, the FWHM of Al (331) and (422) show an increasing trend, whereas that of Al (111) shows a decreasing trend.

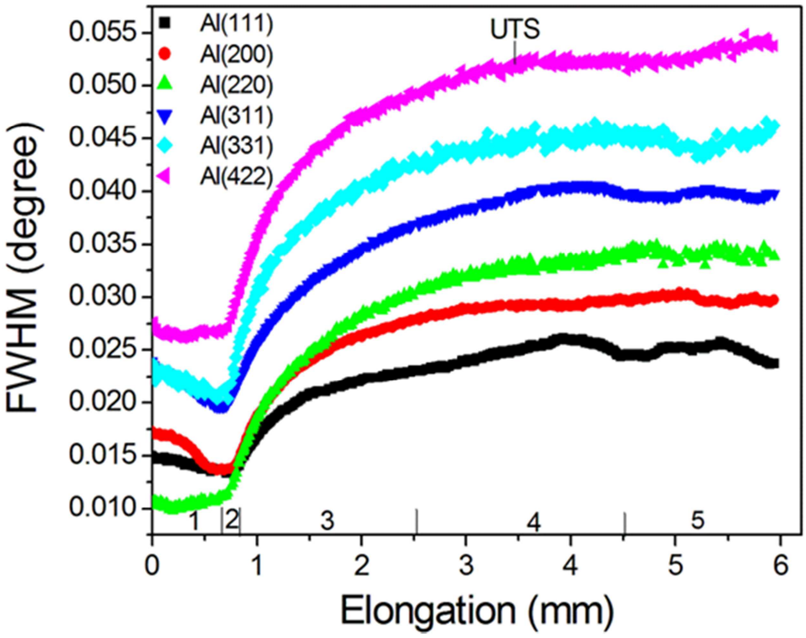

Figure 6.4: FWHM development during tension.

6.5 Peak broadening analysis

In the present study, the thickness correction in section 6.2 can be applied due to 3 factors. First, the beam size is 0.5 × 0.5 mm^2. Second, the scattering angle is very small, maximal 2 theta angle being around 10.4°. Third, the diameter of the sample is 6 mm. Therefore, the irradiated part of the sample can be assumed as a flat sample.

Figure 6.5 shows the conventional Williamson-Hall plot of the thickness and instrument corrected FWHM at unloaded state and at UTS. From it, the Williamson-Hall anisotropy can be observed [130]. The sample before load shows a strong strain anisotropy, but it becomes less anisotropic at UTS. As a matter of fact, the strain anisotropy of the sample does not change until yielding. According to the three categories of lattice defects defined by Krivoglaz [104], the linear type of defects majorly contribute to strain broadening. On the basis of this, after yielding, the change of strain anisotropy should be due to the increase of dislocations.

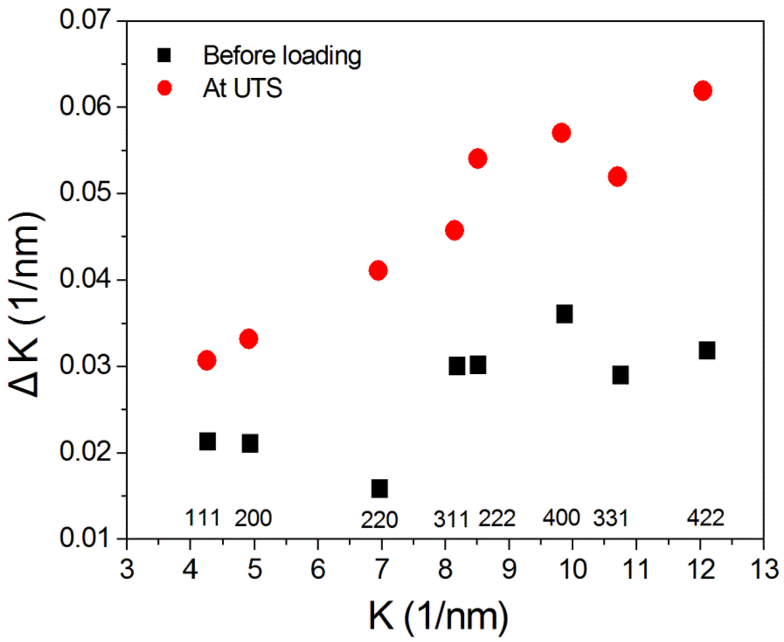

Figure 6.5: Conventional Williamson-Hall plot for the sample before loading and at UTS.

Modified Williamson-Hall plot is used to evaluate dislocation density evolution during tensile loading. As can be seen in the section 2.11, the dislocation arrangement parameter M cannot be obtained by Williamson-Hall procedure. It can only be got from the tail of the peak profile through some assumptions [131-132]. Therefore, the accurate value of dislocation density cannot be obtained from modified Williamson-Hall plot. However, it does not hinder the evaluation of dislocation density evolution for a series of spectra obtained during tensile loading. The present study fixes M = 2, a value between high strain and low strain of an Al alloy got from [133]. Figure 6.6 shows the modified Williamson-Hall plot for the sample before loading and at UTS, respectively. In modified Williamson-Hall plot, the $\overline{C}_{h00}$ is calculated on the assumption that half edge and half screw dislocations exist inside the sample using the program ANIZC [134]. $\overline{C}_{h00} = 0.1922$, with elastic constants of Aluminum, C_{11} = 108.2 GPa, C_{12} = 61.3 GPa, C_{44} = 28.5 GPa [120]. The slope of the linear regression fitting is used to calculate the dislocation density using Eq. 2-36.

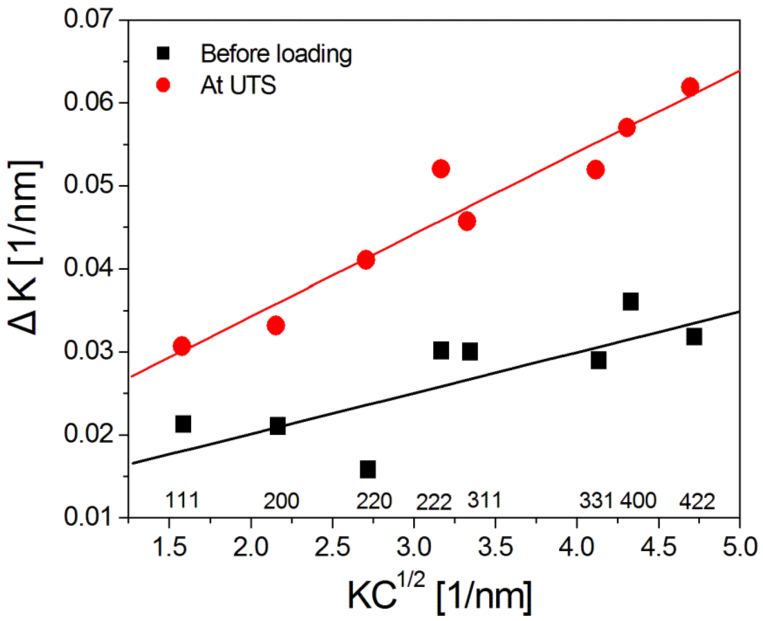

Figure 6.6: Modified Williamson-Hall plot for the sample before loading and at UTS.

6.6 Dislocation evolution during tensile loading

The dislocation evolution during tensile loading is shown in Fig. 6.7. The initial dislocation density is 6.26×10^{13} m^{-2}, which is close to the dislocation density of an aluminum sample after annealing.

In the region 1, dislocation density decreases gradually as the applied stress increases. In this region, the applied stress is not high enough to make generation of dislocations, but it can make the existing dislocations mobile. Thus, when the dislocation line segments of the same character but opposite polarity (positive or negative) encounter, they annihilate each other, leading to the decrease of dislocation densities.

When it reaches the region 2 (yield area) and region 3, the resolved shear stress is high enough to initiate dislocation slip. New dislocations are continuously generated by sources such as Frank-Read source. Also expansion of the dislocations increases the line length within the volume. The two factors make the whole dislocation density go up. Due to the relatively low dislocation density at the initial state, the annihilation of dislocations is low. Therefore, dislocation density increases with high rate till around 2.56 mm elongation. The lattice strain evolution of all the lattice planes in Fig. 5.1 (a) also shows that all lattice planes exhibit work hardening in region 3.

In the region 4, as the applied stress increases, the annihilation of dislocations becomes stronger and stronger so that the increasing rate of dislocation density gets smaller and smaller. From elongation around 2.56 to around 4 mm, a balance between the generation and annihilation of dislocations is reached. In this area, the {111} and {222} lattice planes start to soften, while the other lattice planes still harden, as shown in Fig. 5.1 (a). At the end of the region 4，there is another dominant dislocation generation. It may be due to the decrease of the applied stress after UTS, which is like a relatively compressive stress that changes the balance between dislocation generation and annihilation and makes the former larger. The relatively compressive stress makes the lattice strain of {111}, {220}, {222} and {422} decrease, but has no effect on the other lattice planes, as shown in Fig. 5.1 (a).

In the region 5, at first, dislocation density starts to decrease. Two factors may contribute to this. One is that the dislocation density induced by the relatively compressive stress reaches its maximum, leading to dislocation annihilation reaching a high value. The other one is the applied stress drops down close to the yield stress, resulting in a lower dislocation generation. In the last section of region 5, the sudden increase of dislocation density can be attributed to the reversal of the elastic deformation, which exerts a relatively compressive stress to the measured area (close to the necking area). In the measured area, the reversal of the elastic deformation is faster than that at the beginning of the region 5, as shown by the lattice strain evolution in Fig. 5.1 (a), which makes dislocation generation dominant again.

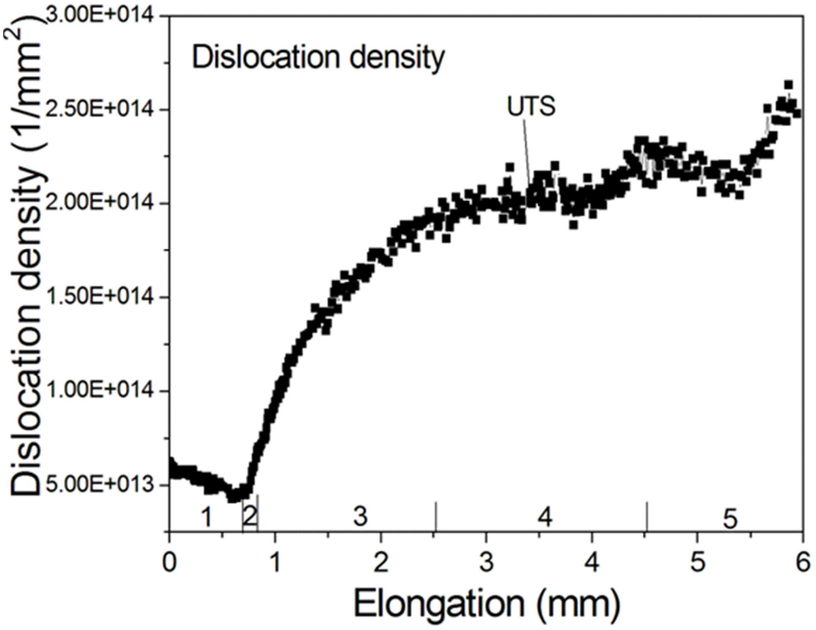

Figure 6.7: Dislocation density evolution during tensile loading.

6.7 Dislocation density and flow stress

According to dislocation theory, the correlation between dislocation density and flow stress can be expressed by Taylor equation [135]:

$$\sigma = \sigma_0 + \overline{M}\alpha\mu b\sqrt{\rho} \qquad \text{(Eq. 6-5)}$$

where σ_0 is the friction stress, $\overline{M}$ is average Taylor factor, α is a constant, μ is the shear modulus, b is the Burgers vector and ρ is the dislocation density. Figure 6.8 shows the stress against square root of dislocation density plot. A good linear correlation is found between these two parameters in the elongation range from 0.83 mm to 2.56 mm. In this range, dislocation generation is dominant, as mentioned in section 6.6. In the later elongation range, when the annihilation of dislocation becomes balanced with dislocation generation, Eq. 6-5 is not suitable to describe the correlation between the stress and square root of dislocation density. Moreover, as shown in chapter 4, the texture does not change much due to the small deformation of the tensile test. Therefore, the average Taylor factor should not change much in the elongation range from 0.83 to 2.56 mm. In the present study, it is assumed to be constant in this range. Making linear fitting of the measured data by least square regression and taking average Taylor factor $\overline{M}$ = 3.06, μ = 26 GPa, b = 0.286 nm, one can get α = 0.296, which is in the range of 0.2-0.35 [136-137], indicating the good correlation between the experimental data and calculated dislocation density.

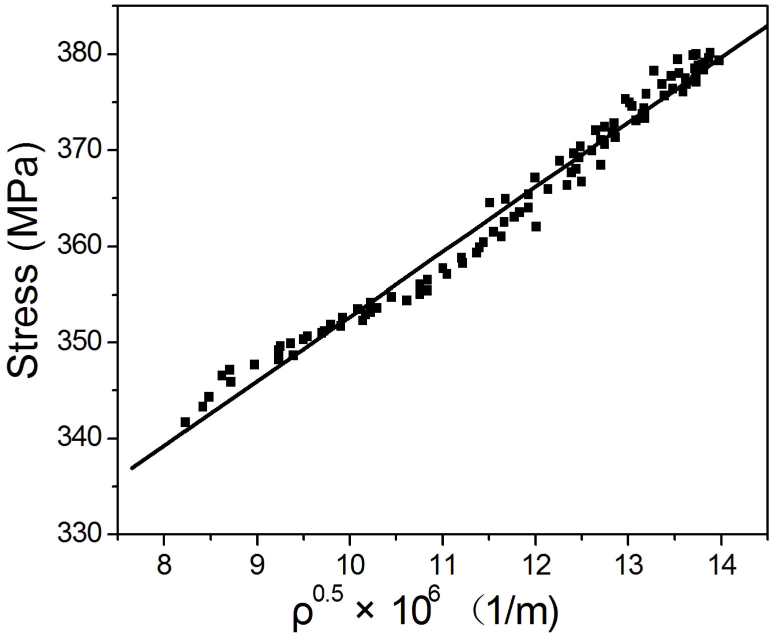

Figure 6.8: Applied stress vs. square root dislocation density plot.

6.8 Summery of dislocation density evolution

Peak broadening analysis is carried out using modified Williamson-Hall plot, assuming the micro strain is caused solely by dislocations. It is feasible to characterize the evolution of dislocation density along the loading axis during uniaxial tension of an AA 7020-T6 sample. Also a method for correction of the peak broadening caused by sample thickness is developed and has been successfully used for data evaluation. Results show that in the elastic region, dislocation density decreases as the elongation increases. From yield to half way between yield and UTS, the dislocation density increases rapidly, which contributes to the work hardening of individual lattice planes mentioned in chapter 5. Near UTS, the dislocation density fluctuates around a certain value, resulting from the balance between dislocation generation and dislocation annihilation. Further beyond UTS, some grain orientations show further work hardening while other grain orientations show softening, which leads to a slight increase in the dislocation density. In the fracture region, a significant increase of dislocation density is observed. It results from the reversal of elastic deformation (like a relatively compressive stress) which is absorbed by the measured area (outside the necking zone). Moreover, in the region from yield to half way between yield and UTS, i.e. elongation from 0.83 to 2.56 mm where dislocation generation is dominant, the correlation between flow stress and dislocation density satisfies the Taylor equation.

7. Anisotropic mechanical behavior along different directions of as-received AA 7020 plate

Besides the elastic anisotropy of single crystal which depends on the investigated material, crystallographic texture is a pronounced factor contributing to the anisotropic mechanical properties of materials such as aluminum [138-140]. Both elastic and plastic properties vary as the direction changes with respect to a specifically referential coordinate (for example the rolling coordinate), if the grains of the investigated material have preferred orientations. Therefore, the deformation of a textured material shows the characteristics of anisotropy such as the occurrence of earing during deep drawing of a textured sheet [3, 6]. During deformation, the stress in individual grains differ from the applied stress, which depend on how the grains are oriented with respect to the applied stress, the orientation correlation with neighboring grains and the interactions with the neighboring grains, making it difficult to predict how grains behave during deformation [20]. However, the stress states in specifically orientated grains can be visualized through the lattice strain [16, 90, 141], and the anisotropic mechanical behavior can be observed directly from the lattice strain evolution during deformation. In this chapter, the texture induced anisotropic mechanical behavior is investigated using the samples cut from the highly textured center layer of the as-received AA 7020-T6 plate, as mentioned in section 3.2. The lattice strain evolution along RD, 45° to RD and 90° to RD during uniaxial tension are analyzed.

7.1 Macro tensile curves and measured points

The LD of the three samples with respect to the Al (111) pole figure is shown in Fig. 7.1. The macro load-elongation curves of the samples along RD, 45° to RD and 90° to RD are shown in Fig. 7.2, which exhibit direction dependent stress strain behavior. In elastic region, due to the low elastic anisotropy of aluminum, the differences among the three samples are very small. But as the yield starts, the plastic anisotropy, which depends on the geometry of dislocation slips, can be immediately observed through the direction dependent yield strengths, as listed in Table. 7.1. The macro yield strength of the RD sample is the highest, while the 45°

to RD sample has the lowest one, and correspondingly, the UTS for the three samples have the same sequence. Besides, from yield to UTS, the working hardening rates are small and similar for all the three samples from macro scale.

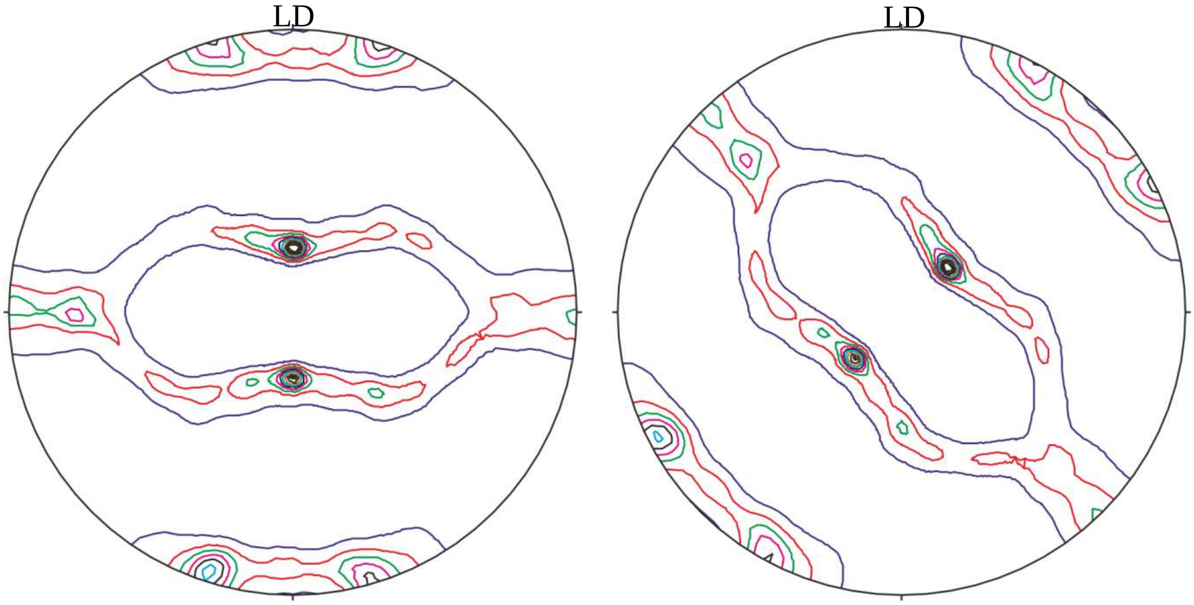

(a) LD // RD

(b) LD // 45° to RD

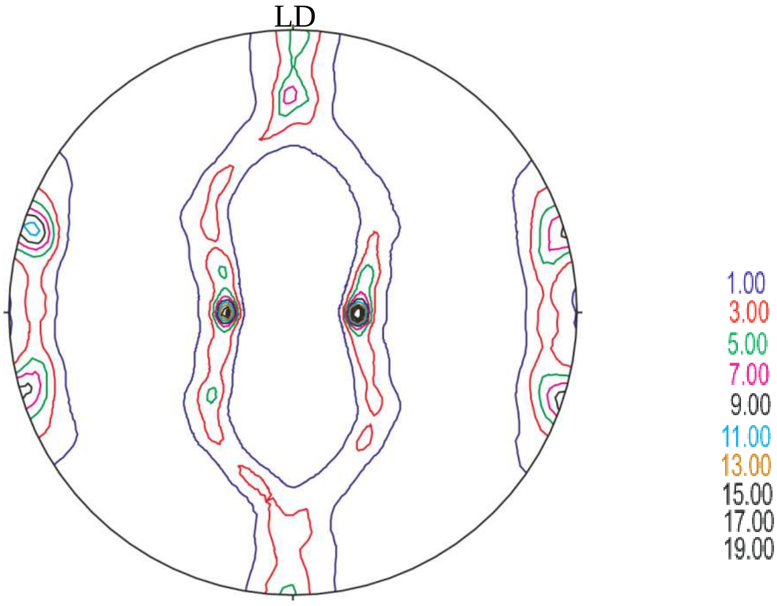

(c) LD // 90° to RD

Figure 7.1: Loading direction of the three samples with respect to Al (111) pole figure (maximum pole density P_{max} = 24 mrd).

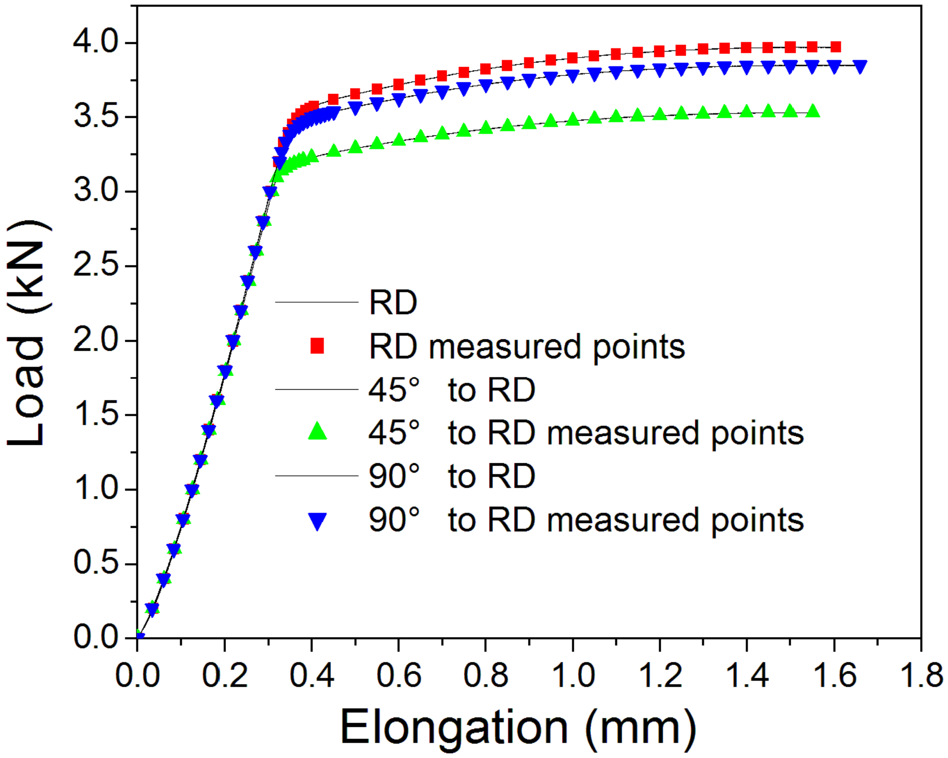

Figure 7.2: The load-elongation curves and measured points of the samples along RD, 45° to RD and 90° to RD.

Table 7.1: Direction dependent yield strengths.

Directions	RD	45° to RD	90° to RD
Yield strength	317.8 MPa	297.5 MPa	303.5 MPa

7.2 Calculations of the lattice strain

Diffraction pattern were collected at each measured point shown in Fig. 7.2. An image from the detector was shown in Fig. 7.3. The Debye-Scherrer rings correspond to the different {hkl} lattice planes oriented in such way that they satisfy the Bragg’s law with respect to the incident beam. Therefore, it is possible to determine the lattice strain of particular sets of crystallites which are orientated in certain directions such as a LD and perpendicular to LD.

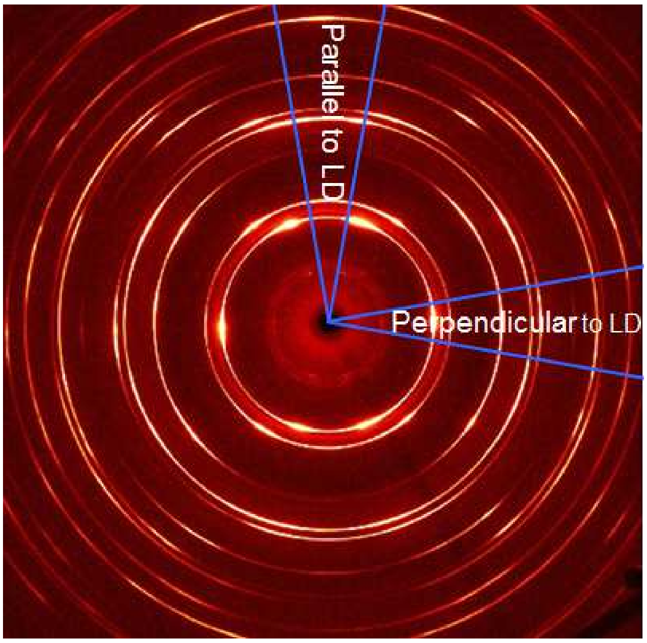

Figure 7.3: Integrated sectors along LD and along perpendicular to LD (sample LD//RD).

In order to get the lattice spacing of different {hkl} planes along LD and along perpendicular to LD, two sectors along these two directions, respectively, were integrated into 2θ-intensity spectrum, as shown in Fig. 7.3. The range of the sector is 10° in γ angle. After that, according to Bragg equation, $2d * \sin\theta = \lambda$, one can get the lattice spacing of different {hkl} planes along these two different directions. The lattice strain of specific {hkl} planes can be determined from the changes in lattice spacing using Eq. 2-33, but the d^{i}_{hkl} is the lattice spacing of the sample at the beginning of stable elastic deformation [142]. In the present study, the fifth measured point in Fig. 7.2 is chosen as the first point to calculate the lattice strain.

7.3 Results and discussion

The texture dependent lattice strain evolution of different {hkl} lattice planes both parallel to and perpendicular to the LD are shown in Fig. 7.4 for the three samples. Due to the strong texture, the intensities of some {hkl} peaks, either in parallel to or perpendicular to the LD, are so low that it is not possible to get the peak positions. Therefore, the lattice strain evolution of some lattice planes may be missing in some of the figures. From Fig. 7.4, one can see the texture induced anisotropy through the different responses of individual {hkl} planes oriented in different directions. In the randomly oriented aluminum, the lattice strains of other lattice planes are bounded by those of {111} and {200} lattice planes [143]. However, in the presently investigated samples, the lattice strains of other lattice planes are not bounded by those of {111} and {200} lattice planes due to the strong texture. The behavior of different lattice planes in the 45° and 90° to RD samples are more different than those in the RD sample.

As shown in Fig.7.4, different oriented lattice planes have different stress strain responses. The responses of different lattice planes under an external load depend on the single crystal properties, on how the lattice planes are oriented with respect to the loading axis and on how they interact with the neighboring grains. The first factor is intrinsic property of the material, while the last two are extrinsic factors, both of which exert influence on the geometry of dislocation slips, thereby influencing the stress strain responses of individual lattice planes.

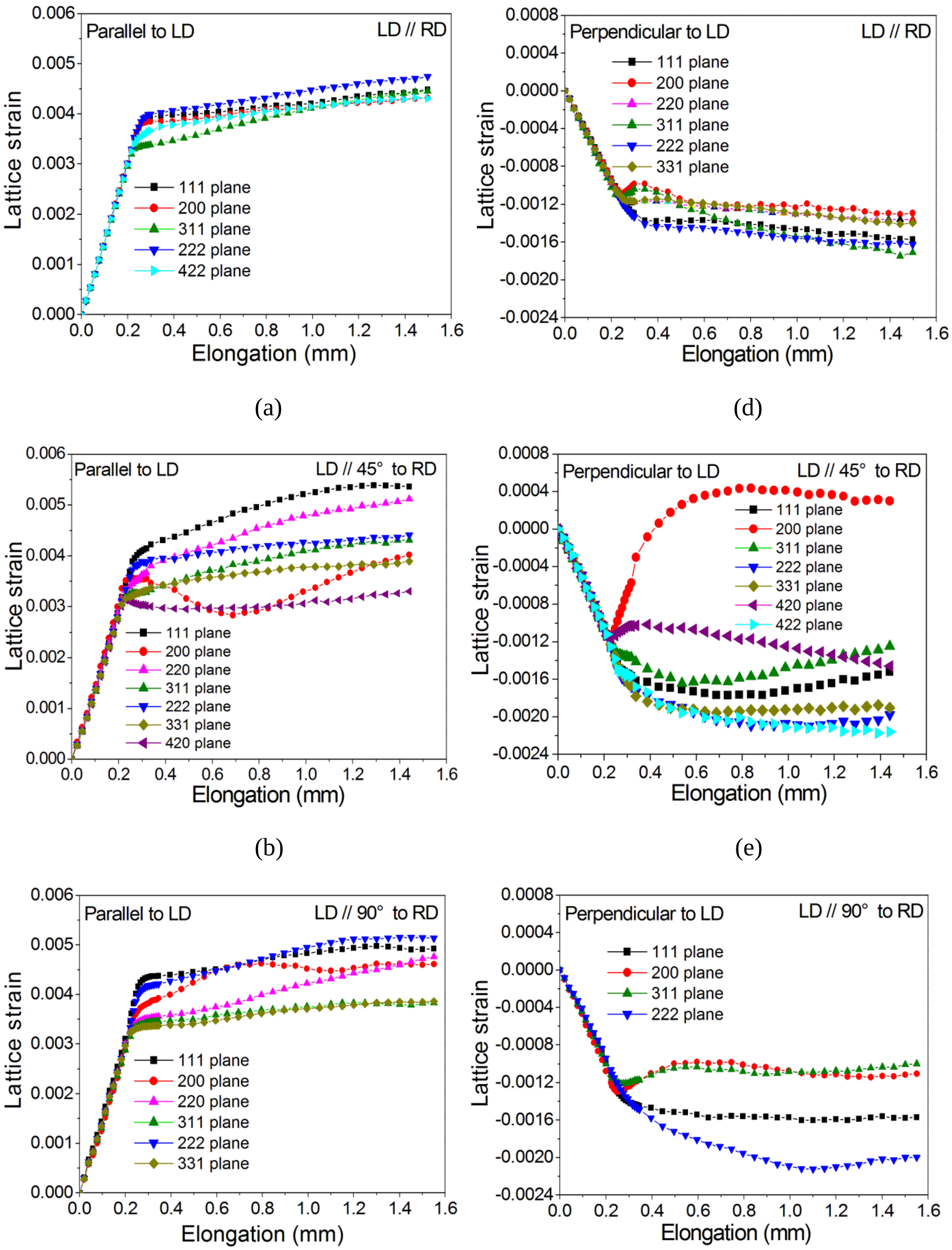

(a) (d)

(b) (e)

(c) (f)

Figure 7.4: Lattice strain evolution of the RD, 45° to RD and 90° to RD samples during uniaxial tension as a function of elongation. (a), (b) and (c) are the lattice strains parallel to LD. (d), (e) and (f) are the lattice strains perpendicular to LD.

7.3.1 Lattice strain in elastic region

In elastic region, parallel to LD, the lattice strains of different {hkl} lattice planes depend on both elastic anisotropy and texture. Since the elastic anisotropy of aluminum is small, which is expressed as $2C_{44}/(C_{11}-C_{12})$ with a value equal to 1.22, the lattice strain differences among different lattice planes are not pronounced, compared to those of copper and stainless steel which have higher elastic anisotropy [84]. The magnitudes of the lattice strains of {hkl} lattice planes are influenced by texture, which makes Young's moduli of different lattice planes depend on the orientations with respect to RD. The Young's modulus of a lattice plane can be determined by the slope of the linear fitting of applied stress vs. lattice strain in LD ($\Delta\sigma_{//} / \varepsilon_{//,hkl}$), while the Poisson ratio can be determined using the slope in LD divided by the minus value of the slope in the perpendicular to LD ($-\Delta\sigma_{\perp} / \varepsilon_{\perp,hkl}$), equal to ($-\varepsilon_{\perp,hkl} / \varepsilon_{//,hkl}$). Fig. 7.5 shows an example of how to obtain Young's modulus and Possion ratio. The yield strength of individual lattice planes can be determined from the stress-lattice strain plot. The stress value where the lattice strain starts to deviate from linearity is defined as the yield strength. The Young's moduli (E_{hkl}), Poisson ratios (ν_{hkl}) and yield strengths of the {hkl} lattice planes of the three samples are shown in Table 7.2. Owing to the strong texture, the intensities of some reflections in the 2θ-intensity spectrum are too low to determine the peak centers either along LD or along perpendicular to LD. Therefore, it is not possible to obtain the corresponding Young's modulus and Poisson's ratio, as shown in the Table 7.2. As can be seen from the table, the Young's moduli of the lattice planes in the 45° to RD are lower than those in the other two directions. The stiffest reflection {111} in randomly oriented polycrystalline aluminum is no longer the stiffest one in the three measured samples, i.e. the Young's modulus of {111} is not the largest one. Also, the softest reflection {200} in randomly oriented aluminum polycrystalline is not the softest one in the RD and 90° to RD samples. Texture influences the magnitude of lattice strain that a reflection undergoes during uniaxial tension. The magnitude depends on the texture itself, on how the lattice planes are oriented with respect to the LD and on the geometry limitation from the neighboring crystallites. It means that under the same external load, the lattice strains of {hkl} planes in a highly textured material are more limited by the neighboring crystallites than those in a randomly oriented material [121], because in a randomly oriented material different {hkl} lattice planes have equal probability to appear in a given direction. In this case a crystallite oriented in a given direction has equal chance to meet crystallites oriented in other directions. However, in a textured material, a crystallite may have more neighbors with specific orientation. Moreover, the specific orientation correlation between neighboring crystallites may exert influence on the crystallites' behavior [144]. It leads to the measured Young's moduli deviating from those calculated by the Kröner model [121]. For instance, there are very small amount of {200} planes with their normal parallel to LD in the 90° to RD sample, as shown in Table 7.3 (The volume fractions of {111} or {200} lattice planes orientated in a given direction were calculated by the software MTEX [117]). The external load is distributed more to the {111} lattice planes, making the lattice strain of {200} smaller than that of {111}. It causes the measured Young's modulus of the {200} to be larger than that of {111} in this sample.

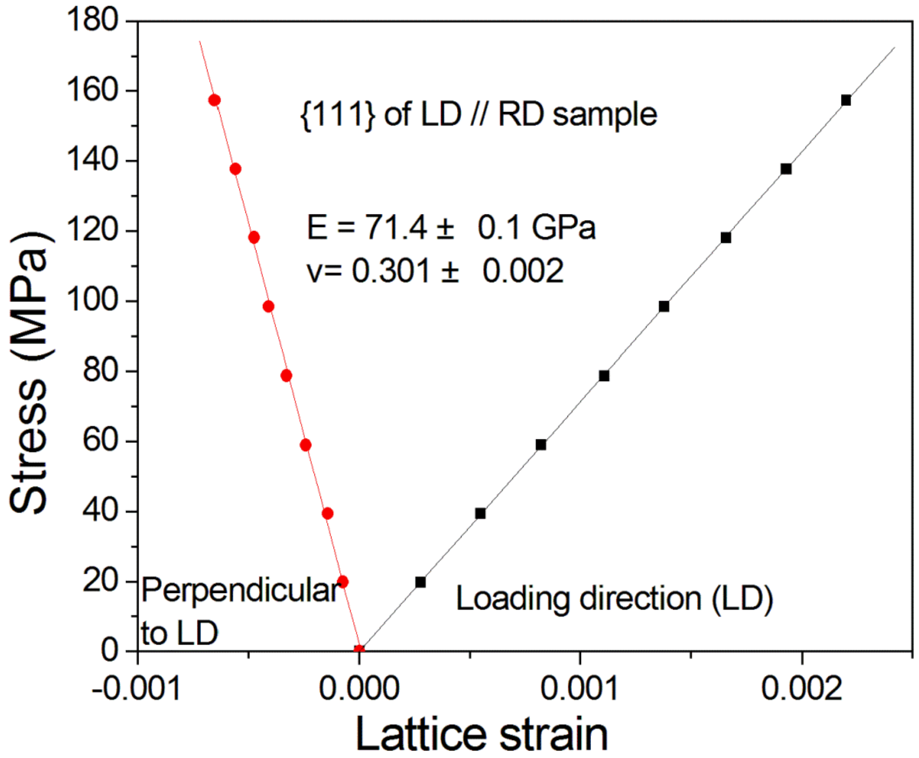

Figure 7.5: An example of determining the Young's modulus and Poisson ratio.

Table 7.2: Young's modulus, Poisson ratio and yield strength of different lattice planes.

Lattice plane	200	311	420	422	220	331	111
LD parallel to RD							
E_{hkl}/GPa	71.5±0.2	73.3±0.3	---	72.3±0.3	---	---	71.4±0.1
ν_{hkl}	0.298±0.004	0.322±0.003	---	---	---	---	0.301±0.002
YS/MPa	314.1	312.3	---	322.2	---	---	315.4
LD parallel to 45° to RD							
E_{hkl} /GPa	64.8±0.9	70.0±0.3	71.3±0.2	---	67.8±0.1	70.9±0.1	66.9±0.5
ν_{hkl}	0.338±0.007	0.362±0.006	0.374±0.004	---	0.332±0.004	0.368±0.002	0.355±0.006
YS/MPa	290.2	296.1	299.8	---	298.6	304.7	293.6
LD parallel to 90° to RD							
E_{hkl} /GPa	73.1±0.7	75.2±0.7	---	---	71.7±0.7	72.8±0.7	70.6±0.7
ν_{hkl}	0.368±0.009	0.349±0.007	---	---	---	---	0.323±0.006
YS/MPa	295.8	311.4	---	---	312.7	308.8	298.5
Values calculated by the Kröner model for random aluminum polycrystalline							
E_{hkl} /GPa	66.7	69.2	69.3	70.8	70.8	71.2	72.3
ν_{hkl}	0.358	0.352	0.352	0.349	0.349	0.348	0.346
	Macroscopic yield strength						
	LD parallel to RD		LD parallel to 45° to RD		LD parallel to 90° to RD		
YS/MPa	317.8		297.5		303.5		

Table 7.3: The amount of crystallites with the normal of {111} and {200} parallel or perpendicular to the LD (volume fraction %).

Samples	LD// RD	LD//45° to RD	LD//90° to RD
Crystallites with the normal of {111} parallel to the LD	0.147	0.025	0.172
Crystallites with the normal of {200} parallel to the LD	0.031	0.050	0.007
Crystallites with the normal of {111} perpendicular to the LD	0.172	0.028	0.147
Crystallites with the normal of {200} perpendicular to the LD	0.007	0.084	0.031

7.3.2 Lattice strain in elastic plastic transition region

When it approaches the elastic plastic transition region, anisotropic behavior of individual lattice planes oriented in different directions with respect to the rolling coordinates can be directly observed, which gives a hint of the texture induced anisotropy. The lattice strain differences among different {hkl} lattice planes are larger in the 45° and 90° to RD samples than those in the RD sample, indicative of a more diverse load redistribution, as shown in Fig. 7.4 (a) to (c).

Parallel to LD, in the RD sample, the lattice strain of {311} inflects while the lattice strains of {111}, {222} and {200} still increases linearly, indicating that in this sample the {111}, {222} and {200} are the lattice planes which carry more load in the elastic plastic transition region. Similarly, in the 45° to RD sample, {111} and {222} carry more load than {311}, {331} and {420}, and in the 90° to RD sample, {111} and {222} carry more load than {220}, {311} and {331}. All the other lattice planes appeared in Fig. 7 (a) to (c) but not mentioned above, carry load that are between maximum and minimum. In contrast, in the aluminum with random orientations, the {111} carries the highest load and the {200} carries the lowest load in the elastic plastic transition region [86]. Therefore, the lattice strain behavior shows that load redistribution in the elastic plastic transition region is texture-dependent. However, the {111} lattice planes are the main load carrier in all three samples. Perpendicular to LD, the lattice strains of different lattice planes are controlled by Poisson contraction and interaction between neighboring crystallites, which will be more discussed in the section 7.3.3.

The yield strengths of individual {hkl} lattice planes in different directions are shown in Table 7.2. The {hkl} lattice planes of the 45° to RD sample have the lowest yield strengths among the three samples, which reveal the reason why the macro yield strength of this sample is the lowest. Texture changes the dislocation slip geometry which is determined by both the orientations of the {hkl} lattice planes with respect to the LD and the orientations between {hkl} lattice planes and their neighboring crystallites. They lead to a larger resolved shear stress in the 45° to RD [145], resulting in the lower lattice plane dependent yield strength in this direction.

7.3.3 Lattice strain in the plastic region

In the plastic region, the differences of stress-strain response among {hkl} lattice planes are more evident than those in the elastic region, depending on the initial texture, as shown in Fig. 7.4. However, in this region parallel to LD, except the abnormal behavior of the {200} lattice planes, work hardening behavior can be mainly divided into two groups, which is deduced from the slope of the lattice strain *vs.* elongation curve, as shown in Fig. 7.4 (a)-(c). The first group shows a very small work hardening rate such as the {222} and {420} in the 45° to RD sample, as shown in Fig. 7.4 (b). The second group shows an increasing lattice strain curve. The slope of the lattice planes in this group is almost the same, e.g. the {111}, {220} and {311} in the 45° to RD sample. The work hardening behavior of the other lattice planes which do not belong to these two groups show intermediate situation between the two groups. When it gets close to UTS, the work hardening behavior of almost all lattice planes becomes similar, which may be attributed to the dislocation density inside the material. In chapter 6, it is found that dislocation generation and annihilation became balanced with each other in this region.

The two types of the work hardening behavior can be attributed to the stress states which the individual lattice planes undergo. Bishop established that four different types of crystallographic stress states can activate polyslip [127], and Kocks investigated the work hardening behavior of the different types of polyslip [125]. Based on their results, the two work hardening behavior are caused by the so called [100] tension and [111] tension stress states, respectively. The [100] tension stress state activates 8 slip systems. The combination of these 8 slip systems cannot make contributions to the hardening on the effected lattice planes. By contrast, the [111] tension stress state activates 6 slip systems, but it can harden the effected lattice planes. Those lattice planes whose work hardening behavior are between the two groups are in the stress state which is in the combination of the [100] tension and [111] tension.

The abnormal behavior of {200} lattice planes are attributed to two factors. One is the amount of crystallites with the normal of {200} lattice planes parallel to or perpendicular to the LD, i.e. texture, which are shown in Table 7.3. The other one is whether the <110> directions of the {200} planes are stressed or not, depending on the interactions between neighboring crystallites. When the <011> directions of the {200} planes are stressed, the activated slip systems are (111)[10-1], (111)[01-1], (11-1)[101] and (11-1)[011]. If the amount of slip on the 4 activated slip systems is the same, the deformation is asymmetric. It will cause large contraction in the [001] direction [86, 146]. If the contraction is along the LD, it will cause tensile stress to the {200} lattice planes, as shown in Fig. 7.4 (c). If the contraction is opposite the LD, it will cause a compressive stress to the {200} lattice planes, as shown in Fig. 7.4 (b).

However, as the deformation goes on, the lattice planes rotate in such way that the <110> directions of the {200} planes are not stressed, resulting in the decrease of the contraction along the [001] direction.

Perpendicular to LD, the lattice strain evolution after yield is mainly controlled by the Poisson contraction and the interactions among neighboring crystallites, the latter of which is strongly related to the texture. The effect of the interaction among neighboring crystallites can be demonstrated by lattice strain evolution differences of the {111} and {222} lattice planes, as shown in Fig. 7.4 (e) and (f). The reason for this is that the difference of the 2θ values for {111} and {222} is around 3.5° under the experimental condition. And notice that the lattice strain is averaged from the crystallites orientated within 10° around the direction perpendicular to LD. In this case, 3.5° is a large enough angle to change the environment of the neighboring crystallites, leading to different lattice strain evolution of the {111} and {222}. The lattice strain of {200} in the 45° to RD sample shows positive values, which indicates that both the <110> directions of {200} are stressed and there are sufficient amount of crystallites with the normal of {200} perpendicular to the LD, as shown in Fig. 7.4 (e) and Table 7.3. Under this condition, the contraction along the [001] direction can offset the Poisson contraction. However, in the RD and 90° to RD samples, there are not enough such crystallites so that the lattice strains of {200} only experience tensile stress at the beginning of this region, as shown in Fig. 7.4 (d) and (f).

7.4 Summery of the anisotropic mechanical behavior

The lattice strain evolution along the three directions, i.e. RD, 45° to RD and 90° to RD of a highly textured AA 7020-T6 alloy shows that the lattice-dependent Young’s moduli, yield strengths, the amount of {hkl} lattice planes oriented in a given direction and the interactions with the neighboring crystallites, leading to the macroscopic anisotropy which exhibits the lowest yield strength and UTS along the 45° to RD and highest along RD.

In the elastic region, the texture-dependent lattice strain evolution indicates that the 45° to RD sample have the smallest reflex-dependent Young’s modulus. Furthermore, the deviations of the measured Young’s moduli from those calculated by the Kröner model for polycrystalline aluminum with random orientations, are related to the amount of {hkl} lattice planes in a specific direction and the deforming limits from the neighboring crystallites.

In the elastic plastic region, due to the low elastic anisotropy of aluminum, the reflex-dependent yield strengths show only small variation for each sample. The 45° to RD sample has the lowest reflex-dependent yield strength among the three samples. The variation of lattice strain shows that differently oriented grains undergo different stresses. This effect is greatest in the 45° to RD sample.

In the plastic region, parallel to LD, the so called [100] tension and [111] tension stress states are dominant in all the three samples, resulting in two groups of strain hardening behavior. The abnormal behavior of {200} lattice planes is related to whether the <110> directions of {200} are stressed, which induces a contraction along the [001] direction. If the contraction along the [001] direction is parallel to the LD, it will induce a tensile stress on {200} lattice planes. If the contraction along the [001] direction is opposite to the LD, it will induce a compressive stress on {200} lattice planes. Perpendicular to LD, the lattice strain of individual lattice planes are controlled by the Poisson contraction and the interactions among the neighboring crystallites. The {200} lattice planes of the 45° to RD sample exhibit positive lattice strains due to both the contraction along the [001] direction of {200} lattice planes and the amount of {200} lattice planes, which are strongly related to the initial texture.

8. Conclusions and recommendations

1. The texture evolution of the AA 7020-T6 sample with initial texture sharpness around 10 mrd (loading axis parallel to RD) shows that the main orientations remain concentrating on copper type texture during tensile test due to the small deformation from initial state to sample fracture. The brass component shows an increasing trend during the whole tensile test. From yield to fracture, the volume fractions of grains with <111> and <100> parallel to the LD increase monotonously, indicating some grains tend to align their <111> and <100> to the LD.

2. Lattice strain evolution of the sample with initial texture sharpness around 10 mrd (loading axis parallel to RD) shows that in the elastic region, the {111} lattice planes are the stiffest ones, as in theory, but the {200} lattice planes are not the most compliant ones due to the interactions with neighboring grains having other orientations. The Young's modulus of {311} lattice planes is less affected by the texture with 10 mrd sharpness, which is almost the same as that of the {311} in a randomly oriented polycrystalline aluminum. In the plastic region, the work hardening behavior is mainly controlled by the two types dislocation arrangements, the so called [111] tension stress state and [100] tension stress state. Load release firstly starts on the {111} and {222} lattice planes before UTS. Further beyond UTS, all lattice planes experience load release.

3. The dislocation density evolution of the sample with initial texture sharpness around 10 mrd (loading axis parallel to RD) shows that in the elastic region, dislocation density decreases as the elongation increases. From yield to half way between yield and UTS, the dislocation density increases rapidly, which causes the work hardening. Near UTS, the dislocation density fluctuates around a certain value, resulting from the balance between dislocation generation and dislocation annihilation. Further beyond UTS, some grain orientations show further work hardening while other grain orientations show softening. It leads to a slight increase in the dislocation density. In the fracture region, a significant increase of dislocation density is observed. It results from the reversal of elastic deformation (like a relatively compressive stress) which is absorbed by the measured area

(outside the necking zone). Moreover, from yield to half way between yield and UTS, the correlation between flow stress and dislocation density satisfies the Taylor equation.

4. A method for correcting the peak broadening caused by sample thickness is developed for X-ray diffraction in transmission geometry.

5. Three flat tensile samples which exhibit the copper type texture with maximum orientation density of 29.7 mrd are used to investigate the anisotropic mechanical behavior induced by texture. The loading axes of the three samples are along RD, 45° to RD and 90° to RD, respectively. The uniaxial tensile tests were done till UTS, which show different yield strengths, UTS and elongations along the three directions. The macroscopic anisotropy is consistent with the reflex-dependent lattice strain evolution, which explains the correlation between crystallite orientations and different mechanical behavior. In the elastic region, the 45° to RD sample has the lowest reflex-dependent Young's modulus, compared to the other two directions. In the elastic plastic region, due to the low elastic anisotropy of aluminum, the reflex-dependent yield strengths show only small variation for each sample. The 45° to RD sample has the lowest reflex-dependent yield strength among the three samples. The variations of lattice strain show that differently oriented grains undergo different stresses. This effect is most evident in the 45° to RD sample. In the plastic region, the work hardening behavior of different {hkl} lattice planes are also controlled by the two types dislocation arrangements, the so called [111] tension stress state and [100] tension stress state. The {200} lattice planes of 45° to RD sample behave abnormally due to the stress along <110> of the {200} planes and the orientation density of {200} lattice planes parallel to and perpendicular to the LD, both of which are dependent on the texture.

Recommendations

There are numerous directions along which the work presented in this dissertation may be extended. However, the following points are recommended:

1. It is necessary to make simulations on the deformation behavior of a texture material, to find out the correlations among texture evolution, lattice strain evolution and dislocation evolution, using finite element model or elastoplastic self-consistent model.
2. To quantitatively describe the texture effects on the Young's modulus. This needs a model which takes into account the orientation correlation between neighboring grains, the amount of grains oriented in a special direction and the interactions between grains having different orientations.
3. It is necessary to develop a way to investigate how the dislocations evolve on any specific {hkl} lattice planes during tensile test.

References:

[1] D. Wilson. *Plastic anisotropy in sheet metals*, Inst. Metals J. 94 (1966), p. 84-93.

[2] P. Van Houtte, G. Cauwenberg, and E. Aernoudt. *Analysis of the earing behaviour of aluminium 3004 alloys by means of a single model based on yield loci calculated from orientation distribution functions*, Mat. Sci. & Eng. 95 (1987), p. 115-124.

[3] O. Engler and S. Kalz. *Simulation of earing profiles from texture data by means of a visco-plastic self-consistent polycrystal plasticity approach*, Mat. Sci. & Eng. A 373 (2004), p. 350-362.

[4] W. Hutchinson, A. Oscarsson, and Å. Karlsson. *Control of microstructure and earing behaviour in aluminium alloy AA 3004 hot bands*, Mater. Sci. Technol. 5 (1989), p. 1118-1127.

[5] V. Randle and O. Engler, *Introduction to texture analysis: macrotexture, microtexture and orientation mapping*, CRC Press, Boca Raton, 2000.

[6] O. Engler and J. Hirsch. *Polycrystal-plasticity simulation of six and eight ears in deep-drawn aluminum cups*, Mat. Sci. & Eng. A 452 (2007), p. 640-651.

[7] H.-J. Bunge and W. Roberts. *Orientation distribution, elastic and plastic anisotropy in stabilized steel sheet*, J. Appl. Cryst. 2 (1969), p. 116-128.

[8] R. Sowerby, D.C. Viana, and G. Davies. *The influence of texture on the mechanical response of commercial purity copper sheet in some simple forming processes*, Mat. Sci. & Eng. 46 (1980), p. 23-51.

[9] P. Lequeu, P. Gilormini, F. Montheillet, B. Bacroix, and J. Jonas. *Yield surfaces for textured polycrystals—I. Crystallographic approach*, Acta Metall. 35 (1987), p. 439-451.

[10] U.F. Kocks, C.N. Tomé, and H.-R. Wenk, *Texture and anisotropy: preferred orientations in polycrystals and their effect on materials properties*, Cambridge university press, 2000, p. 420-464.

[11] W. Lankford, S. Snyder, and J. Bauscher. *New criteria for predicting the press performance of deep drawing sheets*, Trans. ASM 42 (1950), p. 1197-1232.

[12] H. Tresca. *Memoir on the flow of solid bodies under strong pressure*, Comptes-rendus de l'académie des sciences 59 (1864), p. 754-758.

[13] R.v. Mises. *Mechanik der festen Körper im plastisch-deformablen Zustand*, Nachrichten von der Gesellschaft der Wissenschaften zu Göttingen, Mathematisch-Physikalische Klasse 1913 (1913), p. 582-592.

[14] U.F. Kocks. *The Sensitivity of Yield Surface Predictions to the Details of a Texture*, *11th international conference on textures of materials*, ed. Liang Zhide, Zuo Liang, and C. Youyi, 1996, Xi'an China, International academic Publishers. p. 763-767.

[15] M.R. Daymond and N.W. Bonner. *Lattice strain evolution in IMI 834 under applied stress*, Mat. Sci. & Eng. A 340 (2003), p. 272-280.

[16] E. Oliver, M. Daymond, and P. Withers. *Interphase and intergranular stress generation in carbon steels*, Acta Mater. 52 (2004), p. 1937-1951.

[17] H. Poulsen, S. Garbe, T. Lorentzen, D. Juul Jensen, F. Poulsen, N. Andersen, T. Frello, R. Feidenhans'l, and H. Graafsma. *Applications of high-energy synchrotron radiation for structural studies of polycrystalline materials*, Journal of synchrotron radiation 4 (1997), p. 147-154.

[18] B. Clausen, T. Lorentzen, and T. Leffers. *Self-consistent modelling of the plastic deformation of fcc polycrystals and its implications for diffraction measurements of internal stresses,* Acta Mater. 49 (1998), p. 3087-3098.

[19] P. Dawson, D. Boyce, S. MacEwen, and R. Rogge. *On the influence of crystal elastic moduli on computed lattice strains in AA-5182 following plastic straining,* Mat. Sci. & Eng. A 313 (2001), p. 123-144.

[20] M. Daymond, C. Tomé, and M. Bourke. *Measured and predicted intergranular strains in textured austenitic steel,* Acta Mater. 48 (2000), p. 553-564.

[21] I. Polmear. *The Ageing Characteristics of Ternary Aluminium-Zinc-Magnesium Alloys*, J. Inst. Metals 86 (1957), p. 113-121.

[22] E.A. STARKE JR. *Heat-treatable aluminum alloys*, Aluminum Alloys-Contemporary Research and Applications: Contemporary Research and Applications 31 (2012), p. 35-63.

[23] J.T. Staley, *History of wrought-aluminum-alloy development*, in A.K. Vasudevan and R.D. Doherty (eds.), *Aluminum Alloys--Contemporary Research and Applications: Contemporary Research and Applications*, Elsevier, 1989, p. 3-31.

[24] A. Sheikh. *Precipitation Hardening and Substructure Features in Al--Zn--Mg Alloys*, Strength of Metals and Alloys. 1 (1985), p. 483-488.

[25] J. Lendvai. *Precipitation and strengthening in aluminium alloys*, *Materials Science Forum*1996, Trans Tech Publ. p. 43-56.

[26] T. Sanders. *Review of fatigue and fracture research on high-strength aluminum alloys*, Fatigue and microstructure (1979), p. 467-522.

[27] S.P. Ringer, B.C. Muddle, and I.J. Polmear. *Effects of cold work on precipitation in Al-Cu-Mg-(Ag) and Al-Cu-Li-(Mg-Ag) alloys,* Metall. Mater. Trans. A 26 (1995), p. 1659-1671.

[28] V. Bulatov and W. Cai, *Computer simulations of dislocations,* Oxford University Press, New York, 2006.

[29] R. Heidenreich and W. Shockley. *Study of slip in aluminum crystals by electron microscope and electron diffraction methods*, *Report of a Conference on Strength of Solids: Held at the HH Wills Physical Laboratory, University of Bristol, on 7-9 July 1947*, Physical Society. p. 57.

[30] A. Cottrell, *Dislocation and plastic flow in crystals*, Clarendon Press, Oxford, 1953.

[31] L.E. Murr. *Interfacial phenomena in metals and alloys*, Addison-Wesley Publishing Company, 1975.

[32] D. Hull and D.J. Bacon, *Introduction to dislocations*, Butterworth-Heinemann, 2001.

[33] A.S. Argon and W. Moffatt. *Climb of extended edge dislocations*, Acta Metall. 29 (1981), p. 293-299.

[34] E. Schmid and W. Boas. *Plasticity of crystals,* F.A. Hughes & Co. Limited, 1950.

[35] W.F. Hosford. *The mechanics of crystals and textured polycrystals*, Oxford University Press, New York, 1993.

[36] G. Sachs. *On the Derivation of a Condition of Flow*, Z. Verein. Deutsch. Ing 72 (1928), p. 734.

[37] G.I. Taylor. *Plastic strain in metals*, J. Inst. Metals 62 (1938), p. 307-324.

[38] G.I. Taylor. *Analysis of plastic strain in a cubic crystal*, Stephen Timoshenko 60th

Anniversary Volume (1938), p. 218-224.

[39] J. Bishop and R. Hill. *A theory of the plastic distortion of a polycrystalline aggregate under combined stresses*, Philosophical magazine 42 (1951), p. 414-427.

[40] J. Bishop and R. Hill. *A theoretical derivation of the plastic properties of a polycrystalline face-centred metal*, Philosophical Magazine Series 7 42 (1951), p. 1298-1307.

[41] H.J. Bunge, *Texture Analysis in Materials Science*, Cuvillier Verlag, Göttingen, 1993.

[42] P. Van Houtte and E. Aernoudt. *Considerations on the crystal and the strain symmetry in the calculation of deformation textures with the Taylor theory*, Mat. Sci. & Eng. 23 (1976), p. 11-22.

[43] H.-G. Brokmeier and S. Yi, *Texture and Texture Analysis in Engineering Materials*, in W. Reimers, A.R. Pyzalla, A. Schreyer, and H. Clemens (eds.), *Neutrons and synchrotron radiation in engineering materials science*, Wiley-VCH Verlag GmbH & Co. KGaA, Weinheim, 2008.

[44] R.J. Roe. *Description of Crystallite Orientation in Polycrystalline Materials. III. General Solution to Pole Figure Inversion* J. Appl. Phys. 36 (1965), p. 2024-2031.

[45] S. Matthies. *On the basic elements of and practical experiences with the WIMV algorithm—an odf reproduction method with conditional ghost correction*, *Proceedings of the Eighth International Conference on Textures of Materials ICOTOM*1987. p. 37-48.

[46] M. Dahms and H.J. Bunge. *The iterative series-expansion method for quantitative texture analysis. I. General outline*, J. Appl. Cryst. 22 (1989), p. 439-447.

[47] W.R. Hibbard. *Effect of Composition on the Wire Texture of Copper and Its Solid Solution Alloys*, Transactions of the Metallurgical Society of the American Institute of Mining and Metallurgical Engineers 195 (1949), p. 598.

[48] W.R. Hibbard. *Deformation Texture of Drawn Face-Centered Cubic Metal Wires*, J Inst. Metals 77 (1950), p. 581-584.

[49] J. Grewen and G. Wassermann. *Texture-Analysis of Wires I. Deformation- and Recrystallization Textures of Brass, Copper and Silver*, Z. Metallkde 45 (1954), p. 499-505.

[50] H.J. Bunge, H. Sandmann. *Zur Berechnung der reziproken Polfigur von Fasertexturen mit Hilfe des Rechenautomaten URAL I.*, Mber. Dt. Akad. Wiss. 5 (1963), p. 344-350.

[51] C. McHargue, L. Jetter, and J. Ogle. *Preferred orientation in extruded aluminum rod*, Trans. Met. Soc. AIME 215 (1959), p. 831-837.

[52] A. English and G. Chin. *On the variation of wire texture with stacking fault energy in fcc metals and alloys*, Acta Metall. 13 (1965), p. 1013-1016.

[53] G. Chin. *Textures in research and practice*, Proc. of the Int. Syrup. Clausthal-Zellerfeld, Springer Verlag, Berlin-Heidelberg-New York,1969.

[54] H. Mecking. *Textures in metals, Preferred Orientation in Deformed Metals and Rocks: An Introduction to Modern Texture Analysis*, ed. H.R. Wenk, 1985, New York, Academic Press. p. 267-306.

[55] J. Gil Sevillano, P. Van Houtte, and E. Aernoudt. *Large strain work hardening and textures*, Progress in Materials Science 25 (1980), p. 69-134.

[56] R. Smallman and D. Green. *The dependence of rolling texture on stacking fault energy*, Acta Metall. 12 (1964), p. 145-154.

[57] I. Dillamore and W. Roberts. *Rolling textures in fcc and bcc metals*, Acta Metall. 12 (1964), p. 281-293.

[58] J. Venables. *The electron microscopy of deformation twinning*, J. Phys. Chem. Solids 25 (1964), p. 685-692.

[59] H. Hu, R. Cline, and S. Goodman. *Deformation textures of metals, Recrystallization, Grain Growth and Textures,* ed. H. Margolin, 1966, Ohio, American Society of Metals, Metals Park,. p. 295-366.

[60] I. Dillamore and W. Roberts. *Preferred orientation in wrought and annealed metals,* Metallurgical reviews 10 (1965), p. 271-380.

[61] H. Hu, P. Sperry, and P.A. Beck. *Rolling textures in face-centered cubic metals*, J. Metals (NY) 4 (1952), p. 76-83.

[62] Y. Liu and R. Richman. *The evolution of textures in fcc metals. 1. Alloys of copper with germanium and tin*, Trans. Met. Soc. AIME 218 (1960), p. 688-699.

[63] R. Richman and Y. Liu. *The evolution of textures in fcc metals, 2. Alloys of copper with phosphorus , arsenic and antimony*, Trans. Met. Soc. AIME 221 (1961), p. 720-732.

[64] P.A. Beck and A. Merlini. *Effect of Zinc Content on the Rolling Texture And Annealing Texture of Alpha Brass*, Trans. Met. Soc. AIME 203 (1955), p. 385-393.

[65] S. Goodman and H. HU. *Texture transition in copper*, Trans. Met. Soc. AIME 227 (1963), p. 627-639.

[66] H. Hu and R. Cline. *Temperature Dependence of Rolling Textures in High - Purity Silver*, J. Appl. Phys. 32 (1961), p. 760-763.

[67] H. Hu, R. Cline, and S. Goodman. *Texture Transition in High ‐Purity Silver and Its Correlation with Stacking Fault Frequency,* J. Appl. Phys. 32 (1961), p. 1392-1399.

[68] F. Haessner. Zur Theorie der Walztexturen Kubisch Flachenzentrierter, Z. Metallkunde 54 (1963), p. 98-111.

[69] C. Beevers and R. Honeycombe. *Cubic slip in aluminium alloy crystals,* Acta Metall. 9 (1961), p. 513-515.

[70] H. Ahlborn, J. Grewen, and G. Wassermann. *The question of the origin of rolling textures in fcc metals,* Z. Metallkunde 55 (1964), p. 598-599.

[71] H. Honneff and H. Mecking. *A method for the determination of the active slip systems and orientation changes during single crystal deformation,* Textures of Materials, 1 (1978), p. 265-275.

[72] J. Hirsch and K. Lücke. *Overview no. 76: Mechanism of deformation and development of rolling textures in polycrystalline fcc metals—I. Description of rolling texture development in homogeneous CuZn alloys,* Acta Metall. 36 (1988), p. 2863-2882.

[73] J. Kallend and G. Davies. *The Development of Texture in Copper and Copper-Zinc Alloys,* Texture 1 (1972), p. 51-69.

[74] H.J. Bunge and F. Haessner. *Three ‐Dimensional Orientation Distribution Function of Crystals in Cold ‐Rolled Copper*, J. Appl. Phys. 39 (1968), p. 5503-5514.

[75] J. Hirsch, K.H. Virnish, and K. Lücke. *ICOTOM 6*, ed. S. Nagashima, 1981, Tokyo, Japan, ISIJ. p. 375-381.

[76] O. Engler, J. Hirsch, and K. Lücke. *Texture development in Al 1.8 wt% Cu depending on the precipitation state—I. Rolling textures*, Acta Metall. 37 (1989), p. 2743-2753.

[77] K. Lücke and O. Engler. *Effects of particles on development of microstructure and*

texture during rolling and recrystallisation in fcc alloys, Mater. Sci. Technol. 6 (1990), p. 1113-1130.

[78] http://www.science3d.org/content/basic-principles-x-ray-tomography-x-rays.

[79] H.J. Bunge. *Texture and microstructure analysis with high-energy synchrotron radiation*, Powder Diffraction 19 (2004), p. 60-64.

[80] F. Heidelbach, C. Riekel, and H.-R. Wenk. *Quantitative texture analysis of small domains with synchrotron radiation X-rays*, J. Appl. Cryst. 32 (1999), p. 841-849.

[81] H.-R. Wenk and S. Grigull. *Synchrotron texture analysis with area detectors*, J. Appl. Cryst. 36 (2003), p. 1040-1049.

[82] S. Backstrom, C. Riekel, S. Abel, H. Lehr, and H. Wenk. *Microtexture analysis by synchrotron-radiation X-ray diffraction of nickel-iron alloys prepared by microelectroplating*, J. Appl. Cryst. 29 (1996), p. 118-124.

[83] J. Clusters. *Betrachtung über Metalltexturen*, Philips Tech. Rundschau 7 (1942), p. 13-20.

[84] B. Clausen, T. Lorentzen, and T. Leffers. *Self-consistent modelling of the plastic deformation of fcc polycrystals and its implications for diffraction measurements of internal stresses*, Acta Mater. 46 (1998), p. 3087-3098.

[85] B. Clausen, T. Lorentzen, M.A. Bourke, and M.R. Daymond. *Lattice strain evolution during uniaxial tensile loading of stainless steel*, Mat. Sci. & Eng. A 259 (1999), p. 17-24.

[86] B. Clausen, PhD thesis: Characterization of Pollycrystal Deformation, Risϕ National Laboratory, 1997, Denmark.

[87] B. Clausen and M. Bourke. *Lattice plane response during tensile loading of an aluminum 2 percent magnesium alloy*, Metall. Mater. Trans. A 32 (2001), p. 691-694.

[88] C. Neil, J. Wollmershauser, B. Clausen, C. Tomé, and S. Agnew. *Modeling lattice strain evolution at finite strains and experimental verification for copper and stainless steel using in situ neutron diffraction*, Int. J. Plast. 26 (2010), p. 1772-1791.

[89] A. Kanjarla, R. Lebensohn, L. Balogh, and C. Tomé. *Study of internal lattice strain distributions in stainless steel using a full-field elasto-viscoplastic formulation based on fast Fourier transforms*, Acta Mater. 60 (2012), p. 3094-3106.

[90] J. Pang, T. Holden, and T. Mason. *In situ generation of intergranular strains in an Al7050 alloy*, Acta Mater. 46 (1998), p. 1503-1518.

[91] M. Daymond and P. Withers. *A synchrotron radiation study of transient internal strain changes during the early stages of thermal cycling in an Al/SiCw MMC*, Scripta Mater. 35 (1996), p. 1229-1234.

[92] M. Miller, J. Bernier, J.-S. Park, and A. Kazimirov. *Experimental measurement of lattice strain pole figures using synchrotron x rays*, Review of scientific instruments 76 (2005), p. 113903.

[93] A. Cervellino, P. Derlet, and H. Van Swygenhoven. *Elastic properties determined from in situ X-ray diffraction*, Acta Mater. 54 (2006), p. 1851-1856.

[94] H.-G. Brokmeier, U. Zink, T. Reinert, and W. Murach. *The new loading device for texture measurement on the neutron diffractometer TEX-2*, J. Appl. Cryst. 29 (1996), p. 501-502.

[95] A.P. Hammersley, S.O. Svensson, M. Hanfland, A.N. Fitch, and D. Hausermann. *Two-dimensional detector software: from real detector to idealised image or two-theta*

scan, International Journal of High Pressure Research 14 (1996), p. 235-248.

[96] P. Scherrer. *Determination of the size and inner structure of colloid particles by X-rays.[Bestimmung der Größe und der inneren Struktur von Kolloidteilchen mittels Röntgenstrahlen.]*, Nach. Ges. Wiss. Gottingen 26 (1918), p. 98-100.

[97] A.R. Stoke and A.C.J. Wilson. *The diffraction of X rays by distorted crystal aggregates - I*, Proc. Phys. Soc. 56 (1944), p. 174-181.

[98] T. Ungar. *Microstructural parameters from X-ray diffraction peak broadening,* Scripta Mater. 51 (2004), p. 777-781.

[99] G. Williamson and W. Hall. *X-ray line broadening from filed aluminium and wolfram,* Acta Metall. 1 (1953), p. 22-31.

[100] B. Warren and B. Averbach. *The separation of cold‐work distortion and particle size broadening in X‐ray patterns*, J. Appl. Phys. 23 (1952), p. 497-497.

[101] B.E. Warren, *X-ray Diffraction*, Addison-Wesley, New York, 1970.

[102] G. Caglioti, A.t. Paoletti, and F. Ricci. *Choice of collimators for a crystal spectrometer for neutron diffraction*, Nuclear Instruments 3 (1958), p. 223-228.

[103] B.E. Warren. *X-ray studies of deformed metals* Prog. Met. Phys. 3 (1959), p. 147-202.

[104] M.A. Krivoglaz, *Theory of X-ray and Thermal-neutron Scattering by Real Crystals*, Plenum Press, London, 1969.

[105] M. Krivoglaz and K. Ryaboshapka. *The effect of dislocations on line profiles*, Phys. Met. Metallogr 15 (1963), p. 18-27.

[106] M. Wilkens. *The determination of density and distribution of dislocations in deformed single crystals from broadened X‐ray diffraction profiles*, Physica status solidi (a) 2 (1970), p. 359-370.

[107] M. Wilkens. *Theoretical aspects of kinematical X-ray diffraction profiles from crystals containing dislocation distributions(Fourier transform of X ray diffraction line profiles from crystals with dislocations)*, NBS Fundamental Aspects of Dislocation Therory 2, 1970.

[108] T. Ungár, J. Gubicza, P. Hanák, and I. Alexandrov. *Densities and character of dislocations and size-distribution of subgrains in deformed metals by X-ray diffraction profile analysis*, Mat. Sci. & Eng. A 319-321 (2001), p. 274-278.

[109] R. Kuzel and P. Klimanek. *X-ray diffraction line broadening due to dislocations in non-cubic materials. II. The case of elastic anisotropy applied to hexagonal crystals*, J. Appl. Cryst. 21 (1988), p. 363-368.

[110] I. Groma, T. Ungár, and M. Wilkens. *Asymmetric X-ray line broadening of plastically deformed crystals. I. Theory*, J. Appl. Cryst. 21 (1988), p. 47-54.

[111] T. Ungɑ́r and G. Tichy. *The Effect of Dislocation Contrast on X‐Ray Line Profiles in Untextured Polycrystals*, Physica status solidi (a) 171 (1999), p. 425-434.

[112] T. Ungár, I. Dragomir, Á. Révész, and A. Borbély. *The contrast factors of dislocations in cubic crystals: the dislocation model of strain anisotropy in practice*, J. Appl. Cryst. 32 (1999), p. 992-1002.

[113] S.-B. Yi, H.-G. Brokmeier, R. Bolmaro, K. Kainer, and T. Lippmann. *In situ measurements of texture variations during a tensile loading of Mg-alloy AM20 using synchrotron X-ray radiation*, Scripta Mater. 51 (2004), p. 455-460.

[114] H.G. Brokmeier, S.B. Yi, N.J. Park, and J. Homeyer. *In Situ Texture Analysis Using*

Hard X-Rays, Solid State Phenomena 105 (2005), p. 55-60.

[115] S.-B. Yi, C. Davies, H.-G. Brokmeier, R. Bolmaro, K. Kainer, and J. Homeyer. *Deformation and texture evolution in AZ31 magnesium alloy during uniaxial loading*, Acta Mater. 54 (2006), p. 549-562.

[116] R. Hielscher and H. Schaeben. *A novel pole figure inversion method: specification of the MTEX algorithm*, J. Appl. Cryst. 41 (2008), p. 1024-1037.

[117] F. Bachmann, R. Hielscher, and H. Schaeben. *Texture analysis with MTEX–free and open source software toolbox*, Solid State Phenomena 160 (2010), p. 63-68.

[118] O.A. Ruano and G. Gonzalez. *Texture changes during the tensile deformation of a fine grained aluminium alloy*, Scripta metallurgica 19 (1985), p. 27-31.

[119] A. Pandey, A.S. Khan, E.-Y. Kim, S.-H. Choi, and T. Gnäupel-Herold. *Experimental and numerical investigations of yield surface, texture, and deformation mechanisms in AA5754 over low to high temperatures and strain rates*, Int. J. Plast. 41 (2013), p. 165-188.

[120] G.E. Dieter and D. Bacon, *Mechanical metallurgy*. Vol. 3, McGraw-Hill, New York, 1986.

[121] M. Kamaya. *A procedure for estimating Young's modulus of textured polycrystalline materials*, International Journal of Solids and Structures 46 (2009), p. 2642-2649.

[122] J. Chinella. *Development of low cost, high performance AlZn4.5Mg1 alloy 7020, Aluminum alloys: Fabrication, Characterization and Application II*, ed. W. Yin, S.K. Das, and Z. Long, 2009.

[123] S. Kumar and T. Namboodhiri. *Precipitation hardening and hydrogen embrittlement of aluminum alloy AA7020*, Bull. Mater. Sci. 34 (2011), p. 311-321.

[124] A.K. Kanjarla, P. Van Houtte, and L. Delannay. *Assessment of plastic heterogeneity in grain interaction models using crystal plasticity finite element method*, Int. J. Plast. 26 (2010), p. 1220-1233.

[125] U. Kocks. *Polyslip in single crystals*, Acta Metall. 8 (1960), p. 345-352.

[126] W.F. Hosford, *Mechanical behavior of materials*, Cambridge University Press, New York, 2010.

[127] J. Bishop. *VI. A theoretical examination of the plastic deformation of crystals by glide*, Philosophical Magazine 44 (1953), p. 51-64.

[128] T. Ungar, J. Langford, R. Cernik, G. Vörös, R. Pflaumer, G. Oszlanyi, and I. Kovacs. *Microbeam X-ray diffraction studies of structural properties of polycrystalline metals by means of synchrotron radiation*, Mat. Sci. & Eng. A 247 (1998), p. 81-87.

[129] H.-G. Brokmeier, R.E. Bolmaro, Z. Z.Y., and S. N. *Line Broadening influenced by sample geometry*, HASYLAB Annual Report 2011 (2011)

[130] S. Brandstetter, P. Derlet, S. Van Petegem, and H. Van Swygenhoven. *Williamson–Hall anisotropy in nanocrystalline metals: X-ray diffraction experiments and atomistic simulations*, Acta Mater. 56 (2008), p. 165-176.

[131] T. Ungár. *Dislocation densities, arrangements and character from X-ray diffraction experiments*, Mat. Sci. & Eng. A 309 (2001), p. 14-22.

[132] P. Scardi and M. Leoni. *Fourier modelling of the anisotropic line broadening of X-ray diffraction profiles due to line and plane lattice defects*, J. Appl. Cryst. 32 (1999), p. 671-682.

[133] J. Gubicza, M. Kassem, and T. Ungar. *The microstructure of mechanically alloyed nanocrystalline aluminium-magnesium*, Mater. Sci. Forum 443-444 (2004), p. 103-106.

[134] A. Borbely, J. Dragomir-Cernatescu, G. Ribarik, and T. Ungar. *Computer program ANIZC for the calculation of diffraction contrast factors of dislocations in elastically anisotropic cubic, hexagonal and trigonal crystals*, J. Appl. Cryst. 36 (2003), p. 160-162.

[135] U. Kocks and H. Mecking. *Physics and phenomenology of strain hardening: the fcc case*, Progress in Materials Science 48 (2003), p. 171-273.

[136] F.R.N. Nabarro, Z.S. Basinski, and D. Holt. *The plasticity of pure single crystals*, Advances in Physics 13 (1964), p. 193-323.

[137] N. Hansen and X. Huang. *Microstructure and flow stress of polycrystals and single crystals*, Acta Mater. 46 (1998), p. 1827-1836.

[138] O. Engler and Y. An. *Correlation of texture and plastic anisotropy in the Al-Mg alloy AA 5005*, Solid State Phenom. 105 (2005), p. 277-284.

[139] M. Zaidi and T. Sheppard. *Control of earing quality in AA 5052 and AA 5454 aluminium alloys*, Mater. Sci. Technol. 1 (1985), p. 593-599.

[140] P. Bate and Y. An. *Plastic anisotropy in AA5005 Al–1Mg: predictions using crystal plasticity finite element analysis*, Scripta Mater. 51 (2004), p. 973-977.

[141] J. Quinta da Fonseca, E. Oliver, P. Bate, and P. Withers. *Evolution of intergranular stresses during in situ straining of IF steel with different grain sizes*, Mat. Sci. & Eng. A 437 (2006), p. 26-32.

[142] E. Maawad, H.-G. Brokmeier, Z.Y. Zhong, N. Al-Hamdany, M. Salih, L. Wagner, and N. Schell. *Determination of polycrystal diffraction elastic constants of Ti–2.5 Cu by using in situ tensile loading and synchrotron radiation*, Mat. Sci. & Eng. A 594 (2014), p. 62-67.

[143] A. Korsunsky, M. Daymond, and K. James. *The correlation between plastic strain and anisotropy strain in aluminium alloy polycrystals*, Mat. Sci. & Eng. A 334 (2002), p. 41-48.

[144] H. Bunge, *Physical properties of polycrystals*, (eds.), *Preferred Orientation in Deformed Metals and rocks: An introduction to modern texture analysis*, Academic Press, Inc Orlando, FL, 1985, p. 507-525.

[145] N. Lee, J. Chen, P.-W. Kao, L. Chang, T. Tseng, and J. Su. *Anisotropic tensile ductility of cold-rolled and annealed aluminum alloy sheet and the beneficial effect of post-anneal rolling*, Scripta Mater. 60 (2009), p. 340-343.

[146] W. Hosford. *Microstructural Changes During Deformation of (011) Fiber-Textured Metals*, Trans. Met. Soc. AIME 230 (1964), p. 12-15.

Curriculum Vitae

ZHONG, Zhengye

Personal Information

Surname, name:	Zhong, Zhengye
Sex:	Male
Date of birth:	30.01.1984
Place of birth:	Chengdu City, Sichuan Province, China
Nationality:	Chinese
Marital status:	Single
Address:	Windmühlenweg 27 22607, Hamburg, Germany
Tel.:	+49 (0) 157 8113 996 or +49 (0) 40 8998 6906
E-mail:	zhongzhengye@163.com zhengye.zhong@hzg.de

Academic Qualifications

09/2003 – 07/2007	Bachelor degree Materials Science and Engineering Chongqing University
09/2007 – 01/2010	M. Eng. degree Materials Science and Engineering Chongqing University
03/2010 – 09/2010	PhD student Materials Science and Engineering Chongqing University
Since 10/2010	PhD student Institute of Materials Science and Engineering Clausthal University of Technology, Germany

Employment

09/2007 – 01/2010	Teaching assistant at Institute of Materials Science and Engineering, Chongqing University, China.
Since 10/2010	Research assistant at the Institute of Materials Science and Engineering, Clausthal University of Technology, Germany.

Research Experience

- Measurement and analysis of crystallographic texture and residual stress using laboratory X-ray, synchrotron X-ray diffraction and neutron diffraction
- Peak broadening analysis using laboratory X-ray and synchrotron X-ray diffraction.
- Analysis of the anisotropic micromechanical behavior of different {hkl} lattice planes oriented in different directions of textured materials using in situ tensile test with synchrotron X-ray diffraction.
- Phase analysis using laboratory X-ray and synchrotron X-ray diffraction.

Research Interests

- Peak broadening analysis to get the microstructure information such as dislocation density, coherently diffraction domain size.
- In situ investigation of crystallographic texture evolution during deformation using synchrotron X-ray diffraction.
- In situ investigation of phase transformation during heating or deformation using synchrotron X-ray diffraction.
- In situ investigation of anisotropic mechanic behavior of textured material by uniaxial tensile test using synchrotron X-ray diffraction.

Work Responsibilities

- Measurement and analysis of residual stress and crystallographic texture using laboratory and synchrotron X-ray diffraction.
- Peak broadening analysis of deformed materials using laboratory and synchrotron X-ray diffraction.
- Phase analysis using laboratory and synchrotron X-ray diffraction.
- Analysis of anisotropic mechanic behavior of textured materials.

Publications

Year	Publication
2011	H. -G. Brokmeier, R. Bolmaro, Z.Y. Zhong, N. Schell and T. Lippmann, Line broadening influenced by the sample geometry, DESY Annual Report 2011.
	H. -G. Brokmeier, T. Lychagina, D. Nikolayev, B. Schwebke and Z.Y. Zhong, Investigation of texture inhomogeneity in magnesium alloy MA2-1 after equal channel angular pressing (ECAP), DESY Annual Report 2011.
	W.M. Gan, Y.D. Huang, N. Hort, M. Jiang, Z.Y. Zhong and H. -G. Brokmeier, Textures on a high plastic Mg-RE alloy by in-situ tensile deformation, DESY Annual Report 2011.
2012	Z.Y. Zhong, H. -G. Brokmeier, M. Jiang, B. Schwebke and N. Schell, Lattice strain investigation of Al7020 by in situ tensile loading, DESY Annual Report 2012.
	Z.Y. Zhong, H. -G. Brokmeier, B. Schwebke and N. Schell, Evolution of dislocations of a textured Al7020 during in situ tensile loading, DESY Annual Report 2012.
	Z.Y. Zhong, H. -G. Brokmeier, B. Schwebke and N. Schell, Diffraction elastic constants of textured Al7020 by in situ tensile loading, DESY Annual Report 2012.
	H. -G. Brokmeier, T. Lychagina, D. Nikolayev, B. Schwebke and Z.Y. Zhong, Investigation of texture inhomogeneity in magnesium alloy MA2-1 after equal channel angular pressing (ECAP), Part II, DESY Annual Report 2012.
	S. Yang, H. -G. Brokmeier, Z.Y. Zhong, M. Jiang and N. Schell, Characterization of phase transformation of Ti-6246 through thermal treatments using high energy synchrotron X-Ray radiation, DESY Annual Report 2012.
	N. Al-hamdany, H.-G. Brokmeier, B. Schwebke, Z.Y. Zhong and N. Schell, Texture Inhomogeneity through the Thickness of a Copper Tube, DESY Annual Report 2012.
	M. Z. Salih, N. Al-hamdany, Z. Y. Zhong, H.-G. Brokmeier, B. Schwebke and N. Schell, The effect of rolling degree on Fe-2.6%Si, DESY Annual Report 2012.
	M. Z. Salih, N. Al-hamdany, Z. Y. Zhong, H.-G. Brokmeier, B. Schwebke and N. Schell, The effect of rolling degree on Fe-2.6%Si, DESY Annual Report 2012.
2013	H. -G. Brokmeier, E. Maawad, Z.Y. Zhong, M.Z. Salih, N. Al-hamdany, B. Schwebke and N. Schell, Determination of polycrystal diffraction elastic constants of Ti-2.5Cu by using in situ tensile loading and synchrotron radiation, DESY Annual Report 2013.
	H. -G. Brokmeier, Z. Y. Zhong, M. Z. Salih, M. Jang, B. Schwebke, N. Schell, T. Lippmann, E. Maawad, W. M. Gan, Texture Analysis at HEMS and Harwi II.
	Z.Y. Zhong, H. -G. Brokmeier, N. Al-hamdany, M.Z. Salih and N. Schell, Through-thickness texture gradient of a rolled Al7020 plate, DESY Annual Report 2013.
	M. Blankenburg, P. Staron, A. Stark, T. Fischer, L. Bergmann, J. Hilgert, Z.Y. Zhong, N. Schell, J. dos Santos, A. Schreyer and M. Müller, In situ Study of Friction Stir Welding Thermal Cycles in Duplex Steel, DESY Annual Report 2013.
	W.M. Gan, Y.D. Huang, R. Wang, Z.Y. Zhong, N. Hort, K.U. Kainer, N. Schell, H.-G. Brokmeier, A. Schreyer, Bulk and local textures of pure magnesium processed by rotary swaging, Journal of Magnesium and Alloys, vol. 1, (2013), pp. 341-345.
2014	H.-G. Brokmeier, Z.Y. Zhong, N. Al-hamdany and W.M. Gan, Texture evolution along 45° direction of a textured AA 7020-T6 plate during cyclic loading, MLZ Annual Report 2014.

H.-G. Brokmeier, N. Al-hamdany, Z.Y. Zhong, and W.M. Gan, Texture before and after tensile load of swaged brass, MLZ Annual Report 2014.

E. Maawad, H.-G. Brokmeier, Z. Y. Zhong, N. Al-hamdany, M. Z. Salih, L. Wagner and N. Schell, Determination of polycrystalline diffraction elastic constants of Ti-2.5Cu by using in-situ tensile loading and synchrotron radiation, Material Science and Engineering A, vol. 594, (2014), pp. 62-67.

H. Alkhazraji, M.Z. Salih, Z.Y. Zhong, M. Mhaede, H.-G. Brokmeier, L. Wagner and N. Schell, Estimation of Dislocation Density in Cold-Rolled Commercially Pure Titanium by Using Synchrotron Diffraction, Metallurgical and Materials Transactions B, vol. 45B, (2014), pp. 1557-1564.

2015 H.-G. Brokmeier, E.S. Maawad, R. Bolmaro, Z.Y. Zhong and N. Schell, Combined materials characterization by area detector investigations using hard X-rays, IOP Conf. Ser.: Mater. Sci. Eng. 82 (2015) 012104.

Z.Y. Zhong, H.-G. Brokmeier, E.S. Maawad and N. Schell, Texture dependent lattice strains and texture gradient in Al7020, IOP Conf. Ser.: Mater. Sci. Eng. 82 (2015) 012100.

Z.Y. Zhong, H.-G. Brokmeier, E.S. Maawad and N. Schell, *In- situ* investigation of the anisotropic mechanical behavior of rolled AA 7020-T6 alloy through lattice strain evolution during uniaxial tension, Material Science and Engineering A, vol. 639, (2015), pp. 519-525.

Z.Y. Zhong, H.-G. Brokmeier, W.M. Gan, E.S. Maawad, B. Schwebke and N. Schell, Dislocation density evolution of Al7020-T6 investigated by in-situ synchrotron diffraction under tensile load, Materials Characterization, vol. 108, (2015), pp. 124-131.

M.Z. Salih, M. Uhlarz, F. Pyczak, H.-G. Brokmeier, B. Weidendeller, N. Al-hamdany, W.M. Gan, Z.Y. Zhong and N. Schell, The effect of magnetic annealing on crystallographic texture and magnetic properties of Fe-2.6% Si, Journal of Magnetism and Magnetic Materials, vol. 381, (2015), pp. 350-359.